

Electromagnetic Follow-up of Gravitational Wave Candidates

Darren J. White

Department of Physics & Astronomy
The University of Sheffield



The
University
Of
Sheffield.

*A dissertation submitted in candidature for the degree of
Doctor of Philosophy at the University of Sheffield*

5th March, 2014

Declaration

I declare that no part of this thesis has been accepted, or is currently being submitted, for any degree or diploma or certificate or any other qualification in this University or elsewhere.

This thesis is the result of my own work unless otherwise stated.

The following chapters have been based on publications:

- Chapter 2 – Abadie et al. (2012e) and Aasi et al. (2014).
- Chapter 3 – White, Daw & Dhillon (2011).
- Chapter 4 – Aasi et al. (2014), White, LIGO Scientific Collaboration & Virgo Collaboration (2012) and Nuttall et al. (2012).
- Chapter 5 – Work presented at the “Gravitational Wave - Electromagnetic Follow-up with UK Facilities” meeting at Warwick University.

Acknowledgements

The only way to start these acknowledgements is to thank my supervisors: Vik Dhillon for his wisdom and guidance in the scary world of research in Astrophysics, and Ed Daw for his encouragement, guidance and the odd kick up the backside when it was needed. We got there in the end, guys! Wouldn't have been possible without the both of you. I would also like to thank my collaborators within the LoocUp project, in particular Jonah Kanner, Peter Shawhan, Stephen Fairhurst, Laura Nuttall and Patrick Sutton for the many in depth discussions and support during this time.

A huge thank you to my family; Mum, Dad and Josh. The support you have given me in whatever I choose to do has been overwhelming. I wouldn't have made it this far without you. This thesis is dedicated especially to you.

I also have to thank my fellow members of the Sheffield Physics and Astronomy department, past and present, of which there are too many to name. Cheers for the camaraderie, fun times, Nerf battles and interesting chats. It is a wonderful department to work in, and I will miss it dearly when I leave. Special thanks go to Chris, Marvin, Parker, Allison, Grandpa, Furness and Bibby for helping out the newbies when I started! Also, to the genius of Paul 'Pablo' Kerry, for putting up with our daft questions and fixing our numerous self-inflicted computer problems.

Finally, I would like to say thank you to all of my friends and housemates who have kept me sane, cheered me up, and listened to my frustrations when things got tough. In no particular order; Claire, Nicki, Ellie, Cass, Georgia, Dom, Rich, Hodge, Amanda, Hannah, the Ra-Ra's, Luke, Tracy, Jen and countless others. Thank you all for your support. I couldn't have done it without you.

Summary

In the near future, gravitational wave (GW) detections are expected to become common, opening a new window on the Universe. Using the two 4 km Laser Interferometer Gravitational wave Observatory (LIGO) detectors and the 3 km Virgo detector we can triangulate a passing GW to a region of the sky with an area of tens of square degrees. These regions can then be observed using electromagnetic (EM) observatories. Pairing GW and EM observations can verify the astrophysical origin of a GW detection, and provide a more complete picture of the processes taking place.

This thesis describes the first triggered search for EM counterparts to GW candidates from the 2009-2010 LIGO/Virgo observing run. To improve the search strategy of this observing run, we created a catalogue of galaxies within 100 Mpc, known as the Gravitational Wave Galaxy Catalogue (GWGC), which was used to select locations in the GW skymaps to be imaged by EM partner observatories. Analysis of optical images taken as part of this run, from the Liverpool Telescope (LT) and ROTSE observatory network, find no associated counterparts. We also simulate the optical transients expected from GW sources across the LIGO/Virgo horizon of 50 Mpc, and find that the LT would be able to detect most optical counterparts across the majority of the horizon distance, while ROTSE can only detect counterparts over a fraction of the same distance.

Finally, we present the design specifications of GOTO, a wide field-of-view observatory to image the skymaps expected to be produced by the next generation of GW detectors. This telescope will be able to cover ~ 70 square degrees to a limiting magnitude of ~ 21 , the sky area and limiting magnitude required to offer a reasonable chance of detecting an EM counterpart. While NS-NS merger models are uncertain, a tentative first detection of a kilonova-like counterpart to GRB130603B leaves us optimistic that the advanced detector era will provide the first GW detections and EM counterparts.

Contents

1	Introduction	1
1.1	Introduction to Gravitational Waves	3
1.2	Gravitational Wave Detectors	7
1.2.1	Noise Sources	11
1.2.2	Current and Future Detectors	13
1.3	Gravitational Wave Sources	14
1.3.1	Burst	16
1.3.2	Compact Binary Coalescence	16
1.3.3	Continuous	17
1.3.4	Stochastic	18
1.3.5	Evidence for Gravitational Waves	18
2	Multi-Messenger Gravitational Wave Astrophysics	20
2.1	Motivation	21
2.1.1	Sources of GW+EM Emission	21
2.1.2	EM Triggered GW Searches	28
2.2	EM Follow-up Program	29
2.2.1	Optical Instruments	30
2.2.2	Radio and X-ray Instruments	32
2.2.3	Follow-up Pipeline	33
2.2.4	EM Follow-up Events	39
2.2.5	Blind Injection Challenge	41
3	GWGC: The Gravitational Wave Galaxy Catalogue	45
3.1	Motivation for the GWGC	45
3.2	Catalogue Compilation	47
3.2.1	Spatial Distribution of Galaxies	50

3.2.2	Distances	51
3.2.3	Blue Luminosities	55
3.2.4	Angular Diameters and Position Angle	57
3.3	Completeness	58
3.3.1	Comparison to other results	59
3.4	Galaxy Catalogues for the Advanced Detector Era	62
3.4.1	GWGC <i>I</i> -band Magnitude Update	62
3.4.2	H α and HI Surveys to Improve Catalogue Completeness	66
3.5	Conclusions	70
4	Optical Image Analysis of GW Triggers	72
4.1	Image Analysis Methods for the LoocUp Project	72
4.2	Liverpool Telescope Analysis	73
4.2.1	Follow-up Images Taken with the Liverpool Telescope	73
4.2.2	The Liverpool Telescope Analysis Pipeline	76
4.2.3	Efficiency of the Liverpool Telescope Pipeline	81
4.2.4	Analysis Results	89
4.3	ROTSE Analysis	89
4.3.1	Follow-up Images Taken with the ROTSE Network	89
4.3.2	The ROTSE Image Analysis Pipeline	90
4.3.3	Efficiency of the ROTSE Pipeline	95
4.3.4	Analysis Results	99
4.4	Conclusion	101
5	Follow-up observations in the advanced detector era using GOTO	103
5.1	The Advanced Detector Era	104
5.1.1	Commissioning and Observing Schedule	105
5.1.2	aLIGO/AdV Detection Capabilities	107
5.2	Optical Follow-Up with aLIGO/AdV	108
5.2.1	Optical Counterparts	108
5.2.2	Impact of Advanced Detector Capabilities on EM Follow-Up	109
5.2.3	GOTO - The Gravitational-Wave Optical Transient Observatory	117
5.2.4	Updated Opacities for r-process Material - Impacts for aLIGO/AdV	124
5.2.5	GRB 130603B - A Possible Kilonova Afterglow?	132
5.3	Conclusion	133

6	Conclusions and Future Work	136
6.1	Electromagnetic Follow-up	136
6.2	The Gravitational Wave Galaxy Catalogue	138
6.2.1	Optical Image Analysis from GW triggers	139
6.2.2	Efficiency Studies of Analysis Pipelines	140
6.2.3	Follow-up in the Advanced Detector Era	141
6.3	Future Work	141
A	Images from Observations and Analysis for the LIGO/Virgo Joint Science Run	145

List of Figures

1.1	Deformation of a ring of points during one cycle of a passing gravitational wave.	5
1.2	Schematic showing the basic layout of a LIGO-like interferometer.	7
1.3	Amplitude spectral density plot showing noise contributions for initial LIGO.	12
1.4	Comparison of frequency regions covered by ground and future space based detectors.	15
1.5	Examples of a GW signal from burst and inspiral sources.	17
1.6	Orbital decay in the binary pulsar B1913+16 caused by GW emission	19
2.1	Schematic of a typical collapsar process across a range of radii.	24
2.2	Observed X-ray, optical, high frequency and low frequency radio luminosity light curves over a range of observer angles.	26
2.3	A map showing the approximate positions of telescopes used during the 2009-2010 science run.	33
2.4	A flowchart of the real-time trigger analysis.	35
2.5	Sky maps of triggers sent for observations during winter run.	43
2.6	Skymaps of triggers sent for observations during autumn run.	44
3.1	Scatter plot showing distribution of galaxies in GWGC on the sky.	48
3.2	Comparison of distance measurements above 10 Mpc for the same galaxies using different methods.	52
3.3	Cumulative histogram of the major diameter of the galaxies in the GWGC.	58
3.4	Luminosity functions for both the GWGC and the CBCG catalogue at various distances.	60
3.5	Cumulative luminosity for the GWGC and the CBCG catalogue against distance	60

3.6	Plot of the fraction of the number of galaxies needed to obtain a target fraction of the total luminosity or mass.	64
3.7	Plot of the number of galaxies within 100 square degrees as a function of distance.	65
3.8	Estimated completeness of an all-sky HI survey with respect to total stellar mass and total star formation as a function of survey depth.	67
3.9	Estimated completeness of an all-sky, narrow-band H α survey with respect to total stellar mass and total star formation as a function of survey depth	68
3.10	Completeness of H α and HI surveys with respect to galaxies with properties similar to those of the host galaxies of short GRBs.	69
4.1	Skymap for the trigger G23004.	75
4.2	Typical images provided by the RATCam instrument and the SkyCamZ telescope	75
4.3	Plot showing the variation in the calibrated zero point offset for combined SkyCamZ images.	77
4.4	Simplified examples of bad subtraction using simple 1-D Gaussians. . . .	79
4.5	An example of candidate lightcurve and images produced by the pipeline for the Liverpool Telescope	82
4.6	Examples of the light curves used as models for transient injections. . . .	83
4.7	Comparisons of fits and injections of Moffat and Gaussian functions. . . .	85
4.8	Plots showing the efficiency of the LT pipeline as a function of distance for the RATCam images.	87
4.9	Plots showing the efficiency of the LT pipeline as a function of distance for the SkyCamZ images.	88
4.10	Example images for each GW trigger imaged and analysed from the ROTSE telescope network.	91
4.11	Distribution of the ranking statistic for background candidates.	95
4.12	Examples of injected transients with and without scaling in a single image. 98	
4.13	Plots showing the efficiency of the ROTSE pipeline as a function of distance.100	
5.1	Network sensitivity and localisation accuracy for face-on NS-NS systems with advanced detectors.	105
5.2	NS-NS merger afterglow lightcurves for distances of 40 and 70 Mpc. . . .	110
5.3	NS-NS merger afterglow lightcurves for distances of 100 and 130 Mpc. . .	111
5.4	NS-NS merger afterglow lightcurves for distances of 160 and 200 Mpc. . .	112

5.5	Typical GW trigger sky map, taken from blind injection study	116
5.6	Synthetic broadband light curves comparing Fe opacities to r-process opacities.	125
5.7	A comparison of broadband light curves of the fiducial model, calculated using line data from two different models of Nd.	126
5.8	Multi-colour light curves of model NSM-all.	128
5.9	Predicted <i>ugrizJHK</i> -band light curves for model NSM-all and 4 realistic models.	129
5.10	Broadband light curves from the total ejected material and the dynamically ejected matter alone.	131
5.11	X-ray, optical and NIR light curves of afterglows of GRB 130603B.	134
A.1	Examples of warped and subtracted Liverpool Telescope RATCam images.	146
A.2	Examples of warped and subtracted Liverpool Telescope SkyCamZ images.	147
A.3	Examples of images removed from the Liverpool Telescope analysis.	148
A.4	Examples of images removed from the ROTSE analysis.	149
A.5	Examples of artefacts from the Liverpool Telescope and ROTSE image analysis pipelines.	150

List of Tables

2.1	The EM partner observatories used during the 2009-2010 science run.	34
2.2	Triggers observed during the 2009-2010 science run.	40
3.1	A description of the columns in the GWGC.	50
3.2	A table of the contributions of unique galaxies from the selection of source catalogues.	51
4.1	List of GW triggers imaged by the ROTSE telescopes.	90
5.1	Summary of a plausible observing schedule, expected sensitivities, estimated source rates and source localisation for aLIGO/AdV	106
5.2	Table listing the visibility of on- and off-axis SGRB optical afterglows for $E_j = 10^{50}$ ergs and $n = 1 \text{ cm}^{-3}$	114
5.3	Table listing the visibility of on- and off-axis SGRB optical afterglows for $E_j = 10^{50}$ ergs and $n = 10^{-3} \text{ cm}^{-3}$	114
5.4	Table listing the visibility of on- and off-axis SGRB optical afterglows for $E_j = 10^{48}$ ergs and $n = 1 \text{ cm}^{-3}$	114
5.5	Table listing the visibility of on- and off-axis SGRB optical afterglows for $E_j = 10^{48}$ ergs and $n = 10^{-3} \text{ cm}^{-3}$	114
5.6	Table listing the visibility of kilonova light curves	114
5.7	An example of the range of light curves from the models discussed in this chapter.	130

Abbreviations

GW	Gravitational Wave
GR	General Relativity
EM	Electromagnetic
NS	Neutron Star
BH	Black Hole
LIGO	Laser Interferometer Gravitational wave Observatory
aLIGO	Advanced LIGO
AdV	Advanced Virgo
ITM/ETM	Input/End Test Mass
BS	Beamsplitter
AS Port	Antisymmetric Port
LoocUp	Locating and Observing Optical Counterparts to Unmodelled Pulses
CBC	Compact Binary Coalescence
cWB	Coherent WaveBurst
MBTA	Multi-Band Template Analysis
GraCEDb	Gravitational-wave Candidate Event Database
FAR/FAP	False Alarm Rate/Probability
SNR	Signal-to-Noise Ratio
GRB	Gamma Ray Burst
ROTSE	Robotic Optical Transient Search Experiment
LT	Liverpool Telescope
PTF	Palomar Transient Factory
TAROT	Télescopes à Action Rapide pour les Objets Transitoires
LOFAR	LOW Frequency ARray
XRT	X-Ray Telescope (Swift)
UVOT	UV/Optical Telescope (Swift)
HST	Hubble Space Telescope
FoV	Field-of-View
GWGC	Gravitational Wave Galaxy Catalogue
PGC	Principal Galaxy Catalogue
SDSS	Sloan Digital Sky Survey
WCS	World Coordinate System
FWHM	Full-Width at Half-Maximum
GOTO	Gravitational-wave Optical Transient Observatory

Chapter 1

Introduction

Over the past decade Gravitational Wave (GW) detectors have started to reach the sensitivity required for the detection of GW signals from astrophysical sources. With the installation of the Advanced LIGO (aLIGO) and Advanced Virgo (AdV) detectors, which are expected to begin observations over the next few years, it is hoped that detections become common, opening up a new window on the Universe. As well as confirming a key prediction of Einstein's theory of General Relativity (GR), the detection of GWs can provide information on the physics behind some of the most energetic astrophysical processes, the distributions of compact objects such as Neutron Stars (NSs) and Black Holes (BHs), galaxy evolution, measurement of the Hubble constant and even the early history of the Universe soon after the Big Bang.

While the information gathered from GW observations alone can help revolutionise our understanding of the Universe, joint observations with electromagnetic (EM) and particle (for example, neutrino) detectors could greatly increase the information available to us. To this end, a follow-up campaign was established during the most recent "Joint Science Run" during 2009-2010, in which the two LIGO detectors in the USA and the Virgo detector in Italy were operated together. During this campaign observing requests were sent to EM observatories in real-time, in an attempt to detect early EM counterparts

to potential GW detections.

This work summarises my efforts in trying to achieve the first joint GW+EM detection. My contribution to this effort covers a wide range of areas. Prior to the 2009-2010 joint science run, the 2 km Hanford detector was operated during the down-time of the 4 km LIGO detectors prior to the 2009-2010 science run. I spent the first 6 months of 2009 at Hanford as part of this project, known as Astrowatch, to help maintain the 2 km detector in observing mode in the rare possibility of a nearby Supernova or NS-NS merger. As a member of the “on-call” team during the 2009-2010 science run, it was my duty to perform manual validation of any triggered alerts, as described in chapter 2. I also developed Python scripts to handle both the ranking of galaxies in a typical error region, as well as sending observing requests to the Liverpool Telescope and LOFAR. My work also covered the analysis of images produced during the 2009-2010 science run. I created a series of Python scripts which used common image handling packages to analyse images taken with the LT, played a significant role in designing the ROTSE analysis, as well as creating code which injected simulated transients into the LT and ROTSE images, from which we can assess the efficiency of the pipelines used. Finally, I created a series of design requirements for the GOTO telescope, as described in chapter 5.

This thesis is organised as follows:

- Chapter 1 provides a brief introduction to gravitational waves, GW detectors and expected sources, along with some astrophysical evidence for the existence of GWs.
- Chapter 2 details the joint GW-EM campaign undertaken during the 2009-2010 science run, titled Locating and Observing Optical Counterparts to Unmodelled Pulses (LoocUp). This chapter briefly describes expected EM counterparts to GW sources, the GW trigger pipelines used to select possible GW candidates and alert partner observatories, as well as an overview of the observatories used and images

obtained.

- Chapter 3 details the compilation of a catalogue of nearby galaxies for use with the GW trigger pipelines described in Chapter 2, entitled the Gravitational Wave Galaxy Catalogue (GWGC). This chapter also briefly summarises the prospects of creating and using extended catalogues during the advanced detector era.
- Chapter 4 details the analysis of images taken with the Liverpool Telescope and the ROTSE Telescope Network during the 2009-2010 science run. Emphasis is placed on the development and testing of the analysis pipelines used for images taken with these observatories.
- Chapter 5 discusses the capabilities of aLIGO/AdV, and the implications for future optical follow-up campaigns. The design of a future wide-field optical observatory created specifically for GW follow-up in the advanced detector era is described: the Gravitational-Wave Optical Transient Observatory (GOTO).
- Finally, a summary of this thesis, with a look towards the start of the advanced detector era, is presented in Chapter 6.

1.1 Introduction to Gravitational Waves

Gravitational waves are a direct prediction of Einstein's theory of General Relativity (Einstein, 1918), which describes the relationship between matter and space-time geometry. In depth descriptions of Einstein's field equations and the full derivations of GW theory are beyond this work, but we will follow Saulson (1994) and Kanner (2011) in part in order to describe the basic features of how GWs are created, propagate and can be detected.

The space-time interval, ds , is used to describe the observer-independent measurement of the separation between two events. In flat Minkowski space-time (which is free

from local curvature due to gravity), this interval is:

$$ds^2 = -c^2 dt^2 + dx^2 + dy^2 + dz^2, \quad (1.1)$$

in Cartesian co-ordinates, where c is the speed of light. More generally this can be written as:

$$ds^2 = \sum_{\mu\nu} g_{\mu\nu} dx^\mu dx^\nu, \quad (1.2)$$

where the indices μ, ν run through 0, 1, 2 and 3, corresponding to cdt , dx , dy and dz in Cartesian co-ordinates. Here, $g_{\mu\nu}$ is the space-time metric, which defines our local space-time by relating our co-ordinates to the local measure of ds . For perfectly flat Minkowski space-time the metric must have the form:

$$\eta_{\mu\nu} = \begin{bmatrix} -1 & 0 & 0 & 0 \\ 0 & 1 & 0 & 0 \\ 0 & 0 & 1 & 0 \\ 0 & 0 & 0 & 1 \end{bmatrix}. \quad (1.3)$$

For our purposes, we assume that our local space-time is *nearly* flat:

$$g_{\mu\nu} = \eta_{\mu\nu} + h_{\mu\nu}, \quad (1.4)$$

where $h_{\mu\nu}$ describes perturbations to our local space-time and $h_{\mu\nu} \ll 1$. These perturbations are the GWs we hope to detect. Taking the weak-field limit of Einstein's field equations in a vacuum, and using gauge freedom to choose a coordinate system where the spatial coordinates of freely falling bodies are fixed, known as the transverse-traceless gauge, it can be shown that:

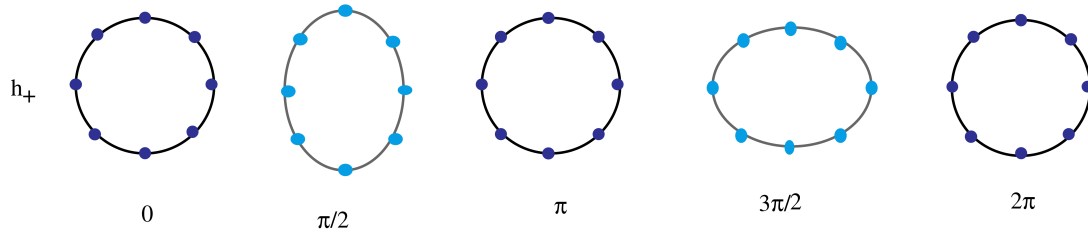


Figure 1.1: Deformation of a ring of points during one cycle of a passing gravitational wave, with polarisation h_+ , travelling normal to the page. Reproduced from Ju, Blair & Zhao (2000).

$$h_{\mu\nu} = \begin{bmatrix} 0 & 0 & 0 & 0 \\ 0 & h_+(t) & h_\times(t) & 0 \\ 0 & h_\times(t) & -h_+(t) & 0 \\ 0 & 0 & 0 & 0 \end{bmatrix}, \quad (1.5)$$

for a GW travelling along the z direction, where $h_{+/\times}$ define the polarizations of the GW. The effect of a passing GW can be seen in figure 1.1. For a ring of free-falling test masses, a passing GW contracts and expands the x and y distances between masses, with h_\times rotated by 45° compared to h_+ .

Analogous to EM radiation (which is emitted by accelerated charged particles), GWs are emitted by accelerated masses. However, unlike EM radiation, in which the dominant form of radiation from a moving charge is electric and magnetic dipole radiation, the simplest form of gravitational radiation is the quadrupolar moment, $I_{\mu\nu}$ (see Saulson, 1994; Kanner, 2011, for detailed discussion). It can be shown that the quadrupole from a spherically symmetric mass distribution is zero, therefore GW perturbations can only be produced from an asymmetric accelerated mass system. A standard example is that of two spherical masses in orbit around a common centre of mass, each with mass M and separated by a radius r . For these systems the scale of the GW perturbation can be calculated using:

$$h_{\mu\nu} \sim \frac{G}{c^4} \frac{Mr^2}{DP^2}, \quad (1.6)$$

where G is the gravitational constant, D is the distance to the GW emitting source and P is the rotational period (Saulson, 1994; Kanner, 2011). It is interesting to note that the strength of the emission varies as $1/D$, rather than $1/D^2$ as with EM emission. This implies that doubling the distance of the detector from a source results in a halving of the detectable signal in contrast to EM detectors, such as telescopes, where doubling the distance would decrease the detected flux by a factor of 4. A typical system we expect to detect via GW emission is that of a binary neutron star (NS-NS) system. For such a system located in the Virgo cluster at a distance of ~ 15 Mpc, with a separation of 20 km, two NSs with masses of $1.4 M_{\odot}$ are estimated to provide perturbations of:

$$h_{\mu\nu} \sim 10^{-21}. \quad (1.7)$$

To put this in context, as we will see from equation 1.17, a 4 km long GW detector will change in length by $1/1000^{\text{th}}$ of the radius of a proton. As a comparison, we can construct a similar system that could feasibly be built in a lab on Earth. Take a typical weightlifters bar of length ~ 2 m, with two weights of 100 kg on each end, spinning at 1000 revolutions per second. The scale of the GW perturbation at a distance of 500 km is:

$$h_{\mu\nu} \sim 10^{-42}, \quad (1.8)$$

which is over 20 orders of magnitude weaker than the GW emission from a distant astrophysical source! It is therefore obvious that the detection of GWs is likely to be difficult due to both the weak emission for even a standard extragalactic source, and the uncontrollable nature of astrophysical sources.

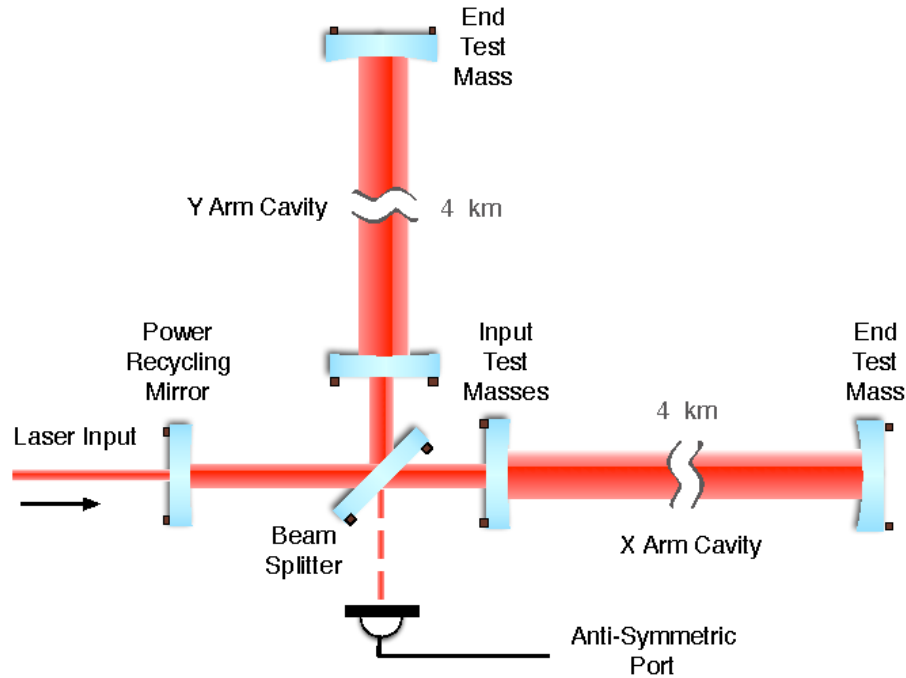


Figure 1.2: Schematic showing the basic layout of a LIGO-like interferometer. Reproduced from Abadie et al. (2010).

1.2 Gravitational Wave Detectors

So far we have only focused on the nature of GWs, but now we turn to past, present and future efforts to detect them. Gravitational wave detectors have been in operation, in various forms, since the 1960's. The first detectors were resonant-mass bar detectors, a design created by Joseph Weber at the University of Maryland (Weber, 1967). The original "Weber bar" consisted of a solid Aluminium cylinder with piezo-electric detectors attached to detect the energy deposited by a passing GW. Unfortunately these were only sensitive to strains of 10^{-16} , too weak to detect anything other than the very nearest, extremely rare sources such as supernovae and NS-NS mergers. Such systems were also only sensitive to specific frequencies of GWs.

In the 1990's, construction began on large scale, laser-interferometry based detectors in the United States. The Laser Interferometer Gravitational wave Observatory (LIGO; Abbott et al., 2009a) network consisted of two identical Michelson interferometers, with arms 4 km in length at a 90° angle. Looking at figure 1.2, frequency-stabilised infrared light ($\lambda = 1064$ nm) enters the detector and is sent down each arm (labelled the X and Y arms) by a beamsplitter. A 10 kg test mass lies at the end of each arm, labelled the End Test Mass (ETM). Each ETM has a highly reflective coating, allowing the ETM to also act as the mirror needed for a Michelson interferometer. Light is reflected, recombines at the beamsplitter and, depending on the phase of the two beams, is detected by photodetectors at the Anti-Symmetric (AS) Port. A power recycling mirror, as the name suggests, reflects light that would normally be sent back towards the laser source by the beamsplitter, and increases the overall power available in the interferometer by a factor of 50 alone. The inclusion of another pair of 10 kg mirrors, the Input Test Masses (ITMs), forms a resonant cavity in each arm, known as a Fabry-Perot cavity, which acts to increase the stored power and also keep photons in the arms for up to 1 ms. This helps increase sensitivity to GWs at lower frequencies. The test masses are suspended by wires, and can be considered “freely falling” in the direction along the length of the arms of the interferometer. Under these conditions we can show the basic effect of a passing GW on the interferometer. Consider a basic Michelson configuration (no ITMs) and a GW approaching from the zenith, with the X and Y arms aligned with the x and y axes of the Cartesian co-ordinate system. Combining equations 1.2 and 1.4 with the space-time metrics from equations 1.3 and 1.5, we find:

$$ds^2 = -c^2 dt^2 + (1 + h_+(t)) dx^2 + 2h_\times(t) dx dy + (1 - h_+(t)) dy^2 + dz^2. \quad (1.9)$$

For simplicity, we assume that the time span is much shorter than the period of the

GW, so $h_{+/\times}(t)$ is approximately constant. For light travelling along the arms, $ds^2 = 0$. Considering the X arm first ($dy = dz = 0$), we see that equation 1.9 reduces to:

$$c^2 dt^2 = (1 + h_+) dx^2, \quad (1.10)$$

which leads to:

$$\frac{dt}{dx} = \pm \frac{1}{c} \sqrt{1 + h_+} = \pm \frac{1}{c} \left(1 + \frac{1}{2} h_+ \right), \quad (1.11)$$

where the square root is approximated given that $h_+ \ll 1$. The sign on dt/dx depends on the direction of travel. The distance from the beamsplitter to the ETM is the arm length, L . Therefore, the outward bound time to reach the X arm ETM, τ_{xo} , is given by:

$$\int_0^{\tau_{xo}} dt = \int_0^L \frac{dt}{dx} dx = \int_0^L \frac{1}{c} \left(1 + \frac{1}{2} h_+ \right) dx \quad (1.12)$$

$$\tau_{xo} = \frac{L}{c} \left(1 + \frac{1}{2} h_+ \right). \quad (1.13)$$

For the return journey:

$$\tau_{xr} = \int_L^0 -\frac{1}{c} \left(1 + \frac{1}{2} h_+ \right) dx = \frac{L}{c} \left(1 + \frac{1}{2} h_+ \right). \quad (1.14)$$

This gives a total round-trip time of:

$$\tau_{xt} = \frac{L}{c} (2 + h_+). \quad (1.15)$$

For non-perturbed space-time the total travel time should be $2L/c$, so a passing GW increases the trip time by h_+L/c . Since the speed of light is a constant this difference can be thought of as a change in length of the arm due to perturbation:

$$\Delta L = \frac{c}{2} \left(\frac{h_+ L}{c} \right), \quad (1.16)$$

$$\frac{\Delta L}{L} = \frac{h_+}{2}. \quad (1.17)$$

From this it can be seen that the GW increases the distance between free-falling objects by a distance proportional to their initial separation, which is why GW perturbations are described as ‘strain’. For a 4 km arm, this results in a change in arm length of 10^{-18} m, $1/1000^{\text{th}}$ of the radius of a proton. Performing the same calculations for the Y arm we get a total round-trip time of:

$$\tau_{yt} = \frac{L}{c}(2 - h_+). \quad (1.18)$$

For an unperturbed interferometer, phase fronts which leave the beamsplitter at the same time on their outward journeys should recombine at the same time on their return. However, the passing GW alters the arrival time of the phase fronts by:

$$\Delta\tau = \tau_{xt} - \tau_{yt} = \frac{2Lh_+}{c}. \quad (1.19)$$

This difference in arrival times can be described as a difference in phase, given by:

$$\Delta\phi = \frac{2\pi\Delta\tau c}{\lambda} = \frac{4\pi Lh_+}{\lambda}, \quad (1.20)$$

which is detected by the photodiode at the AS readout port as a shift in the fringe pattern. This simplified description is sufficient to gain an understanding of the appearance of a signal in the limit where the gravitational wave period is much longer than the storage time of the light in the interferometer arms. Where this approximation breaks down, for high frequency gravitational waves, the strain sensitivity of LIGO is reduced. Control systems keeping the cavity arms aligned also affect the reality of GW detection.

For a more detailed discussion, see Saulson (1994). One important feature of real GW detection to consider is the sensitivity of the detector across the sky. The calculations above were for a source directly above the interferometer, but the sensitivity varies with the direction of the incoming GW with respect to the interferometer layout. This directional sensitivity is known as the antenna pattern of the interferometer, and the total strain detectable by an interferometer is a function the antenna pattern, the two polarisations and the direction of the incoming GW. The sensitivity varies broadly across the sky, with higher sensitivity orthogonal to the arms, decreasing to a minimum (but not necessarily zero) in the plane of the instrument. This broad variation in sensitivity is why a single interferometer can be considered an “all-sky” instrument, and provides little directional information for an incoming GW. This is ideal for simply detecting signals, but for the work described in later chapters this lack of directional sensitivity provides a difficult challenge in localising the origin of an incoming GW (Abbott et al., 2009a).

1.2.1 Noise Sources

There are a great variety of technical noise backgrounds to an interferometer signal. For a detailed review, refer to Freise & Strain (2010) and Sigg (1998). As discussed in section 1.1, the scale of a GW perturbation is expected to be at most $\sim 10^{-21}$. For a 4 km scale detector, using equation 1.17, we can estimate a fractional change in length of 10^{-18} . This length change is incredibly small - less than 1/1000th of the radius of a proton! To achieve sensitivity to such a small signal, the interferometer noise must be well below this anticipated signal amplitude in the sensitive band of the instrument, as shown in figure 1.3. At low frequencies seismic noise dominates. By suspending the test masses as a pendulum, and placing the pendulum on a vibration isolation stack, higher-frequency seismic noise is reduced. High frequency noise is dominated by Poissonian “shot noise” of the photons in the interferometer, which do not arrive in an ordered, continuous stream,

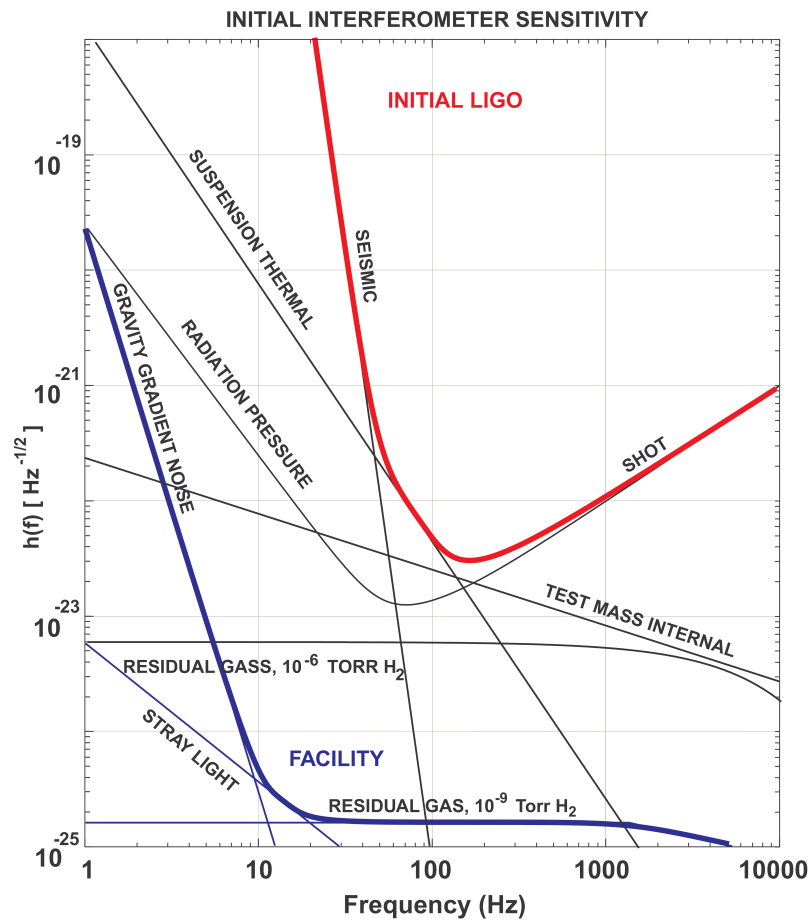


Figure 1.3: Amplitude spectral density plot showing a variety of noise contributions for initial LIGO, and theoretical sensitivity limits for ground based detectors due to these noise sources. See text for description of the main noise sources. Reproduced from Sigg (1998).

but in random bunches. For higher frequencies, the number of photons in a single period of a GW is smaller, resulting in higher Poissonian noise. Other significant noise sources include the vibrational modes of the suspension wires, and Brownian thermal noise in the test masses. Longer-period effects are also present. Thermo-elastic distortion of the mirrors due to light absorption, and environmental effects, such as the deformation of the Earth's crust due to the lunar cycle, must also be treated with care.

1.2.2 Current and Future Detectors

Several detectors similar to the LIGO interferometer design exist across the world. The two LIGO detectors are located in Hanford, Washington (H) and Livingston, Louisiana (L) in the United States. Prior to Summer 2009, a smaller, 2 km-scale detector was also installed at Hanford, designated H2, which was used to cross-correlate detection of stochastic background sources, and also for periods when the larger interferometers were in the process of upgrade and commissioning. The LIGO Scientific Collaboration operates the US-based detectors, along with a smaller 600 m scale interferometer in Hannover, Germany, named GEO600, which primarily acts as a test bed for advanced technology to be used on future detectors. This is also true of the Cryogenic Laser Interferometer Observatory (CLIO; Yamamoto et al., 2008), a 100 m prototype detector located in the Kamioka mine, Japan and TAMA300 (Kozai & TAMA-300 Team, 1999), a 300 m prototype detector at the Mitaka campus of the national astronomical observatory of Japan. The two km-scale detectors in the US ran in “joint science mode” with the 3 km Virgo detector (V) in Cascina, Italy, where GW data was shared for joint analysis, which we shall discuss in more detail in chapter 2.

As of 2010, all three km-scale detectors are undergoing significant upgrades, aimed at increasing the sensitivity by a factor of 10. Advanced LIGO in particular will take advantage of more advanced, active seismic isolation stacks, a new high power laser (125 W compared to 6 W for initial LIGO), and larger, more massive test masses (40 kg compared to 11 kg for initial LIGO). Similar upgrades are also planned for the Virgo interferometer. The initial plan for aLIGO also called for a third 4 km long detector to be installed at Hanford, replacing the smaller H2 detector. However, in order to improve on the sky coverage and localisation (discussed in chapters 2 and 5), the third interferometer is planned to be installed in India, with installation lagging behind by a few years. This reduces median sky localisations from around 70 square degrees for a 3-detector network

to around 10 square degrees with LIGO-India (LIGO Scientific Collaboration et al., 2013). An upgrade to CLIO is also being planned, using techniques also developed using TAMA300, which will result in a km-scale detector currently named Kamioka Gravitational Wave Detector (KAGRA; previously the Laser Cryogenic Gravitational-wave Telescope - LCGT), with early operation beginning from around 2018 (Kuroda & LCGT Collaboration, 2010).

Other proposed detectors include a space-based detector, the Laser Interferometer Space Antenna (LISA), which will utilise three test masses in an equilateral triangle formation separated by up to 5 million kilometres (see Danzmann, 2000; Antonucci et al., 2012; Amaro-Seoane et al., 2013, for a more detailed overview and current status). LISA will primarily search for gravitational waves at lower frequencies due to the absence of seismic noise and longer arm lengths, extending the range of detectable sources to include, for example, white dwarf coalescing binaries or wide-orbit black hole binaries within our galaxy. A comparison between Earth and space-based detectors is shown in figure 1.4. It may also be possible to detect GWs using a pulsar timing array, which attempts to observe subtle shifts in the periods of pulsars caused by passing GWs (Hobbs, 2011). However, for the work described here, our primary concern is that of ground-based km-scale interferometers.

1.3 Gravitational Wave Sources

Now we know how gravitational waves propagate and how we can detect them, we shall briefly discuss the types of sources we expect to detect. As alluded to in section 1.1, GWs we would like to observe must come from astrophysical sources. A broad overview of GW sources can be found in Cutler & Thorne (2002, and references therein). Here we provide a summary of the types of sources we may possibly be able to detect with

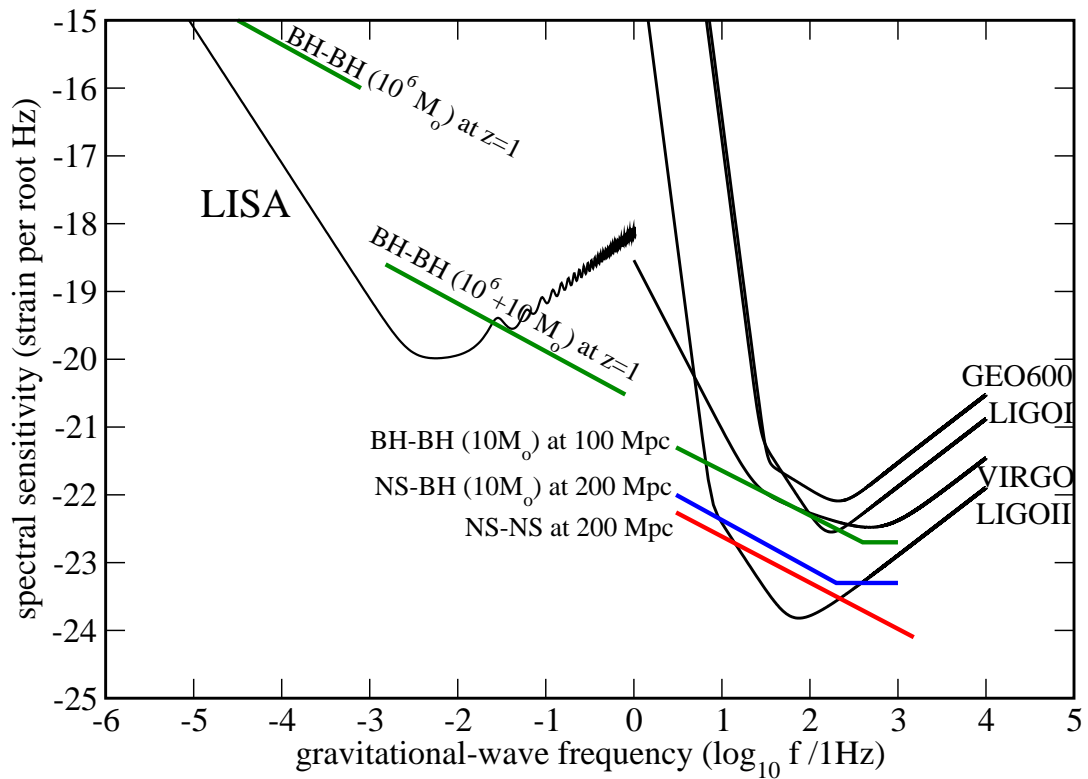


Figure 1.4: Comparison of frequency regions covered by current and future ground and space based detectors. The current "enhanced" LIGO frequency curve (not shown) is at the limit for Compact Binary Coalescence, between the initial and advanced LIGO curves. Reproduced from Kokkotas (2008).

LIGO and Virgo. GW sources can be split into 4 groups¹:

- Burst: Unmodelled, transient
- Compact Binary Coalescence (CBC): Modelled, transient
- Continuous: Modelled, non-transient
- Stochastic: Unmodelled, non-transient.

Burst and CBC sources are the main types of sources we are searching for in this work, as described in chapter 2, which includes more detail on potential sources and a brief overview of analysis methods.

1.3.1 Burst

Burst sources are defined as those which produce a short excess of power detected in the GW interferometer output. They are expected to be associated with catastrophic astrophysical events, such as core-collapse supernovae with an asymmetric explosion, or a neutron star “quake”. Burst searches are waveform independent, partly due to the lack of accurate modelling of these sources, but this also allows us to detect unexpected sources of GWs.

1.3.2 Compact Binary Coalescence

CBC (also known as Inspiral) sources are compact binary systems which are in the final stages of their orbit, which has decayed due to dynamic interactions and/or GW emission. During the final few minutes of the lifetime of such a system (those comprised of neutron stars or black holes for ground-based detectors), the GW emission increases as the orbit shrinks and the frequency increases. This produces a characteristic “chirp”

¹A brief overview of gravitational wave sources and example waveforms is available at <http://www.ligo.org/science.php>

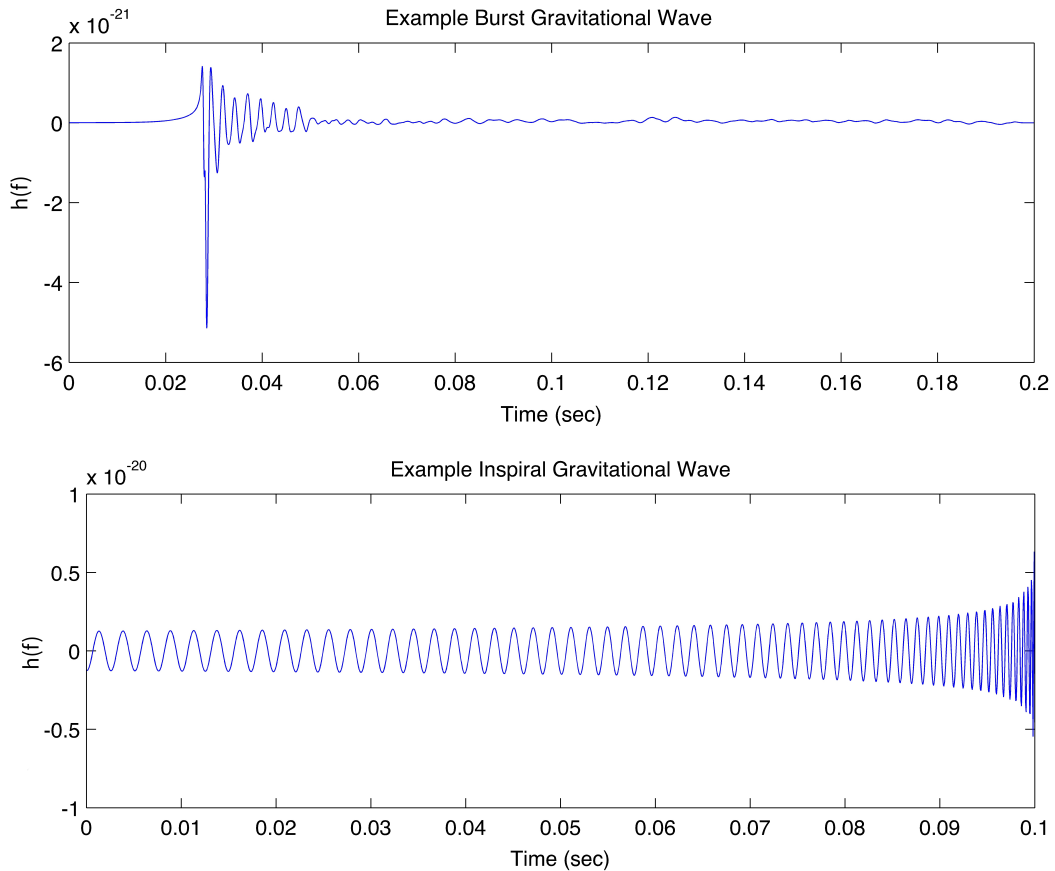


Figure 1.5: Examples of a GW signal expected from burst (top) and inspiral (bottom) sources. The burst source is one example of the GWs predicted for a non-spherical core-collapse supernova, reproduced from Ott et al. (2004). The inspiral source shows the typical ‘chirp’ signal, an increase in frequency and amplitude, expected from merging compact objects, such as two neutron stars. Reproduced from <http://www.ligo.org/science.php>.

signal, an example of which is shown in figure 1.5. Eventually the orbit is no longer stable and the binary system merges into a single black hole. This final stage of merger is also expected to produce a significant burst of GW energy.

1.3.3 Continuous

Continuous sources are generated by any periodic motion with a non-axisymmetric mass distribution, such as slowly orbiting compact binaries (prior to the CBC phase), or rapidly rotating neutron stars with surface irregularities, such as “mountains” formed

from distorted NS crusts. The former source, while strong, produces GWs of frequencies far too low for current ground-based detectors. For rapidly rotating NSs, the asymmetric mass is likely to be comparatively small, and the GW amplitude will therefore only be detectable for sources within the Milky Way (Ushomirsky, Cutler & Bildsten, 2000).

1.3.4 Stochastic

Stochastic GWs are analogous to the Cosmic Microwave Background, and are comprised of many unresolved features. Primarily, stochastic GWs are from an “astrophysical background”, which is the sum of unresolved GW emitting sources such as distant NS mergers and SNe, which are individually very weak. It is also possible that GWs from the inflationary period of the early universe could make up part of this stochastic background. For an overview of stochastic sources and detection see Ferrari, Matarrese & Schneider (1999a,b).

1.3.5 Evidence for Gravitational Waves

The most convincing evidence to date for the existence of GWs is found in the observations of binary pulsar systems (Hulse & Taylor, 1975; Lorimer, 2008). Pulsars are neutron stars which emit radio waves due to an intense magnetic field accelerating charged particles along the magnetic axis. If the magnetic axis does not align with the spin axis, these radio beams sweep across the sky, sometimes hundreds of times per second. If a pulsar is in orbit around another star, we can measure the orbital period of the system. If GWs are being emitted in the manner described in this chapter, then we should see the orbital period decrease. The most famous example of this is the binary pulsar system B1913+16, known as the Hulse-Taylor pulsar after the discoverers (Hulse & Taylor, 1975). This pulsar has been observed for over 30 years, and has been shown to decay in a manner expected by GW emission, as shown in figure 1.6. The observations are

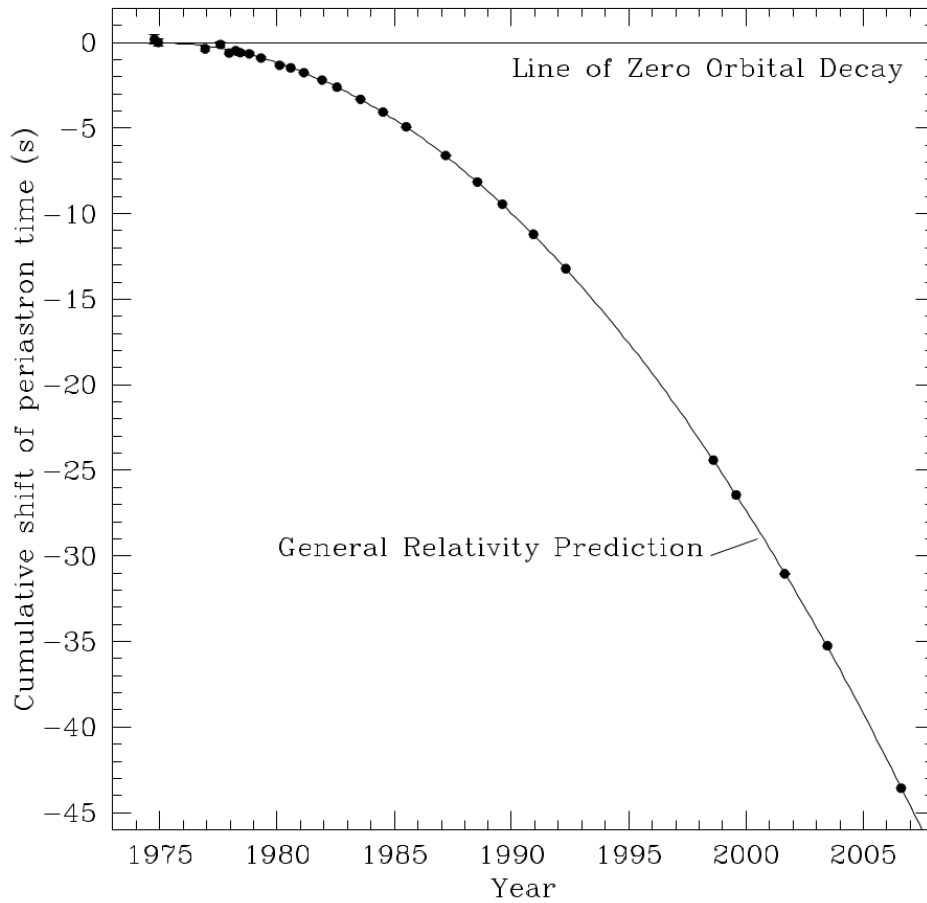


Figure 1.6: Orbital decay in the binary pulsar B1913+16 system demonstrated as an increasing orbital phase shift for periastron passages with time. The prediction due entirely to the emission of gravitational radiation is shown by the black solid line. Reproduced from Lorimer (2008).

so accurate that the error bars are smaller than the data points, which lie exactly on the curve predicted by general relativity to an accuracy of 0.13% (Weisberg & Taylor, 2005). Similar orbital decay has also been seen in several other systems (see Kramer et al., 2006; Jacoby et al., 2006, for examples), which suggests that the most simple and natural explanation is that of GW emission.

Chapter 2

Multi-Messenger

Gravitational Wave

Astrophysics

Work described in this chapter has been previously published, or is currently in preparation. The chapter broadly follows the work described in Abadie et al. (2012e), while section 2.2.4 is based on Aasi et al. (2014), which is the companion results paper to Abadie et al. (2012e). My contribution to this work was the planning of observations using the Liverpool Telescope, testing of the automated scripts to communicate triggered observations to the Liverpool Telescope and LOFAR, and as a member of the “on-call” team, which responded to trigger alerts and performed the necessary human quality check before submitting observing requests to telescopes.

During the 2009-2010 joint science run, the LIGO and Virgo detector data was analysed together in real-time for the first time. This allowed us to observe the most probable sky locations of GW candidates with EM observatories. This chapter discusses the sources we hope to detect using these partner observatories, placing emphasis on the counterparts expected for NS-NS mergers, as these are the systems considered most likely

for the first GW detection. We also briefly describe results from other joint GW+EM analyses, based on EM triggered GW data searches, during the previous two LIGO science runs designated S5 and S6. Finally, we discuss the GW trigger pipeline and observing strategy, the partner observatories used, and the triggers for which EM follow-up observations were taken.

2.1 Motivation

The detection of a GW signal alone will open up a new window on the universe. As mentioned in chapter 1, by observing GWs we can investigate the intrinsic physical properties, distribution and event rates for a variety of sources difficult to observe via EM emission. Paired together, joint GW+EM observations present one of the most promising opportunities to improve our understanding of the physical processes behind some of the most violent and energetic events known, such as Gamma Ray Bursts (GRBs) and Core-Collapse Supernovae (CCSNe), which we describe in this section. The distance to the source can be determined by matching an EM counterpart with a galaxy, or through spectroscopic measurements. Observations across a range of wavelengths can also allow us to obtain spectral energy distributions, providing a test for predicted models for a variety of sources. An EM counterpart to a GW event would also improve our confidence in the GW detection.

2.1.1 Sources of GW+EM Emission

Several sources of GWs are expected to provide detectable EM emission. For this work we primarily look at NS-NS merger systems, but we will also briefly describe other possible GW+EM sources.

Gamma Ray Bursts (GRBs)

Gamma Ray Bursts are, as the name suggests, extremely bright flashes of gamma radiation. Since the atmosphere is opaque to gamma rays, GRBs are only directly detectable with space-based detectors, such as the Burst Alert Telescope (BAT; Barthelmy et al., 2005) on the Swift satellite (Gehrels et al., 2004) and the Gamma-ray Burst Monitor (GBM; Meegan et al., 2009) and Large Area Telescope (LAT Atwood et al., 2009) detectors on the Fermi satellite.

GRBs are typically placed in one of two categories, based on the length of time that contains 90% of the prompt gamma ray emission - Short GRBs (SGRBs) with $t_{90} < 2$ s and Long GRBs (LGRBs) with $t_{90} > 2$ s. It is generally accepted that these two classes are broadly consistent with two progenitors. It is thought that most LGRBs are the result of CCSNe, due to the formation of a central black hole and subsequent rapid accretion of stellar material, known as the collapsar model (see e.g. Piran, 2004, for a broad overview). As a massive star collapses it forms a BH at its centre. As the surrounding stellar material falls inwards, the rapidly rotating material in the centre forms an accretion disc orthogonal to the spin axis of the rotating BH. The inner parts of the accretion disc are relativistic and highly magnetic. Outflows due to accretion of stellar material onto the spinning BH travel along the magnetic field lines, which run parallel to the rotational axis of the BH, forming a relativistic jet. This jet interacts with the surrounding stellar material, before eventually breaking out from the surface of the stellar remnant. The resultant emission is highly collimated along the rotation axis of the BH, which we detect as a GRB (see Woosley, 1993; MacFadyen & Woosley, 1999; MacFadyen, Woosley & Heger, 2001; Piran, 2004; Gehrels, Ramirez-Ruiz & Fox, 2009, and references therein for more detailed descriptions, and figure 2.1 for a general diagram). LGRBs have been observed with prompt optical and X-ray afterglows, along with longer duration supernova counterparts (see Kann et al., 2010, 2011; Nysewander, Fruchter & Pe'er,

2009; Gehrels, Ramirez-Ruiz & Fox, 2009, for examples and an overview of GRB observations). Unfortunately, GWs from such systems are difficult to estimate and detect as the mass distribution is dominated by the spherically symmetric central body, so there is no significant mass rotating asymmetrically (see Ott, 2009, and references therein for details), and for the 2009-2010 science runs are unlikely to be detected outside the Local Group of galaxies.

SGRBs are thought to be the result of the merger of a NS-NS or NS-BH system. Similar to the collapsar model, a merging system can produce powerful magnetic fields, either from one of the NSs or in the material ejected during the merger. Again, this material is accelerated along the rotation axis, producing a highly collimated jet. The lack of stellar material for the jet to interact with, along with the millisecond time scale for merger and accretion, results in very short, but highly energetic gamma ray emission, with jet energies, E_j , ranging from 10^{48} to 10^{51} ergs, compared with 10^{50} to 10^{54} ergs for LGRBs. (Gehrels, Ramirez-Ruiz & Fox, 2009). As with LGRBs, the interaction of the jet with the surrounding medium has been shown to produce prompt optical and X-ray afterglows (see Kann et al., 2011, and figure 4.6 for examples). The afterglows to SGRBs are generally fainter than LGRBs, primarily thought to be due to the lower density of the medium surrounding the progenitor. For LGRBs, both the stellar remnant and the comparatively high density of inter-stellar medium (ISM), due to the star being located in a cluster, results in a surrounding medium of higher density for the jet to interact with. For SGRBs, if NS-NS mergers are the progenitors, there is no guarantee that the merger and subsequent jet will occur in the same environment as is typical for LGRBs. Some binaries may merge soon after forming due to interactions with other stars in a dense cluster. Others may receive large kicks during their evolution, resulting in a merger outside of a galaxy in the inter-galactic medium (IGM). The density, n , of these environments is thought to vary from 10^{-6} cm^{-3} for mergers in the IGM, to 1 cm^{-3} for the ISM, and even higher for clusters. For a detailed overview of SGRB observations

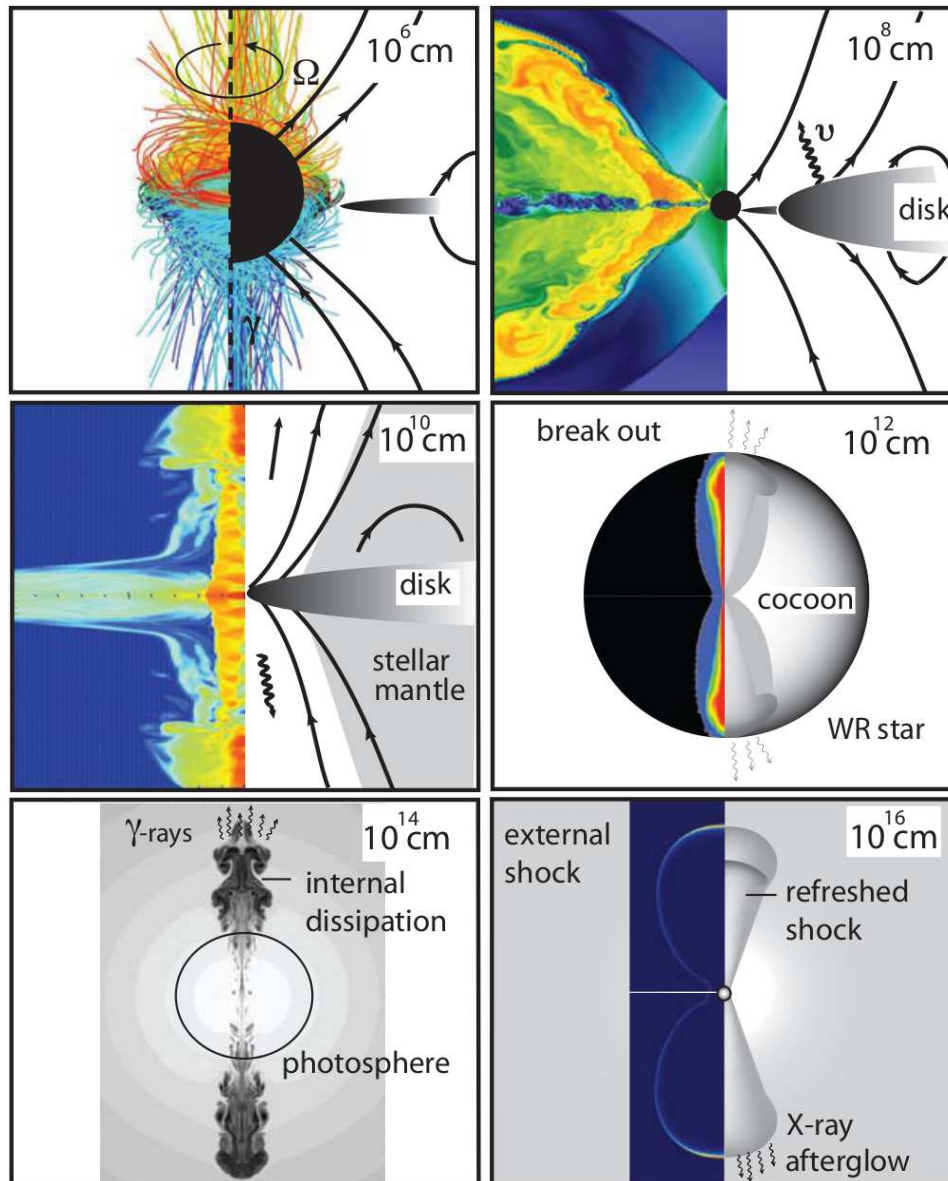


Figure 2.1: Schematic of a typical collapsar process across a range of radii of the central star. Top left: 10^6 cm - The central BH or NS and its magnetosphere. Top right: 10^8 cm - Inner accretion disk with strong magnetic field lines. Differential rotation of inner and outer disk is expected to produce large magnetic structures and coronal arches, accelerating material along the rotation axis of the central BH or NS. Middle left: 10^{10} cm - Even weak magnetic fields are expected to produce some beaming due to the stellar envelope. 10^{12} cm - Inner jet is collimated due to stellar remnant surrounding star, until jet reaches the surface. 10^{14} cm - Post-break-out, the jet dissipates due to velocity differences of material. 10^{16} cm - Post-GRB, lower velocity material dominates, resulting in X-ray and optical afterglows. Reproduced from Gehrels, Ramirez-Ruiz & Fox (2009).

and theory, see Nakar (2007), Gehrels, Ramirez-Ruiz & Fox (2009) and Nysewander, Fruchter & Pe'er (2009), and references therein.

It is also important to note that GRB EM afterglows are seen along the axis of the merger (within the opening angle of the jet), whereas it is possible for GW detectors to observe mergers across a wide range of angles between the merger axis and line-of-sight. The opening angle, θ_j of the jet is also important, and seemingly quite variable for SGRBs, ranging from 0.07 radians to 0.4 radians (Nysewander, Fruchter & Pe'er, 2009). Recently van Eerten & MacFadyen (2011) investigated the effect of viewing NS-NS mergers at various angles from the merger axis for X-ray, optical and radio afterglows. Examples of synthetic light curves, which depend on the jet energy, surrounding medium density and jet opening angle of the system, can be seen in figure 2.2. As shown, the further off axis the SGRB is observed, the fainter and more delayed the peak of the afterglow is expected to be. This delay could make it difficult to link a possible GW event to a faint counterpart several tens of days after the event. However, due to the sensitivity of LIGO and Virgo during the 2009-2010 science run, and the need to be confident in the detection of a prompt counterpart, we concentrated on light curves for on-axis mergers to guide our follow-up efforts and subsequent analysis, as discussed in chapter 4.

Kilonovae

During recent years, another possible EM emission mechanism for compact object mergers has gained popularity - the kilonova. It is expected that a NS-NS or NS-BH merger should produce a significant amount of neutron rich ejecta during the final inspiral phase. The ejecta undergoes r-process nucleosynthesis, producing heavy elements which decay and heat the material, powering a fainter optical counterpart to NS-NS mergers separate to any expected SGRB emission and subsequent afterglow. For the majority of this work, we use the models found in Metzger et al. (2010), who use a nuclear reaction

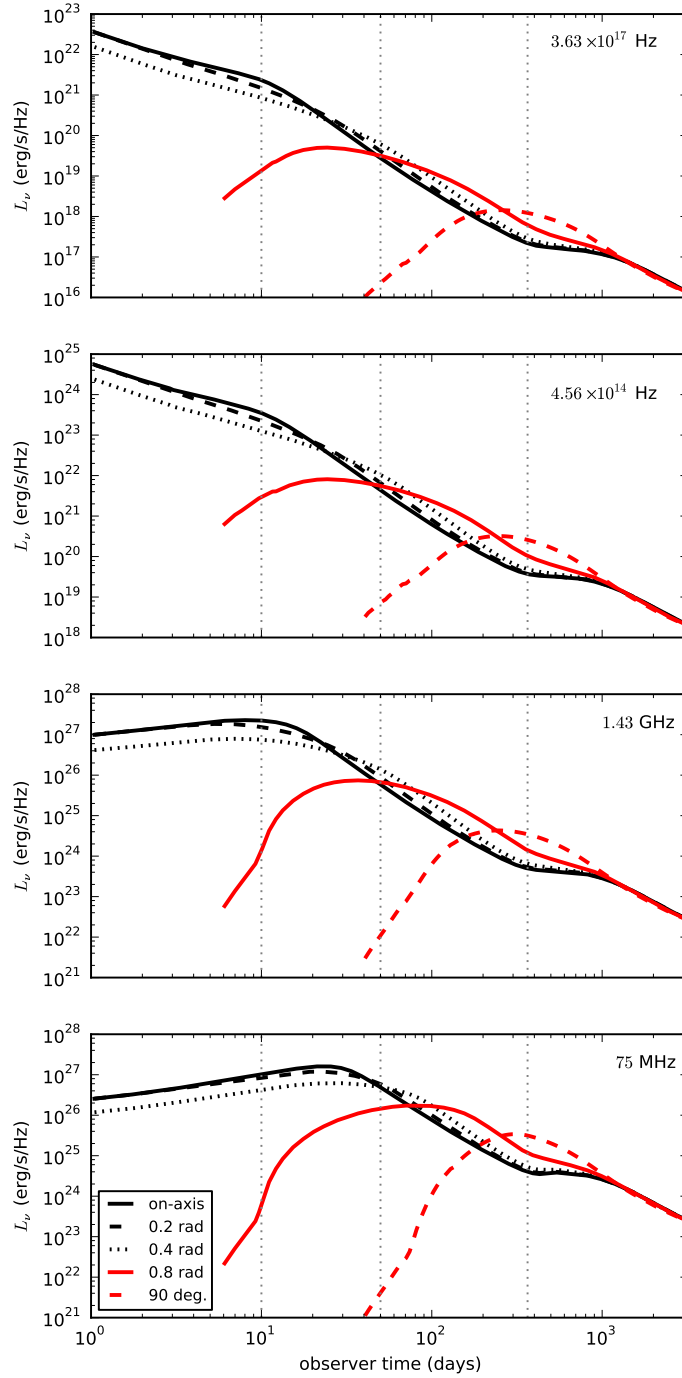


Figure 2.2: SGRB afterglow light curves for $E_j = 10^{48}$ ergs, $\theta_j = 0.4$ rad, $n = 10^{-3} \text{ cm}^{-3}$ over a variety of observer angles, from on-axis to 90 degrees off-axis. Observer frequencies, from top to bottom, correspond to X-ray, optical, high frequency and low frequency radio emission. 10 days, 50 days and 1 yr have been marked with vertical dotted grey lines. Reproduced from van Eerten & MacFadyen (2011).

network to calculate the decay and heating rates. Using the heating rate, Metzger et al. (2010) use radiation transport models to estimate the light curves for a range of ejecta masses. Importantly, in the radiative transport calculations Metzger et al. (2010) uses Iron opacity data to estimate the opacity of the ejecta. More recent work, as described in section 5.2.4, suggests this may underestimate the amount of UV line blanketing, which reprocesses absorbed UV light into longer wavelengths. Prior to the 2009-2010 science run which comprises most of the work in this thesis, the most up-to-date model was considered to be that of Metzger et al. (2010), with ejecta mass, $M_{\text{ej}} = 10^{-2} M_{\odot}$ and outflow speed, $v \approx 0.1c$. However, these parameters suffer from uncertainty, with some models providing $0 < M_{\text{ej}} < 0.1 M_{\odot}$ and $0.1c < v < 0.2c$, along with initial electron fractions, Y_e , of the material, ranging from 0.1 to 0.4. With more recent models described in section 5.2.4 and a tentative first detection as described in 5.2.5, it is hoped that future work may help improve these uncertainties.

Supernovae

As mentioned earlier in this section, some CCSNe can follow the collapsar model, producing relativistic jets which we see as LGRBs. Regardless of the creation of an LGRB, it is possible for a CCSNe to produce GWs, again through asymmetric mass distributions, which are thought to be barely detectable for the local group, and more likely to be only detectable within our own galaxy. Therefore, any detectable GW emission from a CCSN should also result in EM radiation that is easily detectable with partner observatories. Again, see Ott (2009) for an overview of GW emission from CCSNe.

Cosmic Strings and ‘The Unknown’

A more exotic, theoretical source of GWs and possible EM counterparts exists in the form of Cosmic String Cusps (Siemens et al., 2006). These hypothetical, 1-dimensional defects in space-time could theoretically decay by GW and EM emission. However, since

they are currently entirely theoretical, we do not consider them in detail for the work described here.

It is also possible, as with the opening of new EM windows on the universe, that we may find entirely new and unpredicted sources of GW and EM radiation.

2.1.2 EM Triggered GW Searches

Previous efforts to pair GW and EM observations have been attempted, using detected EM transients (such as GRBs) to trigger searches of GW data taken in coincidence. The most recent example is based on analysing GW data taken during the 2009-2010 science run (Abadie et al., 2012c), which was split into two observing periods: ‘Winter Run’ - from December 2009 to January 2010, and ‘Autumn Run’ - from September to October 2010. These dates correspond to the time in which LIGO and Virgo were in observation modes, designated Science-run 6 (S6) and Virgo Science Runs 2 and 3 (VSR2/3) respectively. During this time 155 GRBs were detected and reported via the GRB Coordinates Network (GCN). Given that the sky positions of these bursts are generally well known, typically less than a degree, GW data analysis is made simpler as the differences in the predicted time-of-arrival for each GW detector can be estimated. For ‘blind’ searches, the analysis pipelines must search across all possible GW arrival times. In the GRB triggered searches, all GRBs are searched for using unmodelled burst algorithms, while SGRBs are also searched for in the GW data by looking for signals which match theoretically modelled waveforms. For the GRBs detected during the 2009-2010 science run no GW counterparts were found, however we can still place lower distance limits on the sources at 90% confidence levels. For unmodelled burst sources if we assume (optimistically) that the sources radiate $10^{-2} M_{\odot} c^2$ in GW energy, then the GRBs are located at distances greater than 17 Mpc. For modelled sources, we can exclude NS-NS (NS-BH) mergers within distances of 17 Mpc (29 Mpc). While these

distance limits are small compared to known distances to GRBs (for example, the closest GRB detected, GRB 980425 associated with SN 1998bw, was at a distance of 34 Mpc), they can be used to exclude GRBs with no known distances. Two such examples are those of GRB 051103 and GRB 070201. GRB 051103 was an SGRB which was found to appear close to the galaxy M81. If this was a NS-NS merger, the authors can exclude M81 as the host galaxy with 98% confidence. This leaves two possible scenarios: either the GRB was from a more distant NS-NS merger behind M81, or the GRB is due to a giant Soft Gamma Repeater flare from a magnetar in M81 (Abadie et al., 2012g). Similarly, GRB 070201, another SGRB, was found near the galaxy M31, and a NS-NS merger could be excluded from the galaxy with 90% confidence (Abbott et al., 2008).

2.2 EM Follow-up Program

During the 2009-2010 science run, efforts were made to perform triggered EM observations in response to GW events for the first time. The work described in this thesis was performed as part of the program “Locating and Observing Optical Counterparts to Unmodelled Pulses” (LoocUp), but we will also briefly describe non-optical projects in parallel. Due to the variety of EM emission expected from GW sources, a wide range of observatories were needed. Also, the localisation accuracy on the sky for the LIGO/Virgo network, which depends upon the timing errors in each detector, can span several tens of square degrees (e.g. Fairhurst, 2009). This section describes the telescopes used, the GW analysis pipelines and the strategy required to overcome the difficulties in performing such follow-up programs.

First we list the range of observatories at our disposal, the locations of which are shown in figure 2.3 along with table 2.1 summarising the capabilities of the range of observatories available. Unless stated, the telescopes obtained images using a broadband clear, or white-light, filter. Each telescope is also assigned a target trigger rate, which

is the rate of events sent per week to each observatory, which is related to the False Alarm Rate (FAR) of each trigger, as described in section 2.2.3. Several telescopes also committed to observing several fields for each event sent for observations. The method for choosing which field to observe, as described in section 2.2.3, was applied to produce a series of separate fields of decreasing probability. All telescopes were sent the most likely fields, while those with multiple fields per trigger were given subsequent field locations up to the maximum “Tiles per Trigger” listed below and in table 2.1. All magnitude limits given in this section are calibrated to be equivalent R -band magnitudes.

2.2.1 Optical Instruments

- The Palomar Transient Factory (PTF; Law et al., 2009) is a 7.3 square degree FoV camera mounted on the 1.2 m Oschin Telescope at Palomar Observatory. A 60s exposure detects objects with a limiting magnitude $R = 20.5$. This instrument was only used during the Autumn Run, observing the ten most likely fields over several nights at a rate of 1 trigger every 3 weeks.
- Pi of the Sky (Malek et al., 2009) is a 400 square degree FoV camera, located in Koczargi Stare, near Warsaw. The camera operated by observing the whole error region from the trigger generators over several nights, with exposure times of 10s giving limiting magnitudes of 11–12. The target trigger rate was approximately 1 per week in the autumn observing period.
- The QUEST camera (Baltay et al., 2007), currently mounted on the 1 m ESO Schmidt Telescope at La Silla Observatory, has a 9.4 square degree FoV. The telescope is capable of imaging to a limiting magnitude of $R \sim 20$ with 60s exposures. The QUEST camera was used in both the winter and autumn periods, with a target rate of 1 trigger per week.

- The ROTSE III Network (Akerlof et al., 2003) is a collection of four robotic telescopes spread around the world, as shown in figure 2.3. Each telescope has a 0.45 m aperture, giving a 3.4 square degree FOV. No filter is used, and a 20 s exposure gives an equivalent R -band limiting magnitude of around 17. The ROTSE network was used in the autumn observing period, with a target rate of 1 trigger per week.
- SkyMapper (Keller et al., 2007) is a survey telescope located at Siding Spring Observatory in Australia. The telescope has an equivalent aperture of 1.01 m, a 5.7 square degree FoV, and is capable of reaching a limiting magnitude of ~ 21 with a 110 s exposure. SkyMapper was used in the autumn run with a target rate of 1 trigger per week.
- TAROT (Klotz et al., 2009) is comprised of two robotic 25 cm telescopes, one at La Silla in Chile and one in Calern, France. Each TAROT instrument has a 3.4 square degree FOV, with a 180 s exposure capable of reaching a limiting magnitude of 17.5. The telescope was used in both the winter and autumn observing periods, with a target rate of 1 trigger per week.
- The Zadko Telescope (Coward et al., 2010) is a 1 m telescope located in Western Australia. Zadko is capable of imaging with a FoV of 0.15 square degrees with a limiting magnitude of ~ 20 with a 180s exposure. The telescope was used only in the autumn observing period with a target rate of 1 trigger per week.
- The Liverpool Telescope (LT; Steele, 2001) is a 2 m robotic telescope situated at the Observatorio del Roque de Los Muchachos on La Palma. For the work described here the RATCam instrument, with a 21 square arcminute FoV, was used. A five minute exposure allows us to reach a limiting magnitude of $r' = 21$. For this work, we were originally awarded 8 hours of target-of-opportunity time, split into 8 triggered observations of 1 hour each, with a target rate of 1 trigger

per week. In preparation for the autumn run, I created a Python script which sent these observing requests to the telescope via a program developed to handle target-of-opportunity observations, provided by LT Director Iain Steele.

Importantly, the range of these optical observatories together can cover the range of error regions and the expected magnitude range for SGRB optical afterglows. Using the top right plot of figure 4.6, we can calculate that 1 day after burst an optical afterglow for a SGRB at 50 Mpc, comparable to the distance to which LIGO and Virgo could detect a NS-NS merger during the 2009-2010 science run, would have an apparent optical magnitude of between 12 and 20. The analysis I performed of images obtained by LT and ROTSE is presented in chapter 4.

2.2.2 Radio and X-ray Instruments

The LOw Frequency ARray (LOFAR; Fender et al., 2006) is a dipole array radio telescope based in the Netherlands but with stations across Europe. The array is sensitive to frequencies in the range of 30 to 80 MHz and 110 to 240 MHz, and can observe multiple beams simultaneously. LOFAR was used for the autumn observing period, during which LOFAR was running at a reduced capacity due to commissioning, and accepted triggers at a target rate of 1 per week with a four-hour observation in its higher frequency band, providing a ~ 25 square degree FoV.

Although not used in the prompt search during the science run, the Expanded Very Large Array (EVLA; Perley et al., 2011) was used to follow up a few triggers after the 2009-2010 science run with latencies of 3 and 5 weeks.

The Swift satellite (Gehrels et al., 2004) carries three instruments, each covering different energy/wavelength ranges - the Burst Alert Telescope (BAT - 15-150 keV; Barthelmy et al., 2005), the X-ray Telescope (XRT - 0.2-10 keV; Burrows et al., 2004) and the UV/Optical Telescope (UVOT - 170-600 nm; Roming et al., 2004). The LoocUp

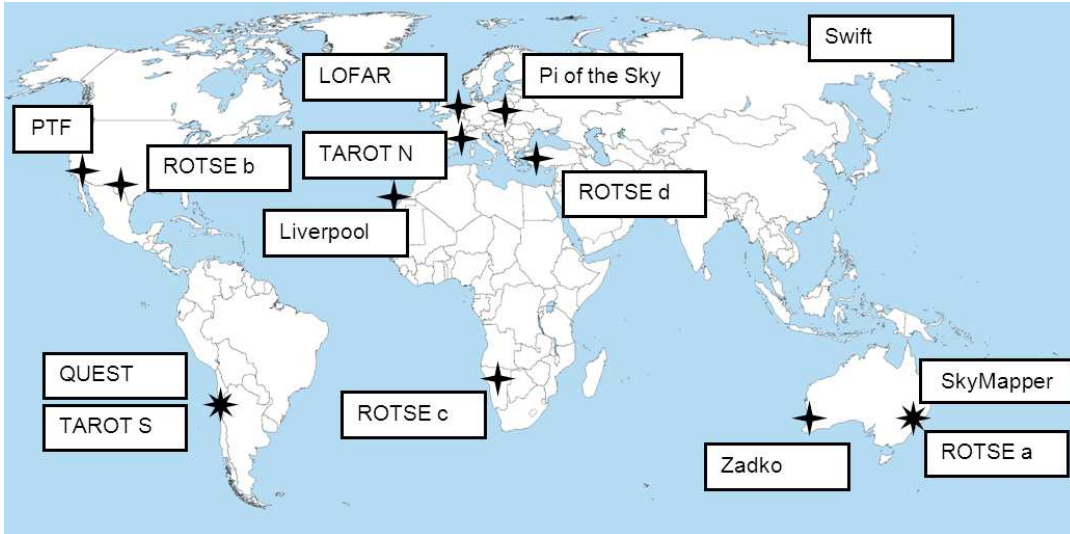


Figure 2.3: A map showing the approximate positions of telescopes that participated in the project. The Swift satellite is noted at an arbitrary location. Reproduced from Abadie et al. (2012e).

follow-up program was granted several target-of-opportunity observations with the XRT and UVOT instruments for the winter and autumn observing periods. The XRT is an imaging instrument with a 0.15 square degree FoV, sensitive to fluxes around 10^{-13} ergs/cm²/s in the 0.5-10 keV band, while UVOT can image with a 0.08 square degree FoV to a limiting magnitude of $B = 22.3$ in a clear filter with a 1000 s exposure.

2.2.3 Follow-up Pipeline

A simplified diagram of the pipeline which produces the observing requests for the telescopes described in this section is shown in figure 2.4. GW data is collected from each interferometer and subsequently analysed by one of 3 analysis pipelines, which run almost in real-time, with only a few minutes delay, which we call trigger generators. These pipelines search the data for signals above a given threshold - a ‘trigger’. These trigger generators search for signals from unmodelled bursts using the Coherent Waveburst (cWB) and the Omega Pipelines, and from modelled compact binary mergers using the Multi-Band Template Analysis (MBTA). The cWB pipeline searches for coherent bursts

Name	FoV (sq. degs)	Aperture (m)	Exposure Time (s)	Limiting Magnitude	Tiles per Trigger	Target Alerts Per Week
PTF	7.3	1.2	60	20.5	10	1/3
Pi of the Sky	400	0.072	10	11.5	1	1
QUEST	9.4	1	60	20.5	3	1
ROTSE III	3.4	0.45	20	17.5	1	1
SkyMapper	5.7	1.35	110	21	8	1
TAROT	3.4	0.25	180	17.5	1	1
Zadko	0.15	1	120	20.5	5	1
LT - RATCam	0.0058	2	300	21	1	1
LT - SkyCamZ	1	0.2	10	18	1	1
LOFAR	~25	N/A	14400	N/A	1	1
Swift - XRT	0.15	N/A	200-5000	N/A	5	1/4
Swift - UVOT	0.078	0.3	200-5000	24	5	1/4

Table 2.1: The EM partner observatories used during the 2009-2010 LIGO-Virgo science run, listing information on the capabilities of each observatory and target trigger rates. Reproduced from Abadie et al. (2012e) and Aasi et al. (2014).

of excess power in the GW strain data, while Omega analyses the data using a selection of templates that are approximately sine-Gaussian, using the assumption that a GW signal can be decomposed into a small series of these waveforms. MBTA searches the data for signals which match the series of waveforms modelled from simulations of compact binary mergers. The range of trigger generators search for a wide range of signal types, with some overlap. This increases the chance of detection, and also can provide verification in the case of a trigger appearing from multiple generators. The trigger generators are discussed in more detail in Abadie et al. (2012e) and Abadie et al. (2012a), and references therein. The triggers produced are then submitted to the Gravitational-wave Candidate Event Database (GraCEDb). The database is monitored in real-time by the LUMIN (LoocUp Monitoring) and GEM (Gravitational to Electro-Magnetic Processor) for statistically significant triggers below a given FAR, as detailed in 2.2.3, which are then passed on for human validation. As a member of the LoocUp team, while ‘on-call’, my job was to verify that the triggers passed to us were of good data quality (DQ). This involved searching the several online DQ verification pages, which list the operating mode

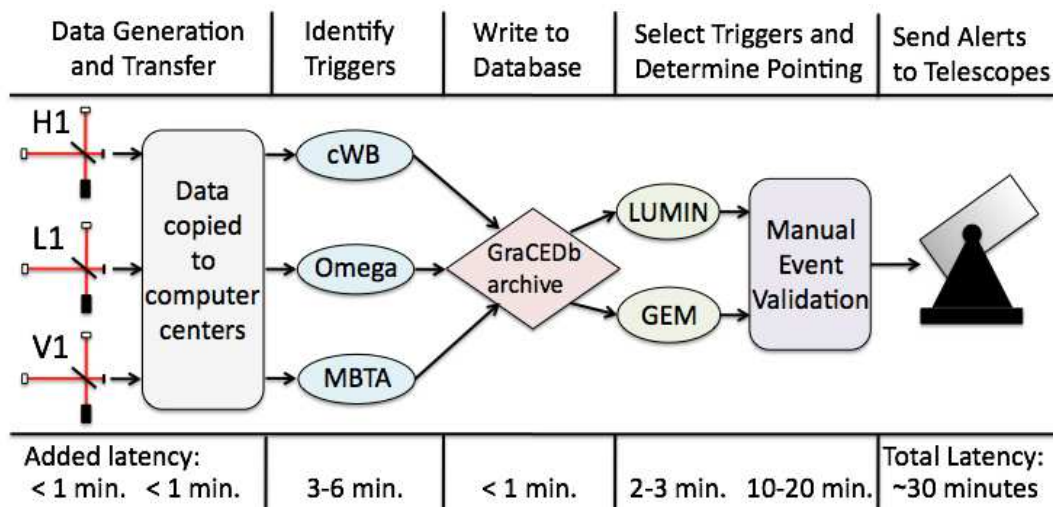


Figure 2.4: A simplified flowchart of the real-time trigger analysis with approximate time requirements for each stage. Reproduced from Abadie et al. (2012e).

of the detectors and other detector site data, checking for any anomalous seismic readings and also telephoning each interferometer site to further ensure no known abnormalities or disturbances occurred at the sites at the time of the trigger, such as a passing train or someone entering the room containing the input/output optics. If an event passes all human verification, observing requests are sent to the partner observatories.

False Alarm Rates

For a trigger to be considered for follow-up observations, we estimated the False Alarm Rate for each trigger. The FAR is the average rate at which noise in the detectors creates events with a similar or greater detection statistic. For example, if a burst signal was detected in the interferometer with a signal-to-noise ratio (SNR) of 5, but random noise in the detector produces triggers of similar or greater SNR every 2 days, that trigger has an FAR of 0.5 events per day. For the winter run, the FAR threshold was set at 1 event per day of coincident detector live-time for ground based telescopes, with a stronger threshold for Swift observations. For the autumn run, the FAR threshold was set at 0.25 events per day for most telescopes, with stronger thresholds for PTF and Swift.

The FAR for the cWB and Omega trigger generators was calculated using methods previously used in all-sky burst searches of GW data (see e.g. Abadie et al., 2010). Data from each of the detectors is artificially shifted in time, so that the time delay is greater than the light travel time between the sites. These unphysical times shifts are then analysed with the same trigger generators, resulting in event rates for triggers due to noise, with no true coincident GW signal. For the burst searches, 100 time shifts of data from between 10 minutes and several hours are constantly analysed, with the FAR calculated for each trigger from the most recent series of time shifts.

For MBTA, since the pipeline is based on modelled waveforms, the FAR of a trigger is calculated in each detector from data collected minutes prior to the trigger of interest, and then combined to produce a FAR for the trigger in all three detectors. This is calculated using information from the previous 200 triggers in each detector prior to the coincident trigger of interest. By calculating the overall probability that a combination of these 3 sets of 200 triggers will produce a false trigger, given the travel time of light between the two detectors. See Marion (2004) and Kanner (2011) for details of the MBTA analysis.

As described earlier in this section, the sky localisation produced by the trigger generators covers several tens of square degrees, and is also irregular in shape (as shown in figures 2.5 and 2.6). Since this is much larger than the FoVs of most of the telescopes used for this follow-up program, we had to produce a method for choosing the most interesting tiles within the whole field to observe. Since the objects we want to observe are expected to be extra-galactic in origin, as discussed in chapter 1, it follows that the distribution of galaxies within the localised regions should be used as a prior for deciding which tiles to observe. To do this we created the Gravitational Wave Galaxy Catalogue (GWGC), as described in chapter 3.

Galaxy Weighting

The trigger generators provide positional information in the form of a sky map, which gives the probability of a given position on the sky containing the true GW signal. Each pixel in the sky map covers an area of $0.4^\circ \times 0.4^\circ$, and only the top 1000 pixels are retained from each trigger, giving typical sky map areas of 160 square degrees. By combining the probabilities in each pixel with prior knowledge of the distribution of galaxies, we can prioritise the regions to be observed by our follow-up partner observatories. While the sources we hope to detect also exist in our own galaxy, the expected rate of signals from the Milky Way is low, and the expected EM emission is likely to be bright enough to be easily visible. For this reason, the weighting algorithms described in this section assumed sources to be extragalactic in origin.

For both burst and MBTA triggers, the blue light luminosity of a galaxy is used as an estimate of the mass of a galaxy, as blue luminosity indicates ongoing star-formation, which was argued to correlate with NS-NS merger rates (Phinney, 1991), as mentioned in chapter 3. Burst triggers assign galaxy weighting using a method similar to that described in Nuttall & Sutton (2010). Each pixel is assigned the following unnormalised likelihood, P_{pix} :

$$P_{\text{pix}} = \sum_i \frac{L_i P_{\text{GW}}}{D_i}, \quad (2.1)$$

where P_{GW} is the likelihood based on the GW data alone, and L_i and D_i are the blue light luminosity and distance of an associated galaxy from the GWGC. The sum i is over all galaxies which lie within each sky map pixel out to a distance of 50 Mpc, which is the most likely maximum distance that a compact binary merger containing a NS could have been detected during the 2009-2010 science run. For objects which have angular sizes greater than the pixel size, the luminosity of the object is split evenly across each pixel located within the ellipse defined by the major and minor axes of

the galaxies in the GWGC. Once the calculation has been performed for each pixel, the whole sky map is normalised such that the total likelihood is unity. For MBTA triggers, it is possible to estimate some of the physical parameters of the source based on the matched theoretical waveforms. Primarily, this can give a minimum distance to a detected source, allowing us to restrict objects in the galaxy catalogue to those between the measured minimum distance and 50 Mpc. Therefore, for triggers from MBTA, each pixel is uniformly weighted by the fraction of the total luminosity of the galaxies, found within the distance limits provided, contained in that pixel:

$$P_{\text{pix}} = \sum_i L_i^{\text{frac}} P_{\text{GW}}, \quad (2.2)$$

where the sum is over all objects associated with the pixel, and $\sum_k L_k^{\text{frac}} = 1$. In the unlikely event that a sky map does not contain a single object from the GWGC, the likelihood from each pixel is taken from the GW data only ($P_{\text{pix}} = P_{\text{GW}}$). In all cases, the coordinates provided for follow-up are selected to contain the highest total likelihood in the FoV of the instrument. If multiple tiles are allowed, the next highest likelihood tiles are also sent.

Particular care must be taken for observing requests sent to the LT, Zadko and Swift observatories due to their narrow FoV. For Swift, in cases where the weighted pixel with the highest probability contains a single galaxy, the coordinate given is the central location of the galaxy given in the GWGC. If multiple galaxies are found, or the galaxy extends across multiple pixels, the central pixel coordinate is given. For the LT and Zadko, I wrote code which uses equation 2.1 to assign a likelihood for each individual galaxy in the error regions, with the highest ranking galaxy visible chosen for observation.

2.2.4 EM Follow-up Events

During the winter run, the ‘on-call’ team received nine trigger alerts. Three of these triggers were vetoed due to DQ issues. Of the remaining six triggers, 4 were rejected as unobservable by the scheduling software of the limited number of telescopes available for the winter run. In addition, two triggers with FARs marginally below threshold were chosen to increase the collected data set. In total, 4 triggers were imaged with the QUEST and TAROT observatories, as shown in table 2.2. In the autumn run, seven triggers were alerted for human verification, of which one was rejected due to DQ concerns. Of the six triggers sent for observations by partner telescopes, one was rejected by scheduling, as the trigger was found to lie close to the Sun. Trigger G18666 was imaged by ROTSE, but was quickly determined as unusable due to a software bug providing an incorrect sky location. The four remaining triggers were imaged by a variety of telescopes, as shown in table 2.2. Two of these triggers were initially found with exceptionally low FARs of <0.025 events per day. Trigger G19377 was found to be a blind injection, and is described in section 2.2.5. Trigger G21852 was given a FAR of 0.023 events per day, or one event for 44 days of coincident observations. This means that for 44 days of coincident observation, we expect to see 1 event passing the trigger thresholds purely due to random noise. Given that the interferometers ran in coincidence for a total of 52 days, this trigger is actually consistent with detector noise. The sky maps produced as part of the pipeline before galaxy weighting had been applied, along with the tiles observed by various telescopes, can be found in figures 2.5 and 2.6 for the winter and autumn runs, respectively. The analysis of the Liverpool Telescope and ROTSE images can be found in chapter 4, the results from the other optical telescopes can be found in Aasi et al. (2014), and the analysis of the Swift satellite observations can be found in Evans et al. (2012).

ID	Date	UTC	Trigger Generator	FAR (day ⁻¹)	Follow-up Images
<i>Winter:</i>					
G3821	Dec 29 2009	15:16:33	Omega	0.66	QUEST collected 12 images.
CWB1	Jan 03 2010	20:37:22	cWB	1.3	Alert sent Jan 7; TAROT collected 6 images.
G4202	Jan 06 2010	06:49:45	Omega	4.5	QUEST collected 9 images.
CWB2	Jan 07 2010	08:46:37	cWB	1.6	QUEST collected 12 images, Swift-XRT 10.
<i>Autumn:</i>					
G19377	Sep 16 2010	06:42:23	cWB	< 0.01	ROTSE collected 117 images, TAROT 20, Zadko 129, SkyMapper 21 and Swift-XRT 6.
G20190	Sep 19 2010	12:02:25	MBTA	0.16	ROTSE collected 257 images, QUEST 23, Zadko 159, and TAROT 3.
G21852	Sep 26 2010	20:24:32	cWB	0.02	ROTSE collected 130 images, PTF 149.
G23004	Oct 3 2010	16:48:23	Omega	0.21	ROTSE collected 153 images, QUEST 40, Liverpool - RATCam 22, Liverpool - SkyCamZ 121, and POTS 444.

Table 2.2: Triggers observed during the 2009-2010 science run, listing the time of the trigger, the trigger generator and the images taken by partner optical telescopes. Reproduced from Aasi et al. (2014).

2.2.5 Blind Injection Challenge

In order to increase the confidence of a true detection, during each science run, an unknown number of test signals are injected into the detector or the output data during scheduled science runs. For transient signals, the End Test Masses are oscillated using the magnets which keep the mirrors aligned. The details of the “blind injections” are decided upon by a few LIGO-Virgo collaboration members. Nobody outside of this select group knows exactly what time, what type or how many (if any) injections are going to occur, details of which are kept hidden in a metaphorical ‘envelope’ (in reality a folder on a USB thumb drive kept safe). This provides an end-to-end test of the detection and analysis capabilities and also prevents premature claims of detection by “rogue scientists”, as the true nature of any detection is not known until the envelope is opened. Previous examples of such blind injection challenges can be found in Abadie et al. (2012f) and Abadie et al. (2012d).

During the 2009-2010 science run, one such blind injection was detected¹, details of which can be found in Abadie et al. (2012b) Trigger G19377 was detected at UTC 06:42:22.955 on 2010 Sep 16 with a FAR of less than one event per 7000 years. The trigger was quickly identified to have a similar evolution to that of a chirp signal, typical of a compact binary merger. The initial sky map used for follow-up observations can be seen in figure 2.6(a). Since the most likely location was found to be near the Canis Majoris constellation, this trigger was given the moniker “The Big Dog”, with an official name of GW100916. Detailed “offline” analysis using a larger selection of theoretical waveforms provided several estimated parameters. The source was estimated to be a compact binary with component masses $5.4 < M_1 < 10.5 M_\odot$ and $2.7 < M_2 < 5.6 M_\odot$, at a distance of between 7 and 60 Mpc. As with previous science runs, if a possible detection is made, the presence of any injections are not announced until a full analysis has been performed, results gathered in a paper and presented at a collaboration meeting.

¹A description of the blind-injection analysis can be found at www.ligo.org/news/blind-injection.php

If the analysis is approved, then the ‘envelope’ is opened to see if any blind injections were the cause of the detections. At the LIGO-Virgo meeting on 14th of March 2011, the envelope was opened, and the Big Dog event was found to be one such injection. However, the estimated parameters were found to be incorrect. One of the masses injected was supposed to be a $1.4 M_{\odot}$ neutron star, and the injected sky location was not in Canis Majoris. However, subsequent analysis found that the injection software used contained two bugs, which would not have been found if not for the blind injection challenge. First, an older waveform was used, causing the mass error, and a sign error in the code for one detector produced the incorrect location. Despite the lack of a real detection, the fact that the blind injection was found gives us confidence that our analysis methods are capable of finding such objects in the near future.

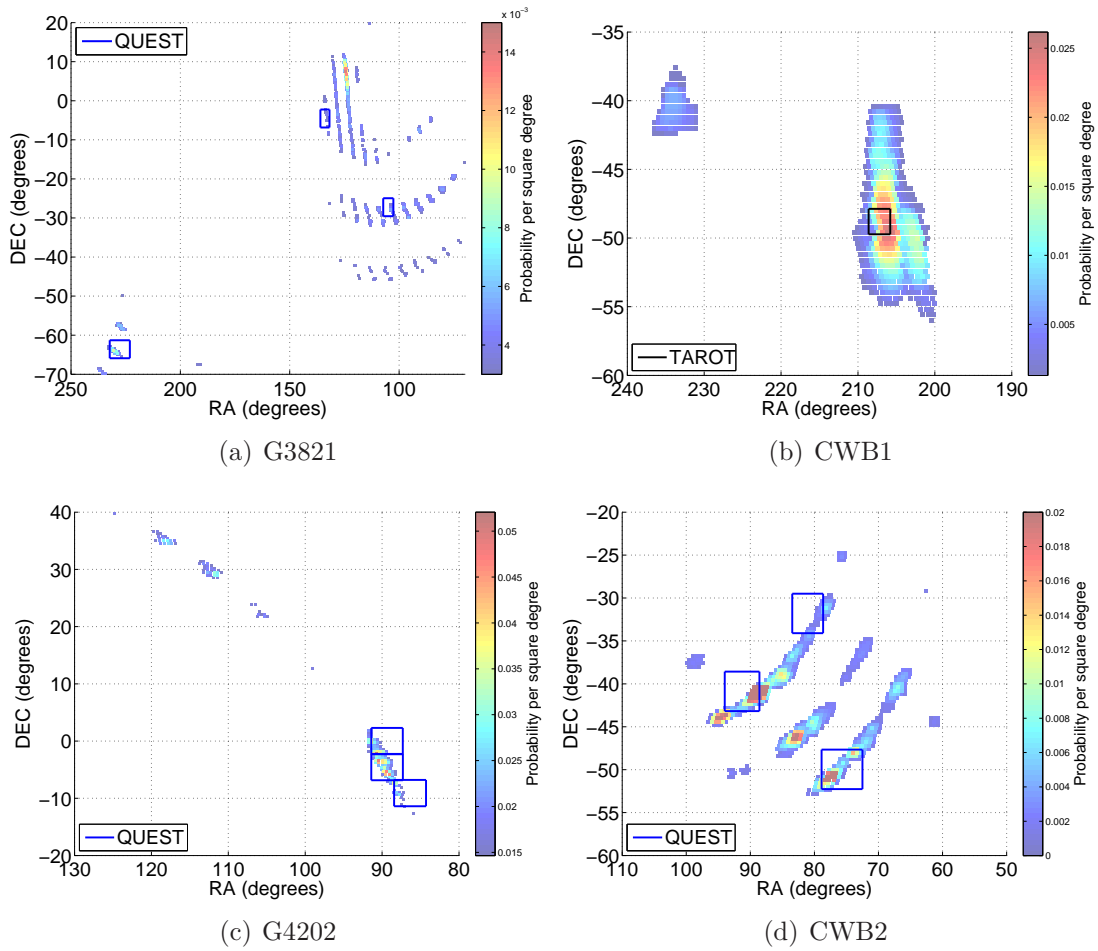


Figure 2.5: The sky maps used for observing requests during the winter observation run, prior to galaxy weighting. The coloured boxes represent the fields observed by each of the telescopes listed, after galaxy weighting was applied. Reproduced from Aasi et al. (2014).

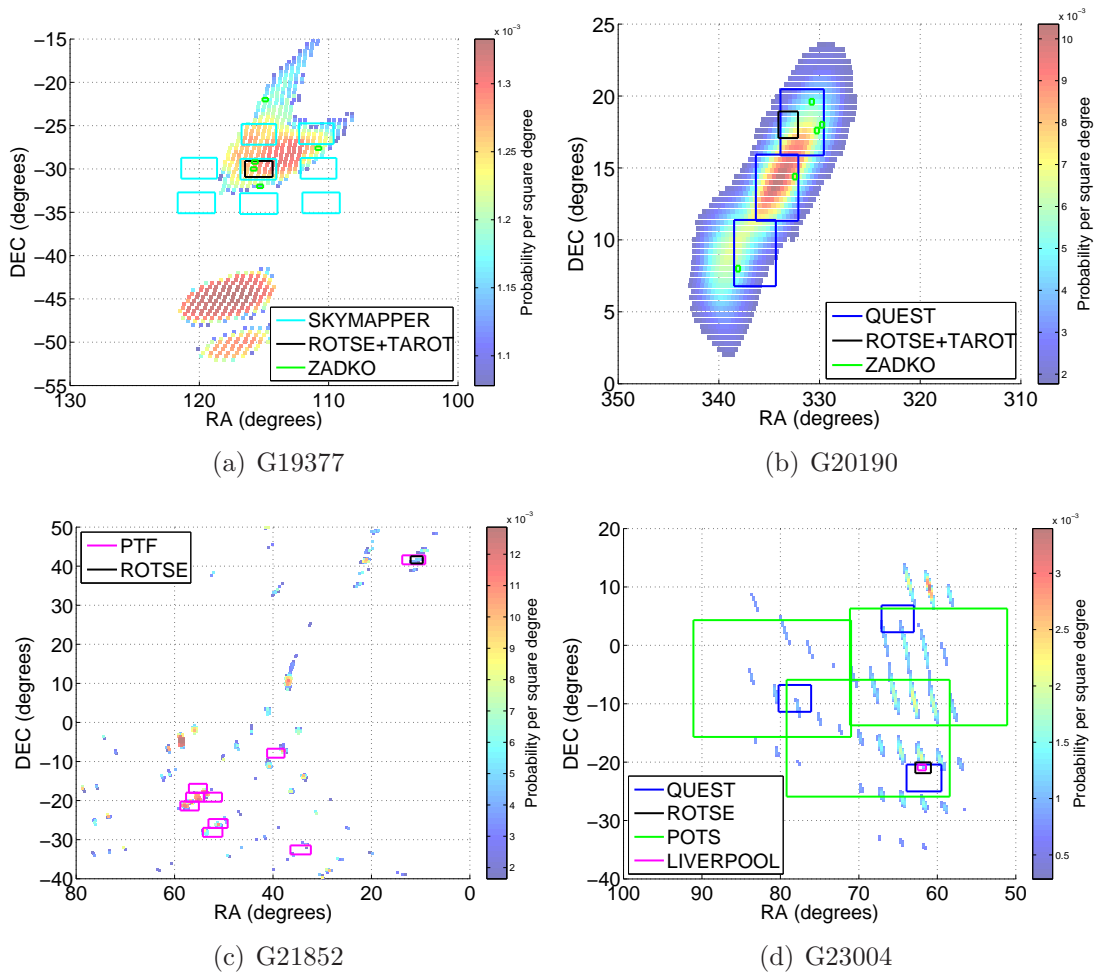


Figure 2.6: Same as figure 2.5, but for triggers during the autumn observation run.

Chapter 3

GWGC: The Gravitational Wave Galaxy Catalogue

This chapter describes the creation of a new list of galaxies within 100 Mpc for the 2009-2010 science run. Work described in this chapter is based on previously published work. Sections 3.1 - 3.3 are based on my work described in White, Daw & Dhillon (2011) in compiling and analyzing the GWGC. Section 3.4.1 is based on Kanner et al. (2012), in which I created an updated version of the GWGC to include I-band magnitudes.

3.1 Motivation for the GWGC

As detailed in section 2.2, the typical error regions on the sky produced during the 2009-2010 LIGO-Virgo science run was generally much larger than the field of view of optical telescopes. Therefore a galaxy catalogue is required to locate the ideal regions to be imaged by telescopes with a smaller field of view within the LIGO/Virgo error region. There are also many EM transients in the sky. How are we to know if a particular EM transient observed in the error circle of LIGO-Virgo is genuinely associated with the GW transient source? Kulkarni & Kasliwal (2009) find that foreground “fog” (asteroids, M-dwarf flares, dwarf novae) and background “haze” (distant, unrelated SNe) result in a significant chance of detecting an unrelated EM transient in a typical LIGO-Virgo

error circle. Fortunately, the expected sensitivity of the LIGO and Virgo interferometers in 2010 is a blessing in disguise here: it places a ~ 40 Mpc horizon on the majority of GW sources (Abbott et al., 2009a; Acernese et al., 2008). This means that we can restrict EM follow-up to only the galaxies present within the LIGO-Virgo error circle, as plausible GW transient sources (e.g. GRBs) are far more likely to be extragalactic than Galactic in origin. This reduces the foreground fog and background haze by three orders of magnitude (Kulkarni & Kasliwal, 2009).

Efforts to create a suitable galaxy catalogue has already been attempted by Kopparapu et al. (2008), with the publication of the Compact Binary Coalescence Galaxy (CBCG) catalogue, containing 38,757 galaxies. When published it was claimed to be the most complete catalogue of galaxies within 100 Mpc. Only galaxies with a blue luminosity of $L_B \geq 10^{-3}L_{10}$ were included, where $L_{10} = 10^{10}L_{B,\odot}$ and $L_{B,\odot} = 2.16 \times 10^{33}$ ergs/s, which is calculated using $M_{B,\odot} = 5.48$. This cut was made as it is argued that in the nearby universe the compact binary coalescence rate is expected to follow the star formation rate (Phinney, 1991), which is traced using blue light. However, this catalogue was not considered suitable for the 2009-2010 joint science run. First, the blue magnitude cut could potentially ignore galaxies that are faint in the blue region of the spectrum. Kopparapu et al. (2008) assumed that blue light traced the likelihood of neutron star merger, but as we see later in section 3.4 this may not be accurate, and so may not be the best choice of cut. Second, we found that the method of compilation of the CBCG introduced a series of errors, primarily revolving around inaccurate positioning information resulting in degeneracies within the catalogue. A startling example of this was the inclusion of very bright, well-known nearby galaxies being included at least twice due to their positions being stated in both J2000 and B1950 co-ordinates in different source catalogues.

In this chapter we describe the compilation of a new galaxy catalogue¹, which we

¹<http://cdsarc.u-strasbg.fr/viz-bin/Cat?VII/267>

call the Gravitational Wave Galaxy Catalogue (GWGC; White, Daw & Dhillon, 2011), providing a more complete, up-to-date sample created from a variety of literature sources extending out to 100 Mpc, which is as unbiased as possible to a particular type of gravitational wave source, and includes a unique identifier for each galaxy taken from HyperLEDA (Paturel et al., 1989, 2003). The GWGC contains a total of 53,225 galaxies within 100 Mpc and 150 Milky Way globular clusters. This catalogue is currently being used in the search for electromagnetic counterparts by the LIGO/Virgo collaboration (Kanner et al., 2008), and several data analysis groups in the collaboration (e.g. Nuttall & Sutton, 2010). In section 3.2 we describe how the catalogue was compiled and the parameters it contains, as well as how the parameter errors were calculated. In section 3.3 we discuss the completeness of the GWGC in comparison to the CBCG catalogue and results from the Sloan Digital Sky Survey (Abazajian et al., 2003).

3.2 Catalogue Compilation

In order to improve on currently available catalogues of nearby galaxies, a larger, more up-to-date sample of galaxies was required. We also aimed to improve the simplicity of incremental updates to the catalogue and minimise the risk of degeneracy within the catalogue itself, compared to similar catalogues. We achieved this by using scripts to create the GWGC from a subset of 4 large catalogues, each of which employs a unique Principal Galaxy Catalogue (PGC) number for each galaxy (Paturel et al., 1989). These catalogues are: an updated version of the Tully Nearby Galaxy Catalog, the Catalog of Neighboring Galaxies, the V8k catalogue and HyperLEDA. These are freely available online but a local, homogeneous list is essential for rapid follow-up purposes with LIGO and Virgo. A single, local catalogue also ensures that all working groups within the LIGO/Virgo Collaboration are using the same sources for both real-time and off-line analyses.

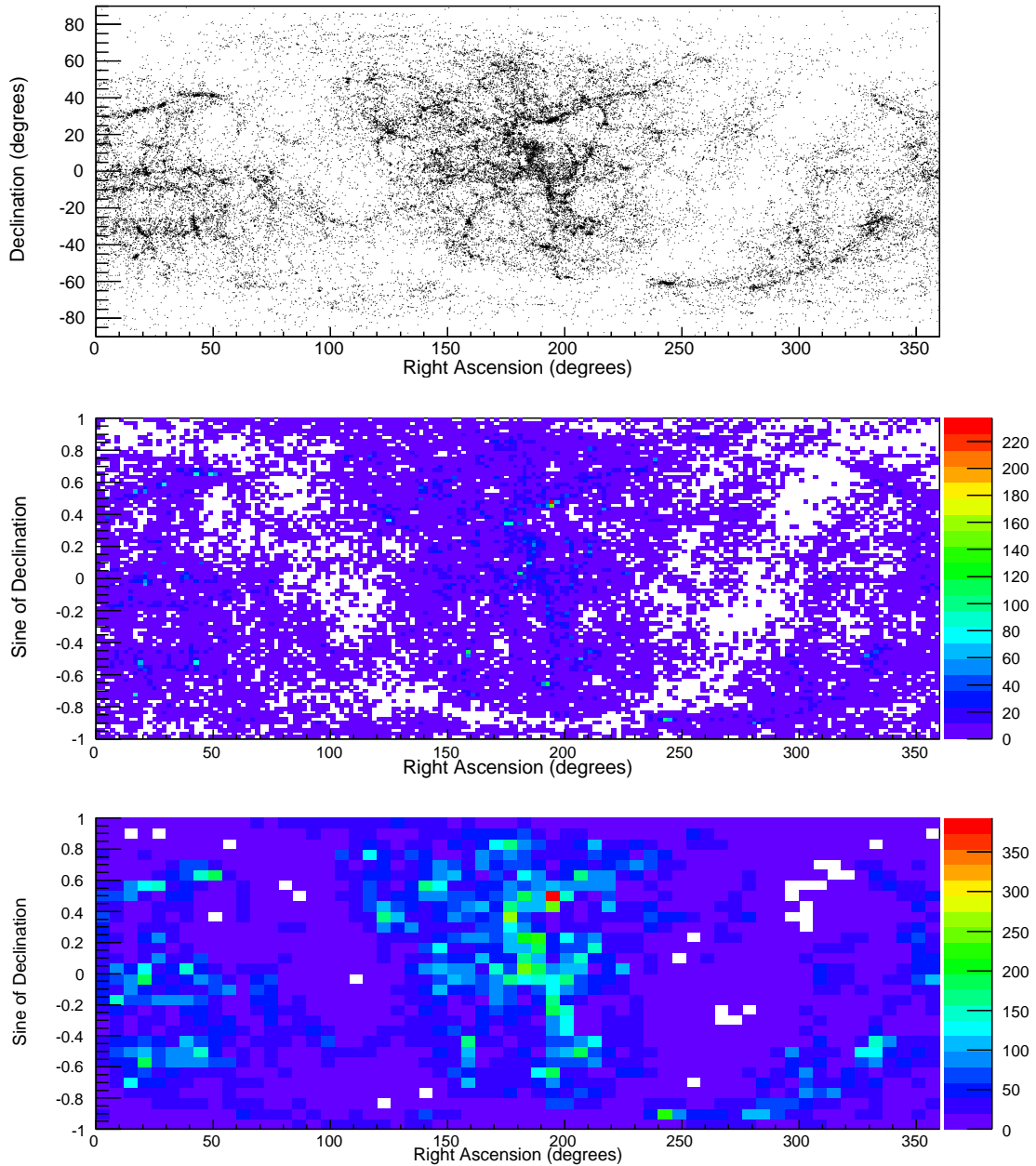


Figure 3.1: Scatter plot showing distribution of galaxies in GWGC on the sky (top), and the distribution in ~ 2 degree bins (middle) and 6 degree bins (bottom). The choice of bin size represents the best and median error circles on the sky obtainable with the LIGO/Virgo network of detectors (Fairhurst, 2009). This highlights the importance of using a list of nearby galaxies, as we must choose the best fields within a LIGO/Virgo error circle to observe. Reproduced from White, Daw & Dhillon (2011).

The Tully Nearby Galaxy Catalog (Tully, 1987), hereafter referred to as Tully3000, is comprised of galaxies with a recession velocity $V < 3000 \text{ km s}^{-1}$ ($\sim 42 \text{ Mpc}$ for $H_0 = 72 \text{ km s}^{-1} \text{ Mpc}^{-1}$). The most recent release of Tully3000 can be found in the Extragalactic Distance Database² (Tully et al., 2009). A subset of these galaxies with high quality distance measurements were used to investigate the Local Void (Tully et al., 2008). Tully3000 also contains galaxies surveyed as part of the Hubble Space Telescope (HST) Key Project to measure the Hubble constant (Freedman et al., 2001).

The Catalog of Neighboring Galaxies, by Karachentsev et al. (2004), is compiled from the literature and contains galaxies with a distance of $D \lesssim 10 \text{ Mpc}$ or a radial velocity of $V < 550 \text{ km s}^{-1}$ ($D \lesssim 7.6 \text{ Mpc}$ for $H_0 = 72 \text{ km s}^{-1} \text{ Mpc}^{-1}$), and contains the less luminous Dwarf Spheroidal (dSph) and Dwarf Irregular (dIr) galaxies often missed by larger surveys.

The V8k catalogue (Tully et al., 2009) is another catalogue compiled from the literature, extending out to radial velocities $V < 8000 \text{ km s}^{-1}$. Drawing heavily on the ZCAT survey³, as well as other literature sources, the V8k catalogue excludes results from directional surveys such as the Sloan Digital Sky Survey (SDSS), Six-degree-Field (6dF) Galaxy Survey (Jones et al., 2004) and Two-degree-Field (2dF) Galaxy Redshift Survey (Folkes et al., 1999), to provide a catalogue that is as uniform as possible across the sky out to a recession velocity of $V < 8000 \text{ km s}^{-1}$. HyperLEDA⁴ (Paturel et al., 1989, 2003) is also used to provide supplemental data where possible (for example, position angles). We also include a list of 150 known Milky Way globular clusters (Harris, 1996). Some of these are listed in HyperLEDA, and the respective PGC numbers are included where possible.

In order to be of use in the analysis and follow-up of gravitational wave data certain galaxy parameters are required to be determined as accurately as possible. These pa-

²<http://edd.ifa.hawaii.edu/>

³<http://www.cfa.harvard.edu/~huchra/zcat/>

⁴<http://leda.univ-lyon1.fr/>

Column	Abbreviation	Description
1	PGC	Identifier from HYPERLEDA
2	Name	Common name
3	RA	Right ascension (decimal hours, J2000)
4	Dec	Declination (decimal degrees, J2000)
5	Type	Morphological type code
6	App_Mag	Apparent <i>B</i> -band magnitude
7	Maj_Diam	Major diameter (arcmins)
8	err_Maj_Diam	Error in major diameter (arcmins)
9	Min_Diam	Minor diameter (arcmins)
10	err_Min_Diam	Error in minor diameter (arcmins)
11	b/a	Ratio of minor to major diameters
12	err_b/a	Error on ratio of minor to major diameters
13	PA	Position angle of galaxy (degrees from North through East, all $< 180^\circ$)
14	Abs_Mag	Absolute <i>B</i> -band magnitude
15	Dist	Distance (Mpc)
16	err_Dist	error in Distance (Mpc)
17	err_App_Mag	error in Apparent blue magnitude
18	err_Abs_Mag	error in Absolute blue magnitude

Table 3.1: A description of the columns in the GWGC. Reproduced from White, Daw & Dhillon (2011).

rameters are the distances, diameters and blue magnitudes of the galaxies, as described below. Table 3.1 shows the columns in the GWGC.

3.2.1 Spatial Distribution of Galaxies

The distribution of galaxies on the sky is far from uniform, as shown in figure 3.1. In the centre, the dense region is looking towards the Virgo cluster, and is also the primary region of observation in the SDSS survey. The empty region which traces a sinusoidal shape on the sky is the “Zone of Avoidance”, in which gas and dust in the plane of the Milky Way obstructs our view. Offset by approximately +70 degrees in RA from the zone of avoidance, and with a similar shape, is the super-galactic plane, a sheet of galaxies in which the Virgo cluster and our galaxy reside. This is most clearly visible

Source Catalogue	No. of galaxies
Catalog of Neighboring Galaxies	120
Tully3000	3,496
V8k	17,602
HyperLEDA	32,007

Table 3.2: A table of the contributions of unique galaxies from the selection of source catalogues. The GWGC was constructed hierarchically, where each source catalogue in turn provides the number of galaxies listed, plus any additional data for galaxies already found in previous source catalogues.

towards the bottom right in the upper panel of figure 3.1. On the left, we can also see dense strips of galaxies, which are due to the SDSS survey.

3.2.2 Distances

Accurate distances are important for electromagnetic follow-up observations as gravitational wave detectors have maximum distances at which expected sources are detectable. For example, the GWGC extends to 100 Mpc but the maximum detectable distance for a $1.4 M_{\odot}$ binary neutron star inspiral is in the region of 30 Mpc for detectors during the 2009-2010 LIGO-Virgo science run (Abbott et al., 2009b). An erroneous distance could cause a galaxy which is actually within 30 Mpc to be missed. Similarly, it is possible that coincident detection of inspiral signals can be used to not only constrain position on the sky, but also a maximum and minimum distance to the source (Abbott et al., 2009b), effectively giving us a region of space in which several possible host galaxies may lie. Inaccurate distances could again cause a galaxy to be missed. Ensuring that the galaxies in the GWGC have accurate distances is therefore vital.

Each of the sub-catalogues in the GWGC contain distance measurements using a variety of methods, so we must estimate the accuracy of each method when not provided. The Tully3000 catalogue, which provides 3,496 galaxy distances to the 53,225 contained within the GWGC, contains 3 groups of measurements:

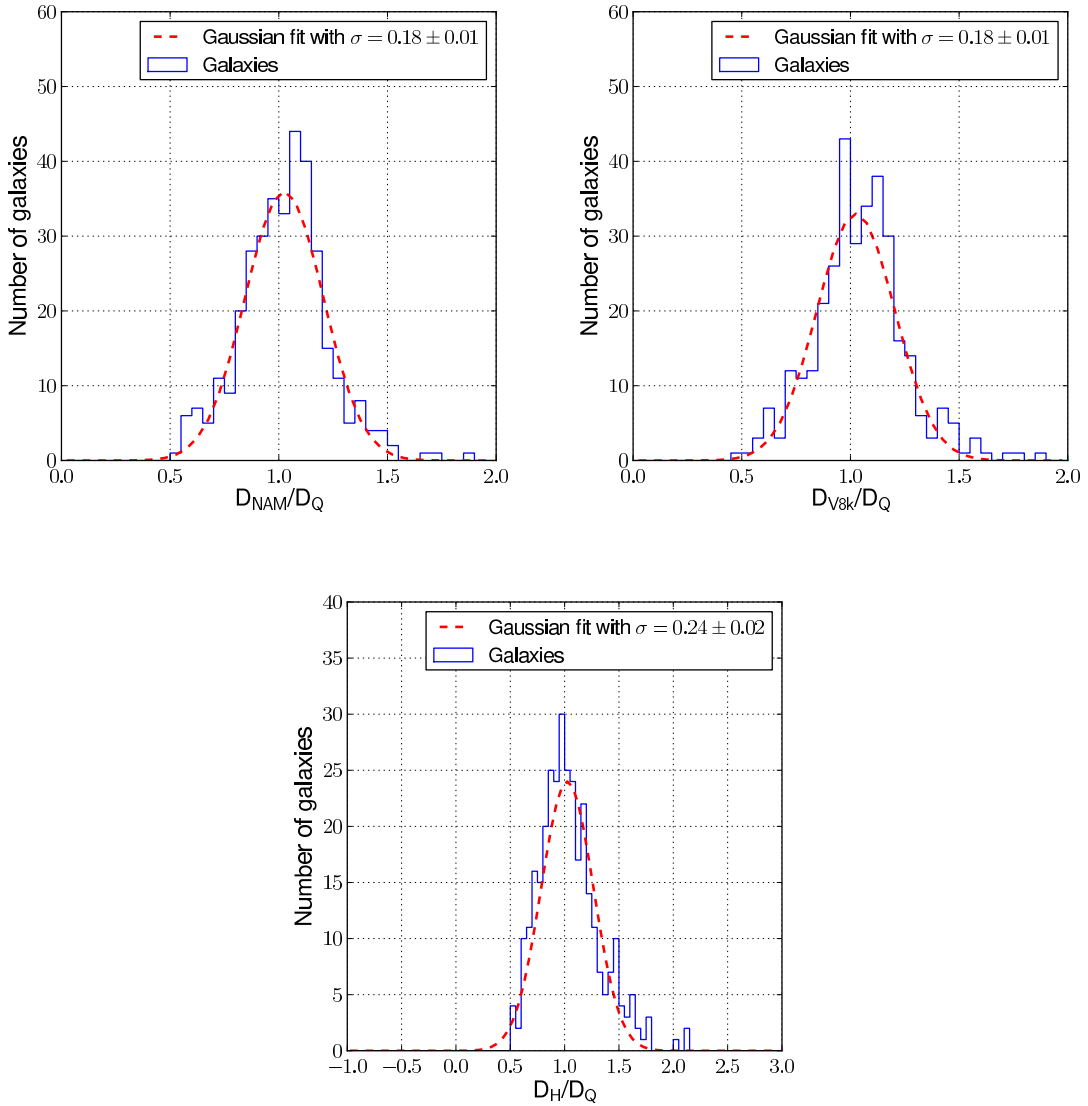


Figure 3.2: Comparison of distance measurements above 10 Mpc for the same galaxies using different methods. Measurements in (a) are for the same galaxies appearing in the Tully3000 catalogue with both quality (D_{Q}) and NAM (D_{NAM}) distances. Those in (b) are for galaxies with D_{Q} distances from Tully3000 that also appear in the V8k catalogue (D_{V8k}). (c) shows those galaxies with D_{Q} distances that appear in HyperLEDA with distances (D_{H}) calculated using v_{vir} . Reproduced from White, Daw & Dhillon (2011).

- “Quality” distance measurements (named due to the low estimated errors) obtained using one of the following methods:
 - The period-luminosity relation of Cepheid variable stars (Leavitt & Pickering, 1912).
 - The surface brightness fluctuation, where the amplitude of the luminosity fluctuation between pixels of a high signal-to-noise CCD image of a galaxy is inversely proportional to the distance, as the variation in brightness between pixels is due to unresolved stars, which are not uniformly distributed throughout the galaxy (Tonry & Schneider, 1988).
 - The tip of the red giant branch, which uses the apparent magnitude of the brightest stars in the red giant branch of a Hertzsprung-Russell diagram and the I -band absolute magnitude of stars undergoing the helium flash stage of evolution, thought to be ≈ -4.0 (Lee, Freedman & Madore, 1993).

The HST Key Project distance measurements using Cepheid variable stars in the Tully3000 catalogue, as described in section 3.2 have small ($<10\%$) errors. This is comparable to errors on the other quality measurements in Tully3000, which are estimated to be 10% (Tully et al., 2008).

- HI luminosity-line width distances measured using the Tully-Fisher (T-F) relation. Doppler broadening of the 21cm neutral hydrogen line is used to measure the rotational velocity of the galaxy, which is then used to estimate mass and, subsequently, luminosity. Combined with apparent magnitude, we can therefore estimate a distance. Distance measurements obtained using luminosity-line width observations are assigned an error of 20% (Tully et al., 2008).
- Distances converted from recession velocities using Hubble’s law, corrected for infall towards the Virgo cluster using an evolved dynamical mass model of the

local universe, the Numerical Action Model (NAM) by Shaya, Peebles & Tully (1995). These are hereafter referred to as NAM distances, with errors calculated in the final paragraph of this section.

Distances in the Catalog of Neighboring Galaxies (an additional 120 galaxies) are measured using several methods: Cepheid variables, tip of the red giant branch, surface brightness fluctuation, T-F relation, the brightest star luminosity (where the average apparent B-band magnitude of resolved stars can be used to estimate the distance modulus as described in Drozdovsky & Karachentsev (2000)), galaxy group membership (where the distance is estimated by assuming membership to a group or cluster in which a galaxy distance is known via other methods) and Hubble's law, in order of decreasing accuracy. Where more than one measurement is available for a galaxy the most accurate measurement is quoted. None of these distances are published with errors so we assign the same fractional errors to distances from the Catalog of Neighboring Galaxies using the same distance measurement method as Tully3000. For sources where distance was measured using a method not in Tully3000, the distances are given fractional errors as calculated for galaxies taken from HyperLEDA, which we calculate in the final paragraph of this section.

Distances in V8k are primarily converted from redshift measurements using Hubble's law, after correcting for Virgo infall using the NAM model by Shaya, Peebles & Tully (1995), as used for the Tully3000 catalogue. This catalogue, which provides 17,602 galaxies with distances within 100 Mpc to the GWGC, also does not provide errors, so we must estimate them using the method used in the final paragraph of this section.

HyperLEDA only gives recession velocities corrected for infall towards the Virgo cluster (v_{vir} , using a different model for Virgo infall⁵), without errors. We did not include any galaxies with $v_{\text{vir}} \leq 500 \text{ km s}^{-1}$ (7 Mpc assuming $H_o = 72 \text{ km s}^{-1} \text{ Mpc}^{-1}$) from HyperLEDA, as below this redshift-based distances are highly uncertain due to the

⁵see <http://leda.univ-lyon1.fr/leda/param/vvir.html> and references therein for full corrections

influence of the local group and limitations of corrections due to Virgo infall for local galaxies. Fortunately, the use of Tully3000 and the Catalog of Neighboring Galaxies are thought to give us a high level of completeness in the local universe. From HyperLEDA, we included 32,007 galaxies with distances within 100 Mpc.

Errors are strongly dependent on measurement method. However, only quality distances and T-F distances in Tully3000 and the Catalog of Neighboring Galaxies have error estimates based on distance measurement method. Therefore, in order to provide an error estimate for distances measured using other methods, we use galaxies which have multiple distance measurements. By plotting the ratio of two different distance estimates to the same galaxy and using a best fit Gaussian, we can determine the errors associated with methods with no published error estimates, as shown in figure 3.2. Comparison between the quality measurements in Tully3000 and NAM distances give a best fit Gaussian with $\sigma = 0.18$. Given that $\sigma = 0.10$ for quality distance measurements, subtracting in quadrature gives fractional errors of 0.14 for NAM distances. Applying the same method to the V8k and HyperLEDA catalogues gives $\sigma = 0.18$ and $\sigma = 0.24$, respectively. This gives fractional errors of 0.15 for V8k distances and 0.22 for HyperLEDA distances.

3.2.3 Blue Luminosities

Blue luminosity is a tracer of recent star formation, and in the nearby universe the distribution of binary neutron stars and black holes is expected to follow this star formation due to a high fraction of short merger timescales of around a few million years (Phinney, 1991; Belczynski, Kalogera & Bulik, 2002). Therefore for investigations into the mergers of black hole and neutron star binary systems, blue luminosity is an important parameter to include. We have included both the apparent and absolute blue magnitudes in the GWGC where available. However, unlike the CBCG catalogue we have not applied a cut

based on low blue luminosity, for two reasons. First, we do not wish to bias the GWGC towards any particular expected source. While blue light is a tracer of recent star formation, and therefore high mass compact binary formation and supernovae rates, there may be a delay in binary neutron star merger compared to the onset of star formation, as well as other unknown sources of GW bursts. Second, as shown in de Freitas Pacheco et al. (2006), the number of low blue-luminosity elliptical galaxies becomes significant in the Virgo cluster, situated at a distance of around 16.5 Mpc, and beyond.

HyperLEDA has both absolute (M_B) and apparent (m_B) blue magnitudes corrected for Galactic extinction, internal extinction and K-correction (a correction made to account for the redshift of galaxies, which are imaged in a standard filter with different rest frame wavelengths), with no errors. HyperLEDA also provides uncorrected apparent blue magnitudes with errors, which we use to apply the same fractional error to the corrected apparent blue magnitude. Tully3000 provides apparent blue magnitudes corrected for reddening, with an error of $\sigma(m_B) = 0.3$ stated in Kopparapu et al. (2008) from a private communication with Tully, while the Catalog of Neighboring Galaxies only has uncorrected apparent blue magnitudes without errors. Finally, the V8k catalogue provides absolute blue magnitudes corrected for reddening, again without errors. We take Tully3000 magnitudes over HyperLEDA magnitudes, as these are fully corrected. If a galaxy has no corrected magnitude, we take the uncorrected magnitude if available. In total 49,364 ($\sim 92.7\%$) of the galaxies in the GWGC have blue magnitude measurements.

For galaxies in the GWGC for which there is no error available for corrected apparent blue magnitude, we assign an error equal to the root of the mean of the square of the error estimates for the set of galaxies for which we do have published errors in HyperLEDA, which we find to be $\sigma(m_B) = 0.43$, which we take as the best estimate we have of the error on the magnitude for the minority of galaxies in the GWGC which have no estimated error from the original survey.

3.2.4 Angular Diameters and Position Angle

A knowledge of the size, shape and orientation of the galaxies in the GWGC is essential in order to determine whether or not the galaxy fits within the field of view of a narrow field telescope. Methods such as drift scanning and mosaic imaging could increase the sizes of galaxies we image, but it is likely that electromagnetic counterparts to the expected sources of gravitational waves are going to be faint and very short lived. Therefore a rapid image of a whole galaxy is vital. In wide-field follow-up, the overlap of the galaxy with the LIGO/Virgo pointing is used as a weight to choose the best field to image. Therefore, when planning either narrow or wide-field follow-up, the size, shape and orientation of each galaxy is needed. In addition, this information can also be used with wide-field image analysis to identify the location of the galaxy and constrain the optical transient image analysis to the regions around known galaxies, even if the galaxy is not visible in the image.

The Catalog of Neighboring Galaxies publishes major diameters (a) and the ratio of minor to major diameters (b/a), while the Tully3000 catalogue only publishes b/a and the V8k catalogue only publishes a . HyperLEDA publishes a and the ratio of major to minor diameters (a/b). HyperLEDA also provides position angle measurements. In the GWGC we include the major, minor and ratio of minor to major diameters, as well as the position angle where available.

HyperLEDA is the only catalogue to provide errors on diameters and ratios, but using the same method used in section 3.2.3, we can estimate the errors on diameters for other catalogues. In HyperLEDA we find fractional errors $\sigma(a)/a = 0.32$ for major diameters and $\sigma(r)/(r) = 0.12$ for diameter ratios where $r = b/a$. Globular clusters have diameters based on a variety of different measurements: the half mass radius, which is the distance in which half of the total mass of the cluster is contained; the core radius, which is the distance at which the surface brightness is 50% of the centre of the cluster; and the tidal

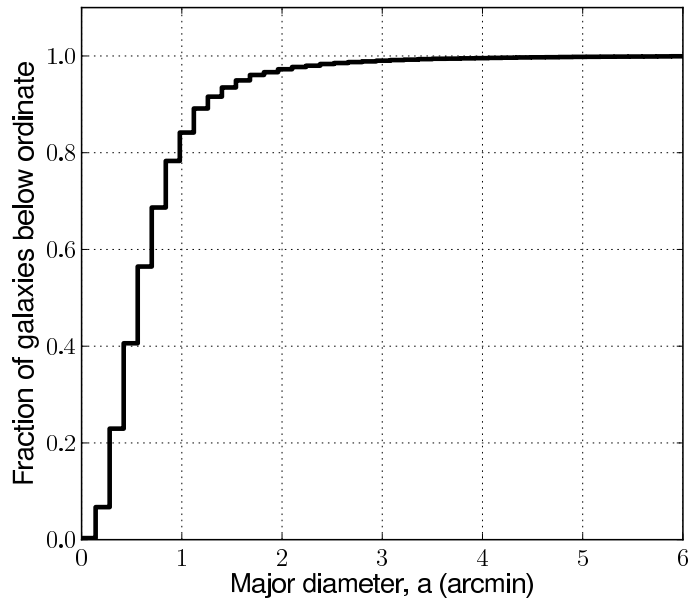


Figure 3.3: Cumulative histogram of the major diameter of the galaxies in the GWGC. Reproduced from White, Daw & Dhillon (2011).

radius, which is the distance at which the globular cluster still has gravitational influence over the constituent stars. For the GWGC we use the tidal radius in order to include as much of the globular cluster as possible, with radius measurements available for 141 of the globular clusters. In total, the GWGC contains diameters for 47,179 ($\sim 88.6\%$) galaxies and globular clusters.

3.3 Completeness

Observing faint galaxies in the local universe is a challenging task for any survey. Catalogue compilations will therefore suffer from incompleteness. The Catalog of Neighboring Galaxies, for example, is estimated to be $\sim 80\%$ complete (Karachentsev et al., 2004), but only extends to a distance of ~ 10 Mpc. Analysis of luminosity functions can give an indication of the level of incompleteness in a catalogue. For the GWGC, we calculate the luminosity function as a function of distance, $N(M_B, D)$, normalised to a spherical

volume within radius D , in terms of absolute blue magnitudes using

$$N(M_B, D, \Delta M_B) = \left(\frac{3}{4\pi D^3} \right) \sum_j l_j, \quad (3.1)$$

where $l_j = 1$ if $(M_B < M_{B,j} < M_B + \Delta M_B)$ and $l_j = 0$ otherwise. The index j is used to step through each galaxy in the catalogue, where D_j and $M_{B,j}$ are the distance and absolute magnitude of each galaxy. In order to investigate the completeness, we compare our luminosity function to the analytical Schechter galaxy luminosity function (Schechter, 1976),

$$\phi(L)dL = \phi^* \left(\frac{L}{L^*} \right)^\alpha \exp \left(\frac{-L}{L^*} \right) d \left(\frac{L}{L^*} \right), \quad (3.2)$$

where $\phi(L)dL$ is the galaxy number density within the luminosity interval L and $L+dL$, L^* is the characteristic Schechter luminosity, the normalisation factor ϕ^* is the number density at the Schechter luminosity and α is the slope of the function at the faint end of the luminosity function. The last three of these parameters must be determined empirically from galaxy surveys such as the SDSS (Blanton & Roweis, 2007; Blanton et al., 2003).

3.3.1 Comparison to other results

In terms of absolute blue magnitude eq. 3.2 becomes

$$\begin{aligned} \phi(M_B)dM_B &= 0.92\phi^* \exp \left[-10^{-0.4(M_B - M_B^*)} \right] \\ &\times [10^{-0.4(M_B - M_B^*)}]^{\alpha+1} dM_B. \end{aligned} \quad (3.3)$$

Using Table 2 in Blanton et al. (2003), and converting g -band to B -band using Table 2 in Blanton & Roweis (2007), the Schechter parameters are $(M_B^*, \phi^*, \alpha) = (-20.3, 0.0081, -0.9)$, from SDSS results extending to $z = 0.1$, which are used to plot the Schechter function in figure 3.4. It can be seen that in comparison to the CBCG catalogue, the GWGC is

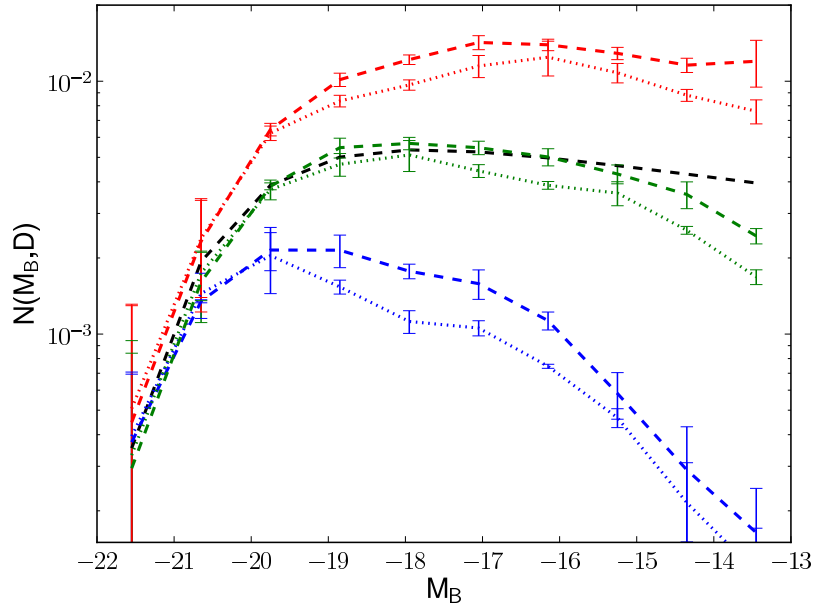


Figure 3.4: Luminosity functions for both the GWGC (dashed) and the CBCG catalogue (dotted) at various distances: 20 Mpc (red), 40 Mpc (green) and 100 Mpc (blue). The dashed black line is the distance independent Schechter function from eq. 3.3. Reproduced from White, Daw & Dhillon (2011).

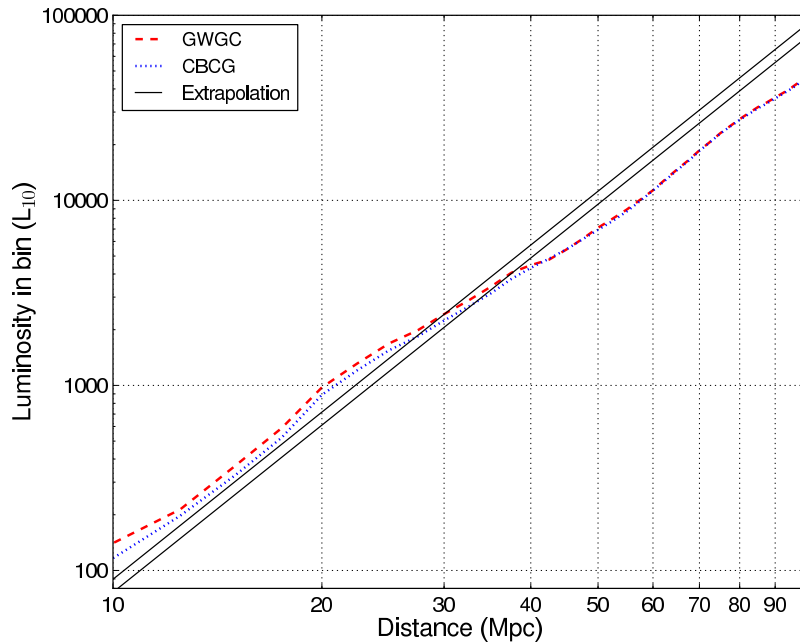


Figure 3.5: Cumulative luminosity for the GWGC (red dashed) and the CBCG catalogue (blue dotted) against distance, with extrapolation of blue luminosity density, with error (solid).

more complete at all distances. By comparing both the shape and number density of our luminosity functions to the Schechter function, we can see evidence of where incompleteness occurs. Out to 20 Mpc we see that our luminosity function has a similar shape, but higher number density, indicating that this is an overabundant region of space due to the Virgo cluster. At 40 Mpc, our luminosity function follows the Schechter luminosity function closely until we reach galaxies fainter than approximately -15th magnitude. This is an indicator that we are incomplete at faint magnitudes. At 100 Mpc, the difference between our luminosity function and the Schechter function is large, indicating a significant level of incompleteness, but we still offer improvement over the CBCG catalogue.

We show the cumulative blue luminosity (in units of L_{10} , where $L_{10} = 10^{10}L_{B,\odot}$ and $L_{B,\odot} = 2.16 \times 10^{33}$ ergs/s) as a function of distance in figure 3.5 compared to the expected distribution of blue light if we assume a blue luminosity density of $(1.98 \pm 0.16) \times 10^{-2}L_{10} \text{ Mpc}^{-3}$ as calculated by Kopparapu et al. (2008) using SDSS results out to $z = 0.1$. We also plot the CBCG catalogue for comparison. Using this method we find that the GWGC has completeness consistent with 100% out to nearly 40 Mpc, compared to just over 30 Mpc for the CBCG catalogue. Comparing the cumulative blue luminosity of the GWGC to the extrapolation of the blue luminosity density at 100 Mpc, we find that the GWGC is $\sim 60\%$ complete. However, due to the non-uniform distribution of galaxies, this may not be completely representative of the true incompleteness of the catalogue. The Local Void (Tully et al., 2008) may, in part, explain some of the incompleteness beyond 40 Mpc. However, due to the ‘‘Zone of Avoidance’’ of the Milky Way we are certain to miss some galaxies. It may be possible to overcome this somewhat with the inclusion of the 2MASS Redshift Survey (2MRS) (Huchra et al., 2012) upon public release and its addition to the HyperLEDA service. The use of SDSS also presents a problem itself, due to the directional nature of the survey. Catalogues compiled using results from this survey will always suffer from completeness problems until an all-sky survey of comparable (ideally greater) depth is undertaken.

3.4 Galaxy Catalogues for the Advanced Detector Era

3.4.1 GWGC *I*-band Magnitude Update

The GWGC as initially published was created using the assumption that blue light, which is believed to be a good tracer for star formation, is also a tracer for the most likely host galaxies for NS-NS mergers. While there is some evidence for this from Belczynski, Kalogera & Bulik (2002), the merger delay times can also produce a significant fraction of mergers long after bursts of star formation have occurred (Belczynski, Bulik & Rudak, 2002; Belczynski et al., 2006), while population synthesis models described in O’Shaughnessy, Belczynski & Kalogera (2008) allows for a large fraction (20-50%) of redder elliptical galaxy hosts. It may therefore be useful to also use the mass of the galaxy as a measure of the likelihood of host a NS-NS merger. Typically, the near-infrared and *I*-band luminosity has been used as an estimate of galaxy mass, and it has been shown that applying a colour correction can improve the accuracy of this technique (Bell & de Jong, 2001; Bell et al., 2003). In order to estimate the mass of a galaxy in the GWGC, we used HyperLEDA to provide an updated catalogue which includes *I*-band magnitudes for as many host galaxies as possible (Kanner et al., 2012). This new catalogue contains 56,969 galaxies, an increase over the original GWGC due to the inclusion of new galaxies in the HyperLEDA catalogue. Of these, 51,136 galaxies have *B*-band measurements, 34,363 have *I*-band measurements, and 31,732 galaxies have both *I*-band and *B*-band measurements.

Using the models from table 1 of Bell & de Jong (2001) it is possible to create a colour-corrected mass estimate using the *I*-band magnitude and $[B - I]$ colour as follows:

$$\log_{10}(M/L) = -0.88 + 0.60[B - I], \quad (3.4)$$

where M and L are the galactic mass and I -band luminosity, both in solar units. Therefore, given both B -band and I -band magnitudes, we can provide a rough estimate of the mass of a galaxy for use with future LIGO/Virgo follow-up programs.

Using the GWGC I -band update catalogue (hereafter known as GWGC-I), we were able to estimate how to best utilise the Swift satellite to observe triggers with the advanced detectors in order to detect possible X-ray counterparts. The X-Ray Telescope (XRT) has a field of view of 0.16 square degrees. and can reach a limiting flux of $6 \times 10^{12} \text{ erg s}^{-1} \text{ cm}^{-2}$ with an exposure time of 100 seconds. Using the properties of the GWGC-I it is possible to estimate at what point the use of a catalogue may no longer be important for telescope pointing. The GWGC-I has ~ 130 galaxies per 100 square degrees, which is a reasonable assumption for the localization of GW transients, particularly during the early part of the advanced detector era (Harry & LIGO Scientific Collaboration, 2010). As shown in figure 3.6, around 40% (10%) of galaxies in the GWGC-I contain 90% (50%) of the I -band luminosity. Figure 3.7 shows how the number of fields required to observe enough galaxies to image 90% and 50% of the I -band luminosity varies with distance, assuming a complete catalogue (given that the GWGC is $\sim 60\%$ complete) and that the number of galaxies scales with r^3 . From this we can see that at a distance of 100 Mpc requires fewer pointing's by an order of magnitude to image galaxies individually than to image the entire localised region (assuming 0.12 square degrees to account for overlap of fields). At a distance of 200 Mpc (the NS-NS distance range for the final configuration of the advanced detectors) the number of fields required to image each galaxy individually and the entire region is approximately equal. This shows that a galaxy catalogue is still a useful tool in the advanced detector era.

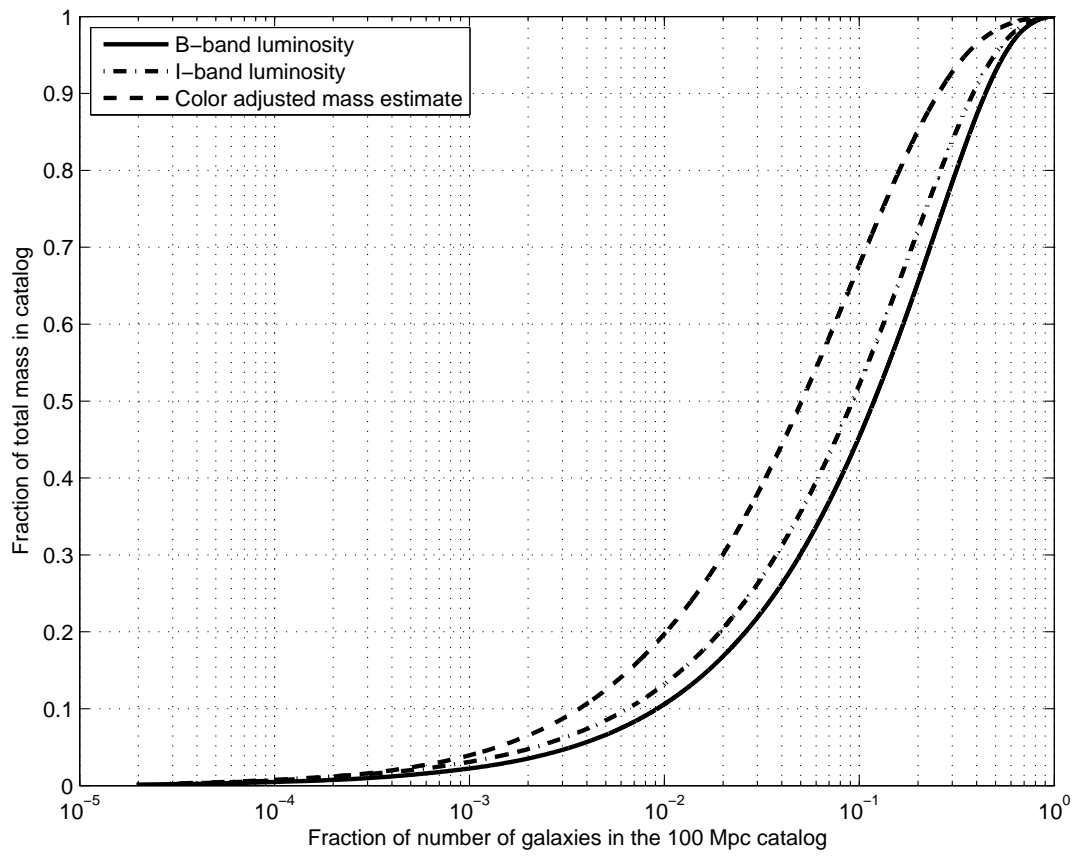


Figure 3.6: Plot of the fraction of the total number of galaxies that must be selected in order to obtain a target fraction of the total luminosity or mass in the catalogue. Reproduced from Kanner et al. (2012).

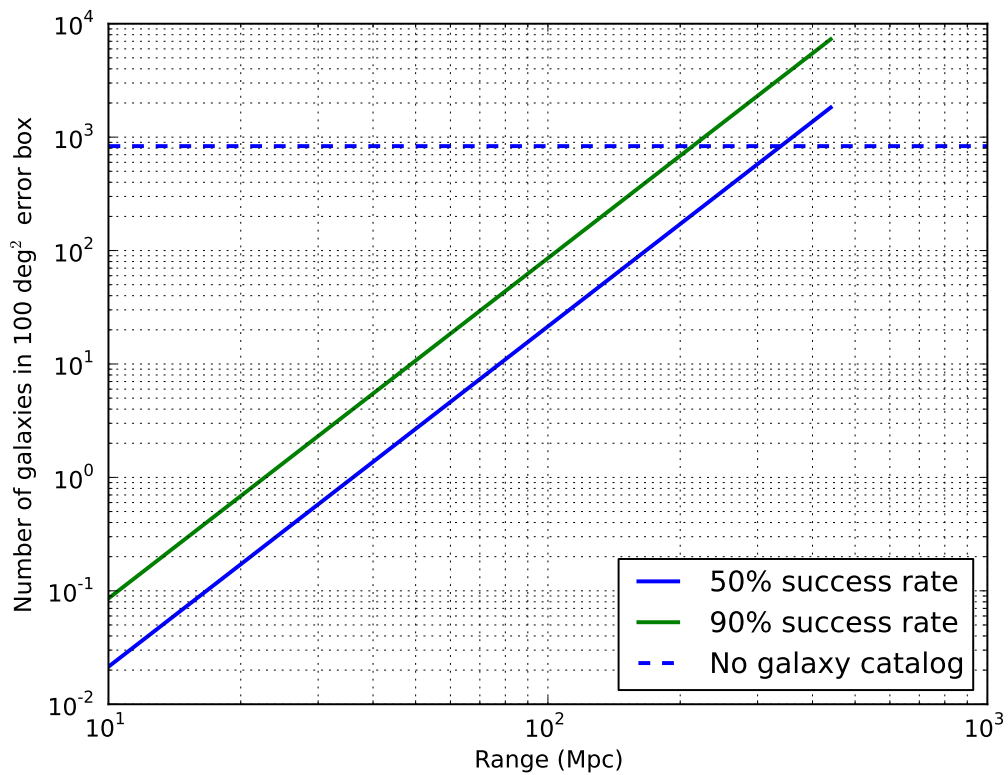


Figure 3.7: Plot of the number of galaxies within 100 square degrees as a function of distance. The GWGC contains 53,000 galaxies within 100 Mpc of earth. The figure assumes that the number of galaxies within a horizon distance r scales as r^3 , and that the catalogue is 60% complete. Reproduced from Kanner et al. (2012).

3.4.2 $H\alpha$ and HI Surveys to Improve Catalogue Completeness

To improve the chances of success for EM follow-up efforts in the advanced detector era a more complete galaxy catalogue is required. Metzger, Kaplan & Berger (2013) recently attempted to quantify how future sky surveys may impact on catalogue completeness, using the assumption that NS-NS mergers are the progenitors of short GRBs, which I summarise in this section. The authors attempt to estimate completeness of future catalogues within 200 Mpc from planned or feasible HI and $H\alpha$ surveys. Leibler & Berger (2010) show that the likelihood of a galaxy hosting a SGRB may trace a combination of both star formation rate (SFR) and stellar mass (M_*). This conclusion is contrary to the findings of Phinney (1991) discussed earlier, in which the SFR alone, and therefore blue light, was considered the ideal tracer. Metzger, Kaplan & Berger (2013) investigate the completeness of a narrowband $H\alpha$ imaging survey and an HI emission line survey to both SFR and M_* at survey depths of $F_{H\alpha} > 2 \times 10^{-15}$ erg s $^{-1}$ cm $^{-2}$ (achievable on metre-class telescopes such as PTF) and $F_{HI} > 0.7$ mJy (the limiting flux for the planned survey WALLABY, the Widefield ASKAP L -band Legacy All-Sky Blind survey). Figures 3.8 and 3.9 show the completeness of the two surveys to SFR and M_* as a function of survey depth.

Using galaxies and their properties from SDSS Data Release 7 (see Metzger, Kaplan & Berger (2013) for a full description of the methods used), the authors estimate a minimum completeness for $H\alpha$ of $f_{SFR}^{H\alpha} \gtrsim 75\%$ and $f_{M_*}^{H\alpha} \gtrsim 30\%$. For an HI survey, the minimum completeness increases to $f_{SFR}^{HI} \gtrsim 90\%$ and $f_{M_*}^{HI} \gtrsim 45\%$. However, these results alone may not give an accurate representation of the true completeness of a survey to typical host galaxies of SGRBs. For this reason, the authors also estimate the completeness of the surveys using galaxies in SDSS with similar masses and SFRs of 11 known SGRB hosts from Leibler & Berger (2010) and Berger (2009). This results in a realistic minimum completeness for the two surveys of $f_{SGRB}^{H\alpha} \gtrsim 50\%$ and $f_{SGRB}^{HI} \gtrsim 45\%$.

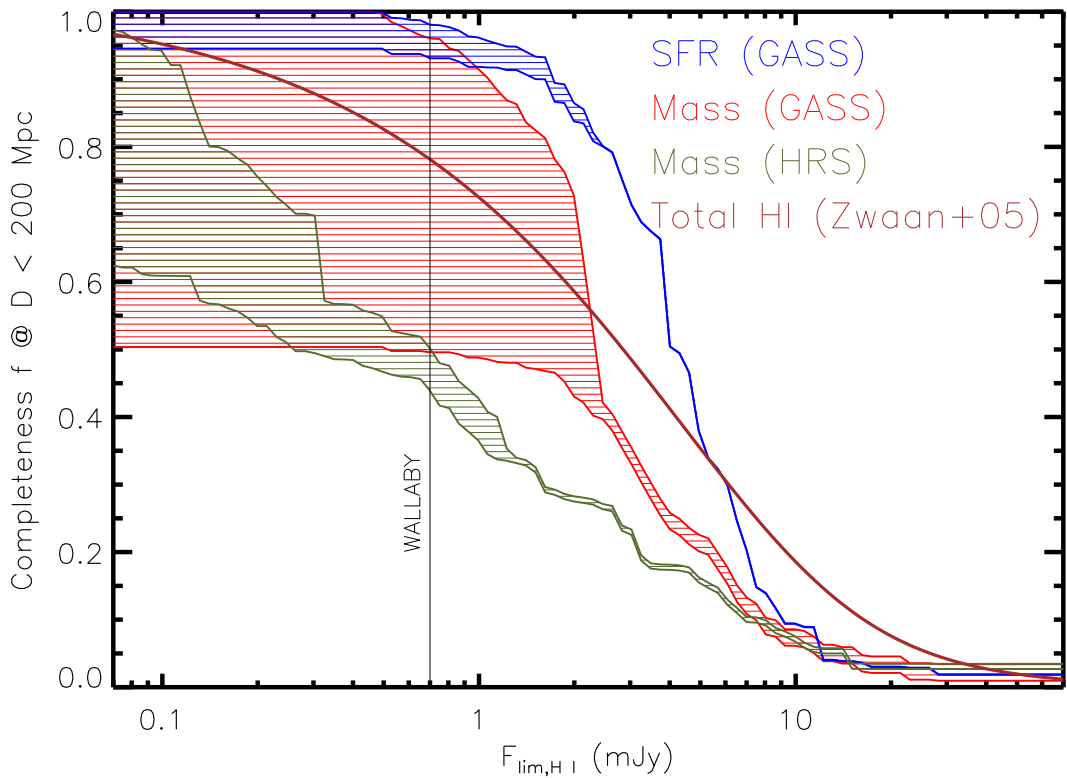


Figure 3.8: Estimated completeness of an all-sky HI survey with respect to total stellar mass (red) and total star formation (blue) as a function of survey depth ($F_{\text{lim,HI}}$). Also shown is the mass completeness calculated using HI masses from the Herschel Reference Survey (HRS; green) and the completeness with respect to total HI mass (brown) calculated using the local HI luminosity function from Zwaan et al. (2005). The hatched regions indicate the range of uncertainty in completeness at low flux due to HI upper limits. See Metzger, Kaplan & Berger (2013) for details of calculation.

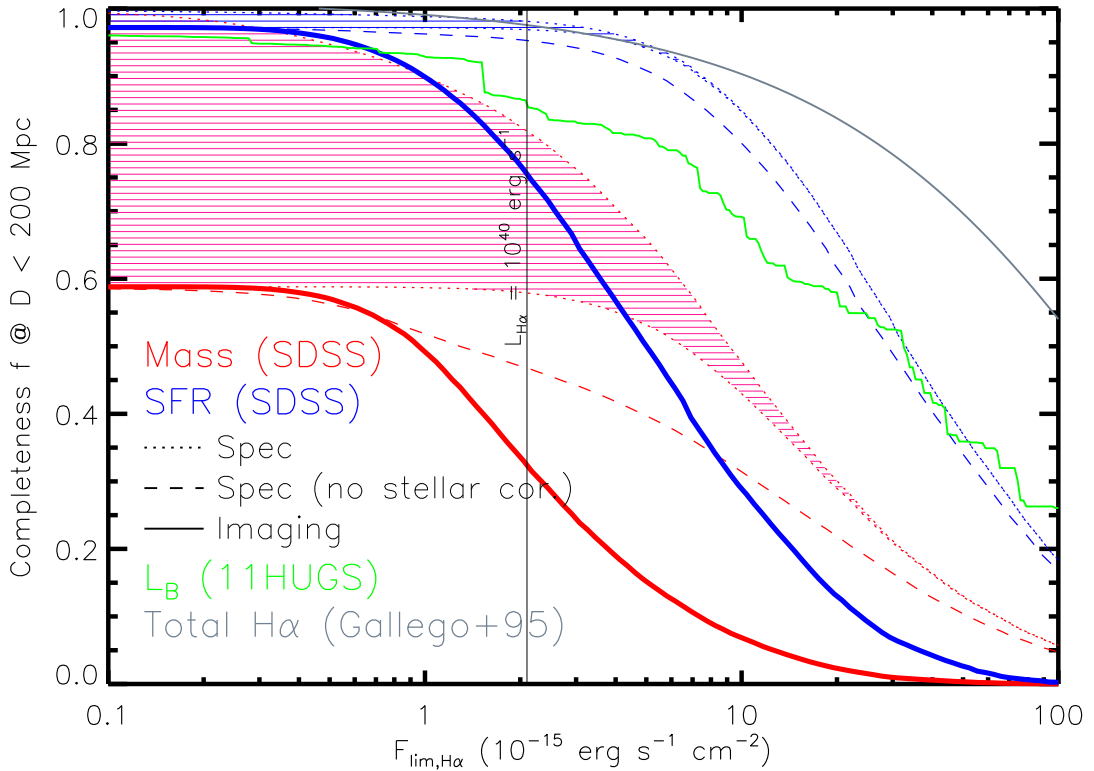


Figure 3.9: Estimated completeness of an all-sky, narrow-band $H\alpha$ survey with respect to total stellar mass (red) and total star formation (blue) as a function of survey depth, $F_{\text{lim},H\alpha}$. Dotted lines show the completeness of an idealised spectroscopic survey which measures the entire $H\alpha$ luminosity of the galaxy (infinite aperture) and corrects the $H\alpha$ flux for stellar absorption; the cross-hatched region represents the uncertainties due to $H\alpha$ upper limits. Dashed lines show how the minimum completeness decreases when one does not correct $H\alpha$ fluxes for the underlying stellar Balmer continuum, as appropriate for narrow-band imaging. Solid lines show the minimum completeness when the $H\alpha$ fluxes are also not corrected for the finite angular size of the galaxy (assuming a 1.5 arcsec radius aperture). These last two cases likely bracket the completeness provided by a purely imaging survey. Also shown for comparison is completeness with respect to B -band luminosity (green) of the local (< 11 Mpc) 11HUGS survey (Kennicutt et al., 2008) and with respect to total $H\alpha$ luminosity (gray; using the Gallego et al. (1995) luminosity function). See Metzger, Kaplan & Berger (2013) for further details.

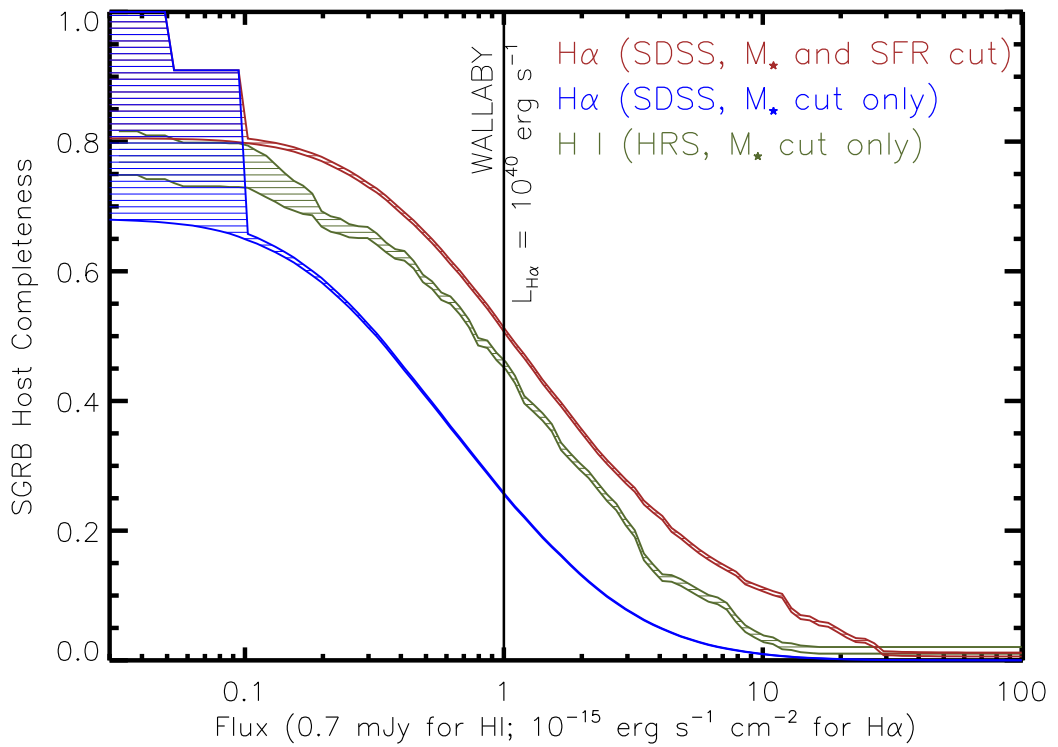


Figure 3.10: Completeness of H α and HI surveys with respect to galaxies with properties (SFR and M_*) similar to those of the host galaxies of short GRBs, normalised to the sensitivity of our fiducial H α imaging survey and to that of WALLABY. In the case of H α , the SDSS galaxy sample is used; results are shown both using a subsample of galaxies selected based on similar stellar masses and SFRs to the short GRB hosts (brown), as well as subsamples chosen based just on similar stellar masses (blue). In the case of HI, the HRS sample is used and results are shown just for the subsample with similar stellar masses (green); since most SGRB hosts are star forming, the completeness achievable by HI is probably underestimated by this figure. Reproduced from Metzger, Kaplan & Berger (2013).

Increasing the survey depth will obviously increase the completeness, as shown in figure 3.10, but only to a maximum of around 80% for $H\alpha$, as 2 of the 11 SGRB host galaxies are elliptical galaxies with only upper limits on the star formation rate. The authors also note that broad-band photometric surveys could complement the surveys described above, as optical surveys are less biased towards star formation and will pick up a larger proportion of stellar mass, which will be investigated in future work.

3.5 Conclusions

In order to increase the likelihood of detecting electromagnetic counterparts to gravitational wave sources, a complete catalogue of nearby galaxies is vital. Using a combination of local and extended galaxy catalogues from the literature, we have compiled a new catalogue reaching out to 100 Mpc. For each galaxy we provide the most accurate distances and positions available, along with diameters, position angles and blue magnitudes where possible. We also provide errors on distances, diameters and magnitudes, either from the literature or estimated as described in the relevant sections. Comparing our galaxy catalogue to the expected distribution of blue light based on SDSS data shows that the catalogue is almost complete out to a distance of ~ 40 Mpc, but suffers from systematic incompleteness beyond this distance. This will only be truly solved with the inclusion of a deep, all-sky galaxy survey. The catalogue is also designed to be flexible, non degenerate and easily updated upon the release of new observations. The catalogue, known as the GWGC (White, Daw & Dhillon, 2011), has already been of use (e.g. Abadie et al., 2012e; Nuttall et al., 2012; Evans et al., 2012; Branchesi, LIGO Scientific Collaboration & Virgo Collaboration, 2012; Adrián-Martínez et al., 2013b) with the first major update to include I -band measurements of galaxies, allowing an improved estimate of the mass of the galaxy to be made, looking ahead towards the advanced detector era (Kanner et al., 2012). This chapter also summarises work done to investigate the use of all-sky

H α and HI surveys to improve the completeness of catalogues for the advanced detector era. Metzger, Kaplan & Berger (2013) find that, for surveys described in section 3.4.2, an H α catalogue could find 75% of the star formation, 30% of the stellar mass and around 50% of galaxies similar to known hosts of SGRBs, while an HI catalogue could find 90% of the star formation, 45% of the stellar mass and around 45% of galaxies similar to known hosts of SGRBs.

Chapter 4

Optical Image Analysis of GW Triggers

This chapter describes the data reduction pipelines used for the analysis of images taken with the Liverpool Telescope and the ROTSE network, as part of the 2009-2010 EM follow-up campaign described in chapter 2. This chapter is based on work published in Aasi et al. (2014). Sections 4.2.3 and 4.3.3 are also based on work presented in White, LIGO Scientific Collaboration & Virgo Collaboration (2012), while section 4.3 is based on work presented in Nuttall et al. (2012).

4.1 Image Analysis Methods for the LoocUp Project

During the 2009-2010 joint science run of LIGO and Virgo a total of 1,806 follow-up images were taken using the telescopes listed in section 2.2. As shown in table 2.1 these cover a wide range of fields-of-view and limiting magnitudes. Therefore it was decided that small groups would work together on separate data sets, utilising current analysis pipelines where possible, or creating suitable analysis methods where needed. A full description of the analysis methods for individual telescopes can be found in Aasi et al. (2014). These analysis methods can be broadly split into two groups. The catalogue-based search tracks the brightness of each object found in a series of images and looks

for a change in magnitude above a given threshold. Cuts are typically made to remove objects coincident with known variable stars and asteroids. This technique was used on images taken with the TAROT, QUEST, Zadko and Pi of the Sky telescopes.

The alternative method utilised image subtraction, again with some variation to account for the differences in telescopes. The PTF, ROTSE and Liverpool telescopes all used image subtraction in their analysis pipelines, based on the methods originally described by Alard & Lupton (1998), subsequently improved in Alard (2000). Image subtraction algorithms attempt to find a convolution kernel which convolves one image to match the PSF and flux of another, which can then be subtracted. The convolution kernels used in these analyses are composed of 2-D Gaussians multiplied by polynomials. In Alard & Lupton (1998) the kernels are calculated for the images as a whole, while Alard (2000) attempted to account for PSF variation across an image by calculating kernels for image subsections. Once an image has been convolved, image subtraction can be performed, producing a difference, or residual, image containing objects variable between the two original images. This has the advantage over the catalogue based approach in that transients in crowded fields or in bright galaxies can be more easily detected. The downside to image subtraction is that the alignment and convolution is not always perfect, and can produce additional artefacts which require special attention, some of which are discussed in detail in sections 4.2.2 and 4.3.2.

4.2 Liverpool Telescope Analysis

4.2.1 Follow-up Images Taken with the Liverpool Telescope

The Liverpool Telescope is a 2 m robotic telescope with a 4.6' Field-of-view (FoV) situated at the Observatorio del Roque de los Muchachos, La Palma, Spain. Images were taken with the RATCam instrument using the SDSS r' -band filter. The observing plan

for the Liverpool Telescope was to take 11 images in one hour as soon as possible after the GW trigger each with, exposure times of 300 seconds duration each in addition to one-off overheads of 60 s for acquisition, 45 s for autoguiding, 5 s for filter changing, and 110 s for CCD readout time. This allowed us to reach a limiting magnitude of ~ 21 . For the work described here we only imaged one trigger during the 2009-2010 LIGO/Virgo science run, designated G23004. The target considered the most likely candidate that the Liverpool Telescope could image, as described in 2.2, was the galaxy NGC1507 (RA: $61^\circ 06' 41.4''$, Dec: $-2^\circ 11' 46.2''$). For this trigger we took 11 images starting at UTC 01:04:51 on 2010 Oct 4. We also obtained a further 11 images with RATCam of the same galaxy starting at UTC23:18:16 on 2010 Nov 01. In addition, we were able to obtain images from a secondary finder scope on the LT with a 1 degree FoV called SkyCamZ (Mawson, Steele & Smith, 2013), centred on the same field which can reach $\sim 18^{\text{th}}$ magnitude with 10 second exposures every 60 seconds during the time of observation. This produced a total of 22 narrow field images with a further 172 images from the SkyCamZ telescope to be analysed. Finally, 3 RATCam and 17 SkyCamZ images were taken on 2012 Mar 08 to be used as reference images.

As with other analysis efforts within the LoocUp group, it was first necessary to remove images that were unusable. In the case of the LT this included one image on the first night, due to a bright satellite passing through the field. It was also necessary to remove one SkyCamZ image from the second night as the image was taken whilst slewing the telescope. In addition, it is also necessary to remove one additional image from the second night in order to have a suitable number of images to produce the co-added images detailed in section 4.2.2, as the number of images taken results in a single remainder image with no co-addition possible.

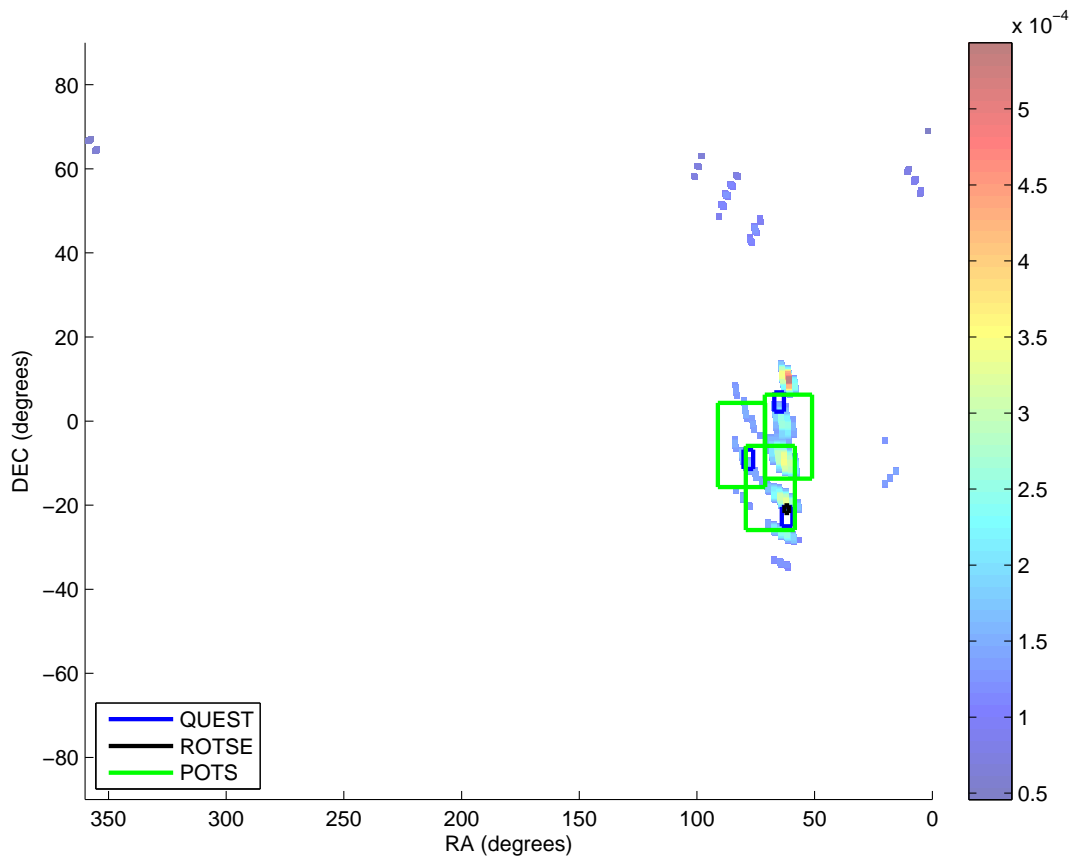


Figure 4.1: Skymap for the trigger G23004, with fields imaged by specific telescopes highlighted.

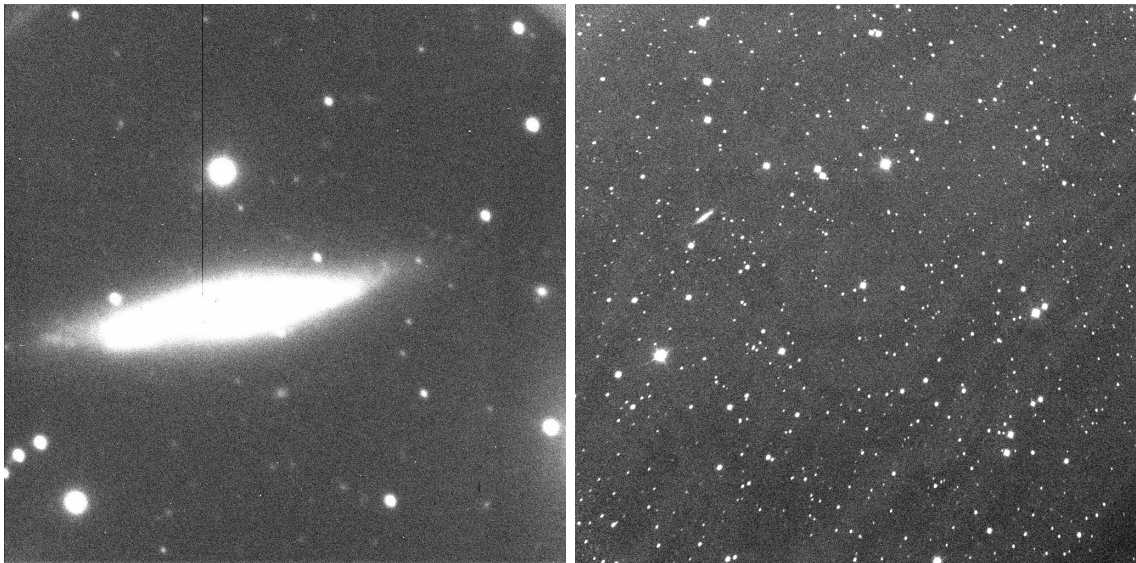


Figure 4.2: Typical images provided by the RATCam instrument (left) and the SkyCamZ telescope (right).

4.2.2 The Liverpool Telescope Analysis Pipeline

The LT pipeline for this analysis consists of a series of python scripts written by myself, which passes images and parameters to standard programs which align, combine and image-subtract the frames. Before any analysis can be done, we must first create the reference images used for subtraction. To do this for RATCam we combine the images taken in 2012. This removes any uninteresting transient artefacts in single images, such as cosmic rays or passing satellites. This is performed using SWarp (Bertin et al., 2002), which takes the median value of the aligned pixels in the images to be combined as the value of the pixel in the output reference image. SWarp requires that the input images are sufficiently aligned so that simple pixel-by-pixel combining can be performed. Due to the design of the LT, RATCam images of the same region on the same night are already aligned via a CCD rotator. However, due to the mounting of the SkyCamZ camera on the main body of the LT these images are slightly mis-aligned between exposures as the telescope tracks the target field across the sky. Alignment is achieved by resampling images to match the pixel layout of a target image, for which we use WCSRemap¹. Once this has been completed, it is simple to combine the images in the same way as with the RATCam images. In addition to the reference images taken in 2012, we chose to combine the SkyCamZ images from our initial observations in 2010 into sets of 5 images using SWarp. Again, this helped remove any uninteresting transient artefacts from the images, and also provided SkyCamZ images with a similar cadence to the RATCam images.

SkyCamZ Image Calibration

Since the SkyCamZ instrument uses a clear, white light filter the images must be calibrated using the USNO-B catalogue of stars in order to obtain the zero point (ZP) required to calculate corrected magnitudes from these images, the results of which are shown in figure 4.3. To do this, we compared the USNO-B *R*-band magnitudes of stars

¹<http://www.astro.washington.edu/users/becker/wcsremap.html>

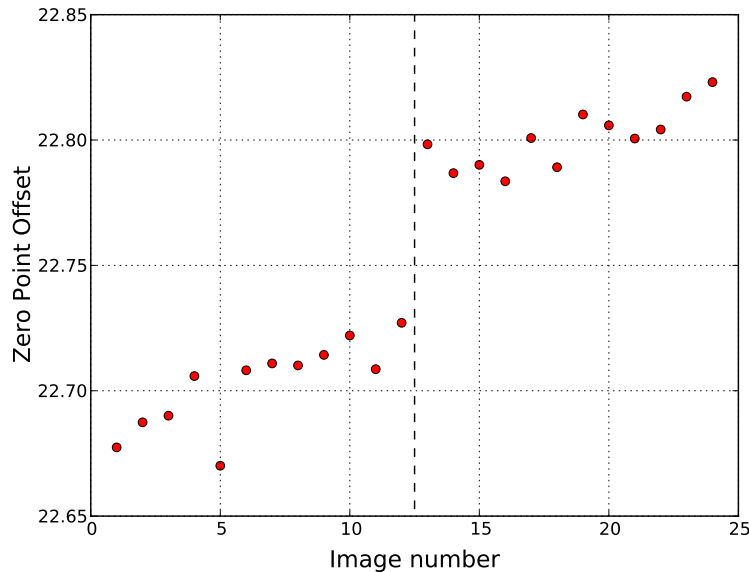


Figure 4.3: Plot showing the slight variation in the calibrated zero point offset for combined SkyCamZ images. The dashed line highlights the difference between the two sets of images; one set from the first night of observations and the second set taken a month later. This shift is due to differences in atmospheric extinction between observing nights.

found using SExtractor (Bertin & Arnouts, 1996) in the combined SkyCamZ images with a zero point of 0.0. The median difference between the USNO-B magnitudes and the SExtractor magnitudes is the zero point offset for that image.

The zero point² for the r' -band filter for the RATCam instrument is stated as $ZP_{\text{RATCam}} = 24.5$. However, SExtractor does not automatically take into account the gain, g , and exposure times, t_{exp} , of images when calculating the magnitudes of objects when using the zero point provided. Therefore, we must calculate the zero point to be used with RATCam images that SExtractor is expecting, by taking these parameters into account. To calculate this, we convert between ZP_{RATCam} and the required SExtractor zero point, ZP_{sex} using the following:

$$ZP_{\text{sex}} = ZP_{\text{RATCam}} + 2.5 \log_{10}(t_{\text{exp}}) - 2.5 \log_{10}(g) \quad (4.1)$$

²<http://telescope.livjm.ac.uk/Info/TelInst/Inst/RATCam/>

For our RATCam images, we have exposure times of 300 seconds and a gain of 2.2, which gives us a value of ZP_{sex} of 29.84. Since we have calibrated the SkyCamZ images using a standard catalogue, the zero points calculated for these images already take into account the exposure times and gains of the images.

Alignment and Subtraction

Once the image zero points have been calibrated and the 2012 reference images created it is possible to perform image alignment and subtraction. Each individual image to be subtracted is aligned using WCSRemap to match the orientation of the reference image. The reference image is then subtracted from the analysis image using the High Order Transform of PSF and Template Subtraction (HOTPANTS)³ image subtraction package. SExtractor is then used to detect potential candidates in each individual field. An object is considered a candidate if the object contains a minimum of 4 pixels 4σ above the background noise level of the image, as selected in the configuration of SExtractor for this analysis. This limit was chosen as it represented the best balance between achieving the lowest detection threshold without saturating the pipeline with uninteresting objects from background noise due to cosmic rays or residual effects from the image subtraction routine, and is analogous to a FWHM cut. This allowed us to achieve a limiting magnitude of around $r' = 20$ for the RATCam images and $R = 16.5$ for the SkyCamZ images. One issue with the SkyCamZ analysis is that the reference image used for subtraction is not centred perfectly with the images taken in coincidence with the trigger, due to the mounting of SkyCamZ on the LT. This reduces the field size available for analysis by $\sim 50\%$, and also has consequences for our efficiency study described in section 4.2.3.

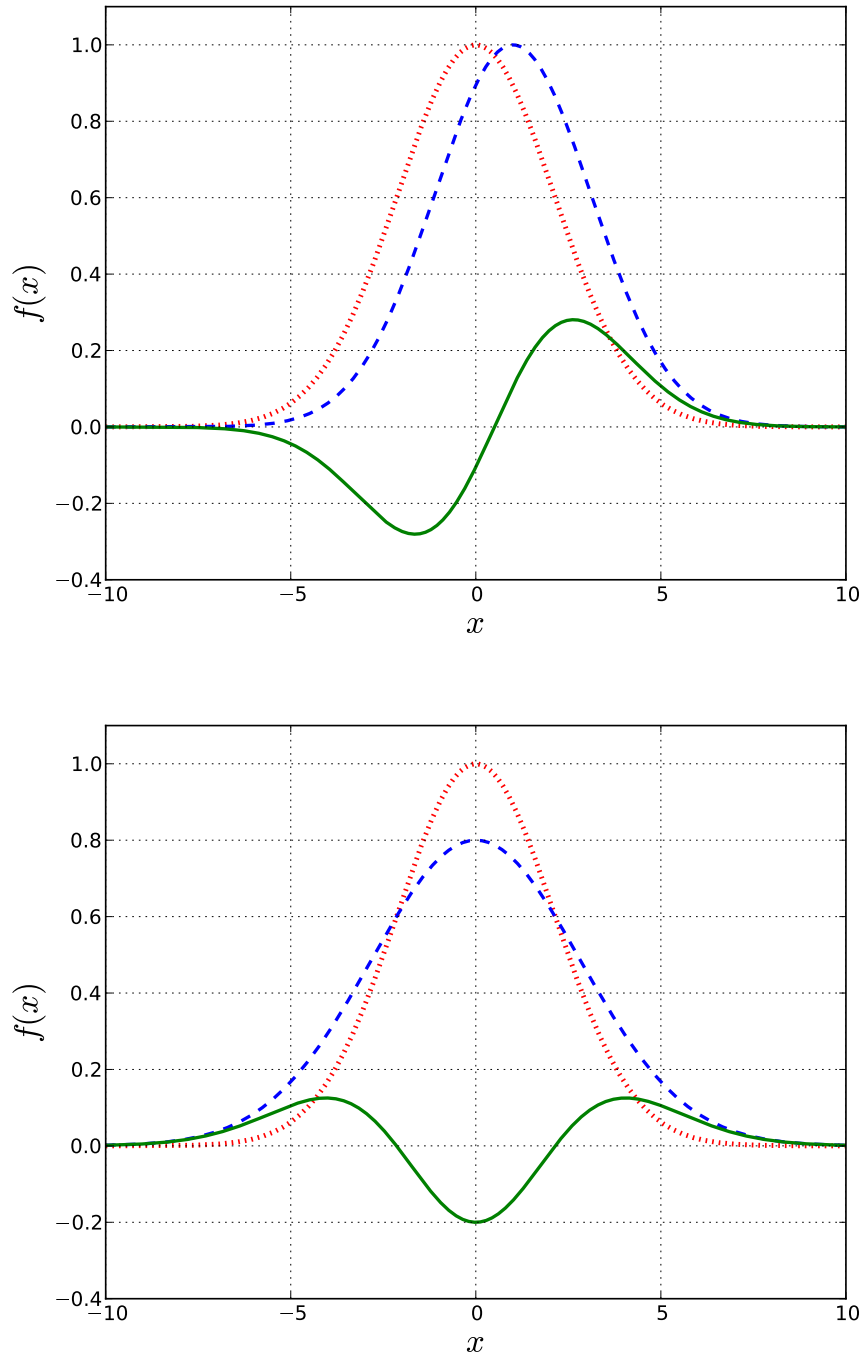


Figure 4.4: Simplified examples of bad subtraction using simple 1-D Gaussians. In both images, the red-dotted Gaussian has a height, $h = 1$ and width, $\sigma = 3$. In the top image the blue-dashed Gaussian has the same shape, but is shifted to the right by 1 (poor alignment). In the bottom the blue-dashed Gaussian has $h = 0.9$ and $\sigma = 4$ (poor convolution). In both cases the red-dotted Gaussian is subtracted from the blue-dashed Gaussian, producing the residual green-solid curve in both images. This is an oversimplified model designed to explain the basic processes which can produce false candidates.

Candidate Rejection

The output from SExtractor for each individual image is then combined to provide a list of every unique transient candidate from the entire sequence of subtracted images. Each unique candidate lists the magnitude, magnitude error and full-width at half-maximum (FWHM) of the object in each image. Using this information data, a series of cuts were made to highlight any candidates that are interesting to our analysis. First, candidates found within 20 pixels of the edge of either the original or reference image were discarded, as the image subtraction process produces artefacts in these regions. For RATCam images we also removed candidates within 20 pixels of a strip of damaged pixels for the same reason. Next we removed candidates due to bad image subtraction. These are primarily caused by poor alignment or convolution of the images prior to subtraction. This produces a residual “negative” flux in the subtracted image alongside the detected positive flux above threshold, as shown in figure 4.4. If the total amount of negative flux is greater than the threshold for candidate detection detailed above (4 pixels greater than 4 sigma below the median) then the candidate in that particular image was ignored (but the candidate may still be a valid candidate in other images). The next cut removes candidates not seen in at least half of the images available on the first night, to ensure candidates were visible long enough to be confident that they are not simply artefacts. We also rejected candidates that appeared close to known variable stars in the General Catalogue of Variable Stars (GCVS; Samus et al., 2009) and minor planets from the Minor Planet Checker⁴. Finally, a candidate must decrease in brightness (corrected for atmospheric extinction⁵) greater than 5 sigma of the median error on the magnitude measurements from SExtractor, from the first night to the second night 29 days later. This allows us to be confident that a candidate is a transient, and is not varying due to

³ <http://www.astro.washington.edu/users/becker/hotpants.html>

⁴ <http://scully.cfa.harvard.edu/cgi-bin/checkmp.cgi>

⁵ Calculated using the airmass stored in the FITS header of each image and the extinction coefficient taken from http://www.ast.cam.ac.uk/~dwe/SRF/camc_extinction.html on the same (or nearest) night data is available.

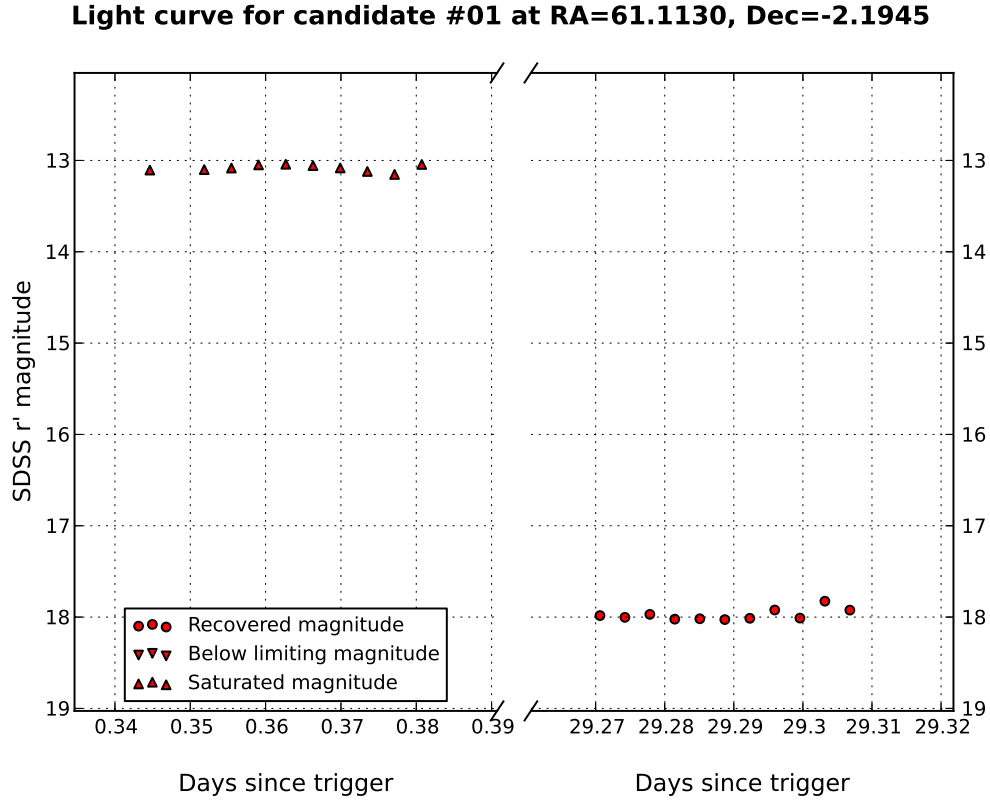
measurement error.

Any objects that remained after these cuts were considered likely candidates, and looked at in more detail. This was initially done by plotting the light curves of each object across both nights and inspecting images of the candidates in both the original and subtracted images. This allowed us to gauge whether any transients warranted further investigation. An example of the output from the pipeline using an injected transient is shown in figure 4.5.

4.2.3 Efficiency of the Liverpool Telescope Pipeline

In order to be confident in the results of our analyses, it is useful to test the efficiency of the pipelines to the EM transients expected as counterparts. The most promising sources of GW signals are the mergers of compact objects (neutron stars and black holes) and core collapse supernovae. The EM sources believed to be associated with these events, as discussed in chapter 2 are LGRBs, SGRBs and kilonova decay. For the injections, we used the observed optical afterglows of on-axis GRBs and the decay model expected for kilonovae (see figure 4.6), taken from Kann et al. (2010) for LGRBs, Kann et al. (2011) for SGRBs and Metzger et al. (2010) for the kilonova Model. The transient flux depends on both the distance to the source, and the difference in time between the original event and the time the image was taken.

As seen in figure 4.6, the LGRB and SGRB afterglows follow similar decays, which can be described by a power law of the form $L \propto t^{-\gamma}$, where $\gamma \approx 1$. To calculate the magnitude of an object that follows these models at specified distances we use the magnitude of these afterglows located at $z = 1$ one day after the GRB, which gives us magnitudes of 20 ± 4 and 27 ± 4 for LGRB and SGRB afterglows, respectively. For the



Images of candidate #01 at RA=61.1130, Dec=-2.1945

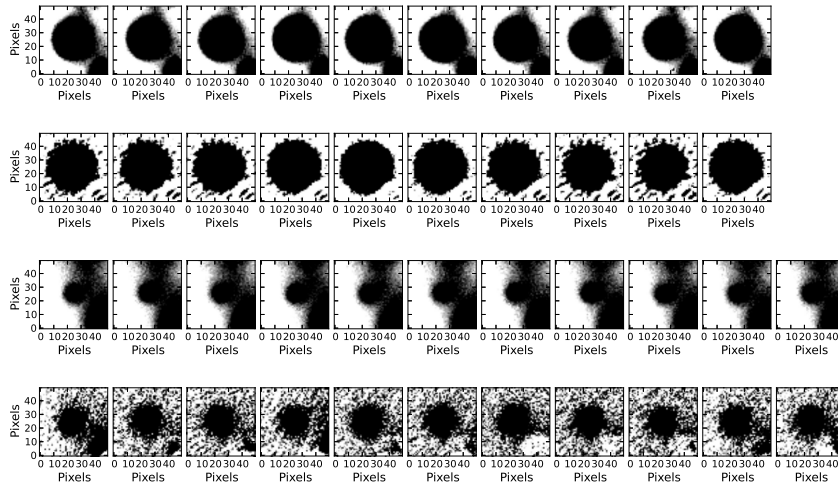


Figure 4.5: An example of candidate lightcurve and images produced by the pipeline for the Liverpool Telescope using a bright injected LGRB afterglow at a distance of ~ 50 Mpc.

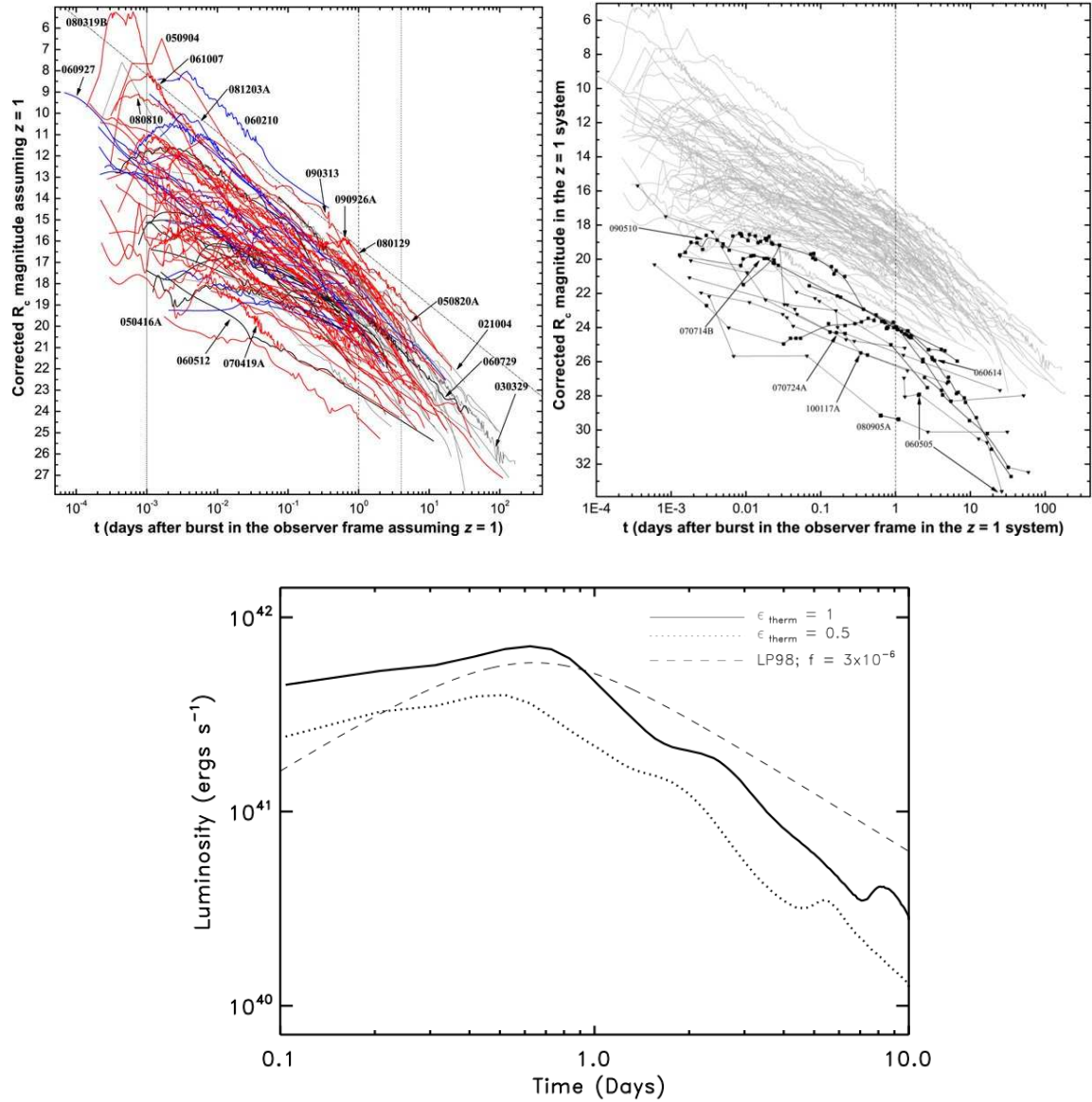


Figure 4.6: Examples of the light curves used as models for transient injections. Top left is an example of measured LGRB light curves, taken from figure 4 of Kann et al. (2010). Top right is an example of SGRB light curves taken from figure 5 of Kann et al. (2011). Bottom is the bolometric radioactive afterglow model from figure 4 of Metzger et al. (2010).

kilonova model, we calculate the luminosity with the relationships (Aasi et al., 2014):

$$L = 10^{42} \times t^{0.43} \text{ ergs s}^{-1} \quad (t < 0.7 \text{ days})$$

$$L = 5.1 \times 10^{41} \times t^{-1.29} \text{ ergs s}^{-1} \quad (t > 0.7 \text{ days}).$$

In order to estimate the efficiency of the pipeline, we injected a number of transients into our images, which were then analysed using the same pipeline described in section 4.2.2. Ideally, we would use pre-existing stars in the images to act as templates to be injected into other regions in the images (as described in section 4.3.3), but due to the sparse number of suitable stars in the LT images, this was not possible. However, due to the high quality images obtained by the LT, this is not a major problem, and can be rectified by injecting a suitable point spread function (PSF) which matches our images. For the Liverpool Telescope images a softened exponential, known as a Moffat profile (Moffat, 1969), was chosen as the most suitable PSF for our images:

$$I(r) = I_0 \left[1 + \left(\frac{r}{\alpha} \right)^2 \right]^{-\beta} \quad (4.2)$$

where

$$\alpha = \frac{\text{FWHM}}{2\sqrt{2^{\frac{1}{\beta}} - 1}}, \quad (4.3)$$

and $I(r)$ is the intensity of the function at a radius, r , from the center of the profile, I_0 is the value of the function at $r = 0$, and β determines the overall shape of the PSF. The value for β was measured to be ~ 3 and ~ 2 for the RATCam and SkyCamZ images respectively using the standard Image Reduction and Analysis Facility (IRAF). The Moffat profile is similar to a 2-dimensional Gaussian, but with broader wings. Examples of comparisons between Moffat profiles, 2-dimensional Gaussians and a bright star found in an LT image are shown in figure 4.7.

Using the light curve models described earlier, Moffat profiles were injected into

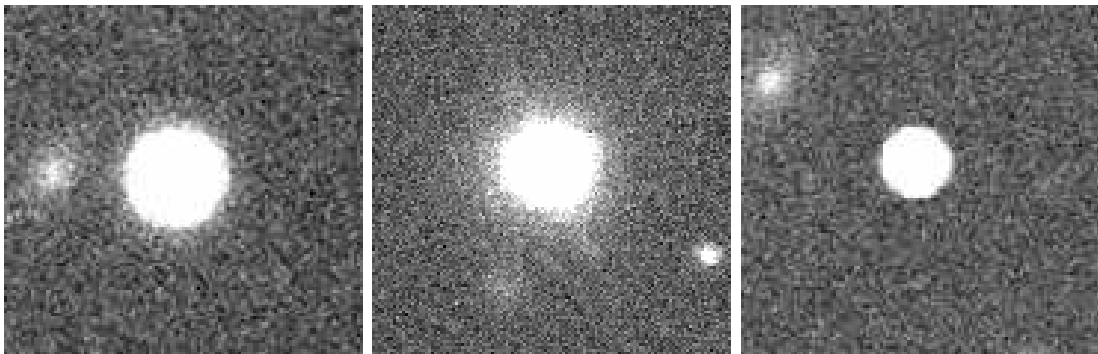
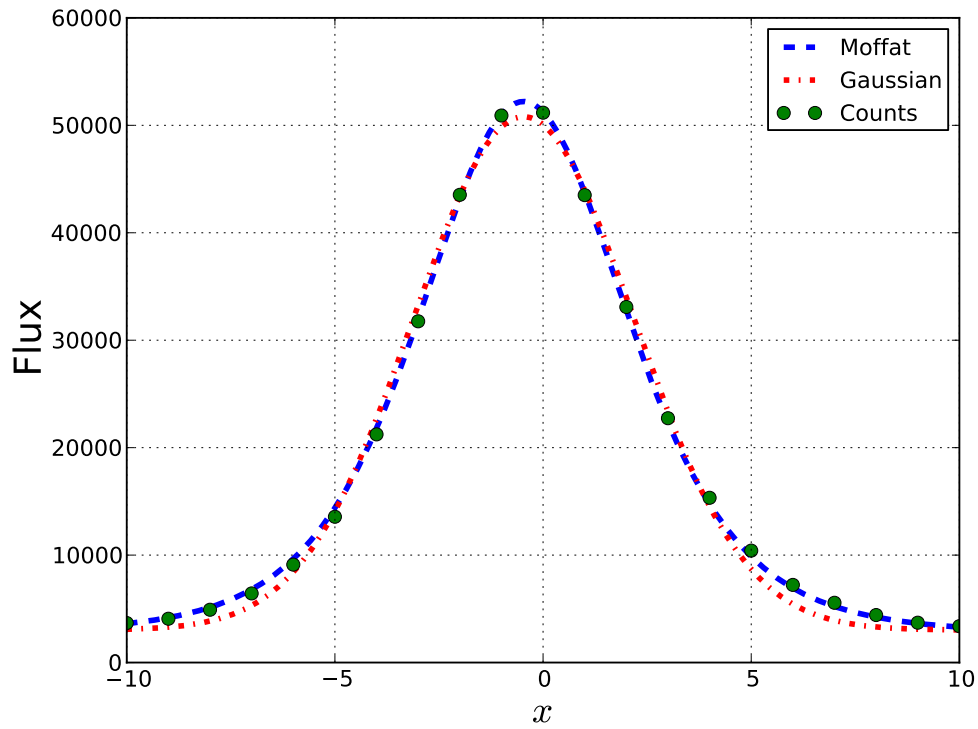


Figure 4.7: Top: Comparison of 1-D Moffat (blue-dashed) and Gaussian (red-dotted) profile fits to a star in a Liverpool Telescope image (green circles). Bottom: Comparison of injections made with 2-D Moffat functions (left), 2-D Gaussian (right) compared to a star in a Liverpool Telescope image of the same magnitude (center).

the images at distances ranging from 0.1 Mpc out to either 1 Gpc, or the distance at which the magnitude of the transient is equivalent to the limiting magnitude of our images described in section 4.2.2, found to be around $r' = 20$ for the RATCam images and $R = 16.5$ for the SkyCamZ images. The image sets produced by the injection algorithm were then analysed using the LT pipeline, and objects recovered compared to the list of injections in each set of images. This allowed us to produce efficiency curves for our images for all light curve models, as shown in figures 4.8 and 4.9. Since the SkyCamZ images used for analysis were not centred on the same region as the reference image we plot both the efficiency of all injections into the original images, regardless of coverage by the reference image, and the efficiency of injections that are in the region of sky covered by the reference image to highlight the importance of obtaining well aligned images where possible. For both RATCam and SkyCamZ images we are able to recover $\sim 90\%$ of injections that are covered by the reference images out to either the limiting magnitude (shown by a sudden drop in efficiency) or the maximum distance injections were made (1 Gpc). Unlike the ROTSE pipeline described in section 4.3.2, the LT pipeline does not mask saturated objects before subtraction, so it is possible to detect injections at close distances. The missing 10% rejected primarily due to the candidate being too close to the image edge or a region of poor subtraction. The dip in efficiency at around 20 Mpc in the bottom plot of figure 4.8 is due to several injections being placed either close to the bad pixel strip or each other. The decrease in efficiency for very nearby LGRB injections is also due to the overlap of injections. The extreme brightness of nearby LGRB injections results in objects with hundreds of saturated pixels. When two or more injections close by overlap, SExtractor can pick out only one object instead of the two or more that were injected due to the blending of the objects.

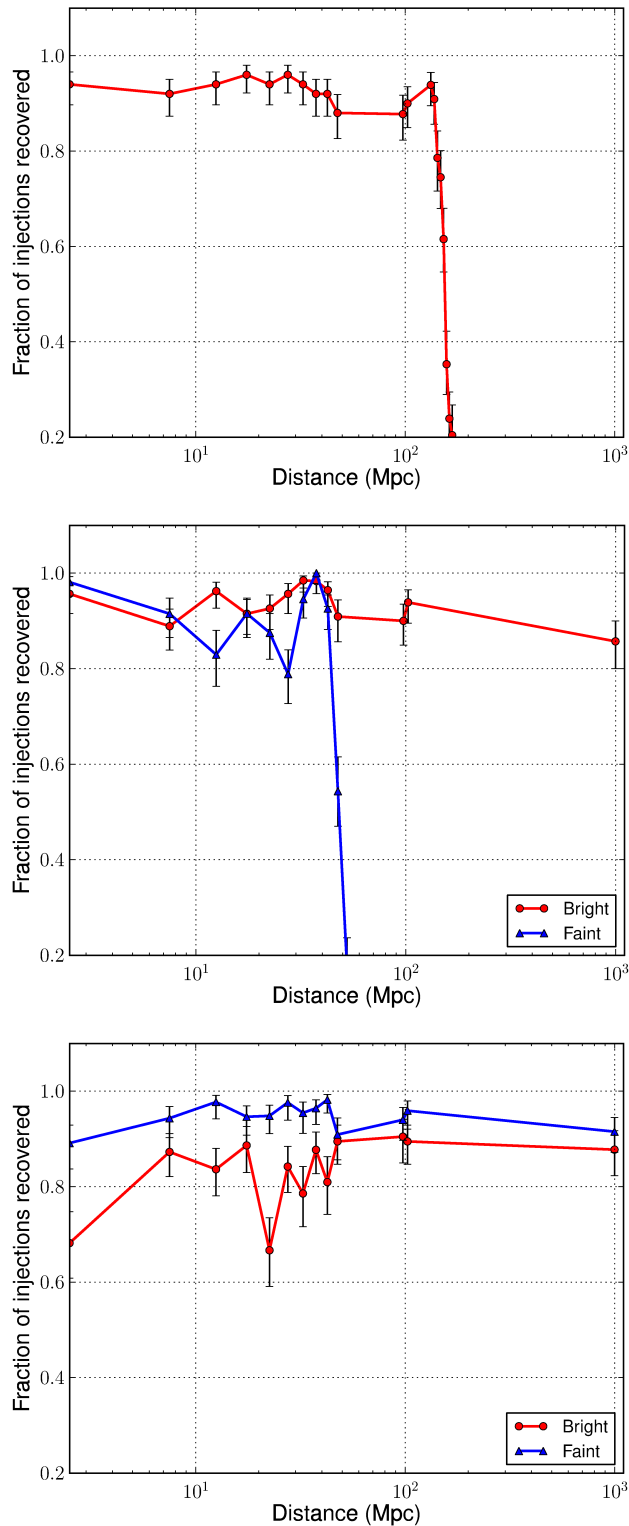


Figure 4.8: Plots showing the efficiency of the LT pipeline as a function of distance for the RATCam images. Using the Kilonova (top), SGRB afterglow (middle) and LGRB afterglow (bottom) models. For the GRB injections, we plot both the brightest (red) and faintest (blue) injections from the range of reference magnitudes given earlier. For the brightest LGRB injections, dips in efficiency are due to random overlap between multiple extremely bright injections which SExtractor cannot separate in the image. In practice it is highly unlikely that more than one extreme transient will appear in a single image. Given the small number of injections per bin, this has a large, unrealistic effect on efficiency calculations.

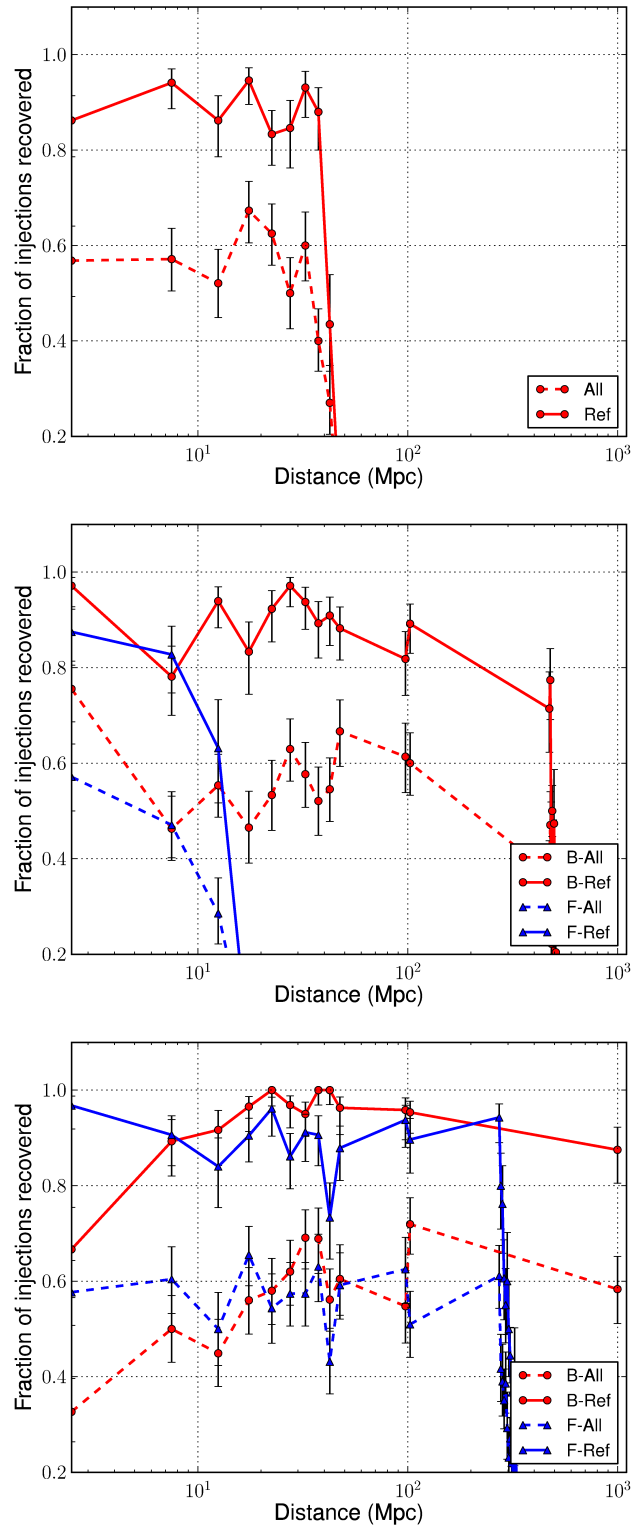


Figure 4.9: Plots showing the efficiency of the LT pipeline as a function of distance for the SkyCamZ images, with the same injection types as figure 4.8. The SkyCamZ reference image does not overlap entirely with the original images. For this reason two efficiency curves are plotted for each case in figure 4.8. The dashed line (B/F-All) is the efficiency calculated from all injections made in to the SkyCamZ images, regardless of overlap between the injected images and reference image, while the solid line (B/F-Ref) is the efficiency calculated only taking in to account injections made that are covered by the SkyCamZ reference image.

4.2.4 Analysis Results

The pipeline described in section 4.2.2 was used to analyse the RATCam and SkyCamZ-images separately. For RATCam we found 406 individual candidates before applying our cuts. Of these, 113 were associated with artefacts near the image edges and the bad pixel strip. Of the remaining 293, all but one was removed due to bad subtraction or not containing the required number of detections in the series of images. The final candidate was found near a minor planet and was therefore rejected. This left us with no remaining viable candidates. For SkyCamZ we found 163 individual candidates, 87 of which were considered to be artefacts near the image edges, and were removed. The remaining 76 did not pass the cut for required number of detections after being checked for bad subtraction. This also left us with no remaining candidates.

4.3 ROTSE Analysis

4.3.1 Follow-up Images Taken with the ROTSE Network

The ROTSE-III network consists of 4 robotic telescopes situated at Los Alamos, New Mexico, USA; Coonabarabran, Australia; Mt. Gamsberg, Namibia; and Bakirlitepe, Turkey, each with a 0.4m aperture. This provides a 3.5 square degree FoV. These telescopes imaged areas of the sky relating to 5 triggers produced by the GW pipelines described in section 2.2 using a ‘clear’, white light filter. The ROTSE observing strategy aimed to image the region 30 times in one night as soon after the trigger as possible, followed by 8 images for as many nights as possible for up to approximately one month after the trigger, each with either 20 or 60 seconds exposure time depending on Lunar brightness. This produced a total of 782 images for analysis, with limiting magnitudes of around 17th magnitude. Trigger G19377 was later revealed to be a “blind injection” created to test the capabilities of the GW data analysis pipelines, as described in section

Trigger ID	Date and time of 1st image (UTC)	Total no. of images analysed (No. of images taken)
G18666	2010-09-08 18:15:29.54	125 (125)
G19377	2010-09-16 18:26:59.70	102 (117)
G20190	2010-09-20 22:40:38.96	64 (257)
G21852	2010-09-27 08:17:30.12	72 (130)
G23004	2010-10-03 23:13:40.57	48 (153)

Table 4.1: List of GW triggers imaged by the ROTSE telescopes, along with date and time of the first image taken and the number of usable (total) images taken.

2.2.5. Trigger G18666 imaged the incorrect sky location due a software bug, as described in section 2.2.4. For this reason, images from G18666 were used during the testing of the ROTSE pipeline, providing an example of expected efficiencies but no analysis results.

As with the LT analysis, images that were of poor quality had to be removed. Table 4.1 lists the triggers the ROTSE telescopes imaged along with information on the images taken. Unfortunately only 411 of the original 782 images were useful for the analysis. Images were rejected primarily due to cloud or dust obscuring the sky, poor focusing and bright sky background due to a full Moon.

4.3.2 The ROTSE Image Analysis Pipeline

We used the existing ROTSE pipeline to reduce the images taken with the ROTSE telescope network. As with HOTPANTS used for the LT pipeline, this is based on the ISIS package⁶ which uses a single convolution algorithm described in Alard & Lupton (1998) and Alard (2000). ISIS performs best when the reference image is of better quality than the images to be analysed. This is not always the case with images from the ROTSE telescope network, which vary greatly due to temperature, telescope orientation, and atmospheric effects which can produce highly variable, often elliptical PSFs. The ROTSE pipeline was adapted by Yuan & Akerlof (2008) to use cross convolution (the convolution

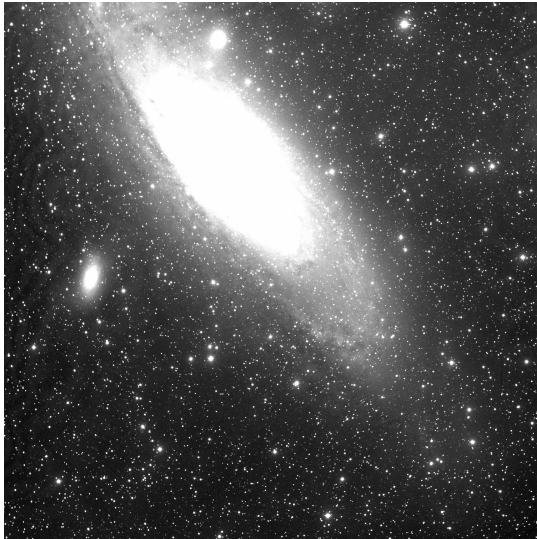
⁶<http://www2.iap.fr/users/alard/package.html>



(a) G19377



(b) G20190



(c) G21852



(d) G23004

Figure 4.10: Example images for each GW trigger imaged and analysed from the ROTSE telescope network.

of both the reference and original images) to improve image subtraction results. This pipeline was implemented for our analysis to require minimal user interaction and for large-scale image processing. On a typical night eight images are taken with exposure times of 60 seconds (20 seconds during a full moon), which are combined to improve the limiting magnitude of the images (hereafter called the 8-fold image). The original 8 images are also split into two groups of 4 and combined to produce two stacked images (hereafter called 4-fold images) from the same night. A reference image is then convolved and subtracted from these images and SExtractor is used to detect objects in the three residual images. During the image subtraction step, regions containing saturated stars are masked off and are not considered suitable for further analysis. For an object in a single night to be considered a candidate by the original pipeline the object must pass a set of criteria set by Yuan (2010) during the development of the ROTSE pipeline, described here:

- The object must appear in both of the 4-fold images, have a signal-to-noise ratio (SNR) of above 2.5 in the 4-fold images and above 5 in the 8-fold image.
- The object must also not move in position between the 3 images by more than 1 pixel for objects with $\text{SNR} > 15$ (1.5 pixels with $\text{SNR} < 15$) and must also have a FWHM no greater than twice the median FWHM of stars in the convolved reference image.
- If the object is found to be within 20% of the semi-major axis of a galaxy then a flux change of only 3% compared to the reference image is required. For other objects a change in flux of 60% is required.

After these selections have been applied further cuts are applied to reduce the number of candidates to less than 20 per image. If an image contains a large amount of candidates it is assumed that this is due to poor subtraction of the images, an example of which

is shown in figure 4.4. The following cuts are made in order until less than 20 objects remain:

- Objects found with 15 or more other objects within 250 pixels are discarded, as objects due to poor subtraction tend to be grouped together.
- Objects near the edges of images are removed as these regions are more susceptible to aberrations.
- Finally, the image size is reduced until either 20 objects remain or the image is 800 pixels across.

Objects remaining after the cuts outlined above are collated into a candidate list for each night. With the original ROTSE pipeline, these candidates were then analysed by hand, applying criteria such as checking for known variable stars or asteroids, or poor subtraction, in order to find interesting candidates for further investigation. However, due to the large number of images we have and the time-consuming process to produce the candidate lists and subsequent light curves, we needed to automate the pipeline to perform these manual checks and highlight any interesting candidates from the remaining lists of objects. The automation of the pipeline, described in Nuttall et al. (2012), combines the lists of objects from each night into one master list of unique objects which lists which images the object was seen in and the individual light curves of each object. A series of pass/fail “hard cuts” are applied to the objects. These cuts ensure that an object appears on more than one night, that it does not match a known variable star or asteroid found in the SIMBAD catalogue⁷ or the Minor Planet Checker, and that an object’s brightness decays by 0.5 magnitudes to be considered a candidate transient. Any objects which fail any of these tests are discarded. Any remaining candidates found within three times the major diameter of any galaxies within 50 Mpc⁸ in the

⁷<http://simbad.u-strasbg.fr/simbad/>

⁸This is the range of the detectors during the 2009-2010 science run to an optimally orientated Neutron Star - Black Hole merger.

Gravitational Wave Galaxy Catalogue described in chapter 3 (in order to account for the possibility that a NS-NS binary may have high enough velocities to leave their host galaxies), or with light curves that follow theoretical light curves shown in figure 4.6 are subsequently highlighted in the final candidate list. This final list typically contains less than 5 candidates, but rather than analyse each of these individually with equal weighting (since it is likely that most candidates will be from uninteresting transients unrelated to GWs), an ad-hoc ranking statistic, R , was created to rank these candidates based on their initial brightness, their rate of decay in brightness and the images in which they appear, which is defined as:

$$R \equiv \sum_i (18 - \text{mag}_i) \times \text{weight}_i \quad (4.4)$$

where

$$\text{weight}_i = \begin{cases} 1 & t_i - t_{\text{event}} < 1 \text{ day} \\ \left(1 + \log_{10} \frac{t_i - t_{\text{event}}}{1 \text{ day}}\right)^{-\alpha} & t_i - t_{\text{event}} \geq 1 \text{ day} \end{cases} \quad (4.5)$$

and the sum, i , is over all images the candidate was identified. The power law index α is chosen to be 3, which is the approximate gradient of the models discussed in section 4.2.3. Images taken with ROTSE have a typical limiting magnitude of ~ 18 , which is fainter than the images we have due to sky brightness during our triggers.

If a candidate was found to have a magnitude fainter than 18 on a specific night the rank for that night is taken to be zero. This ranking statistic was designed to prefer candidates which are at their brightest within a day of the trigger and are similar to the model light curves described in section 4.2.3. The statistic can then be compared to background events, as described in detail in Nuttall et al. (2012), in order to highlight likely candidates. This is done by choosing ~ 100 sets of images taken by ROTSE unrelated to GW triggers, with similar cadences, and analysing them using the same pipeline. The distribution of the ranking statistic of the candidates from those images

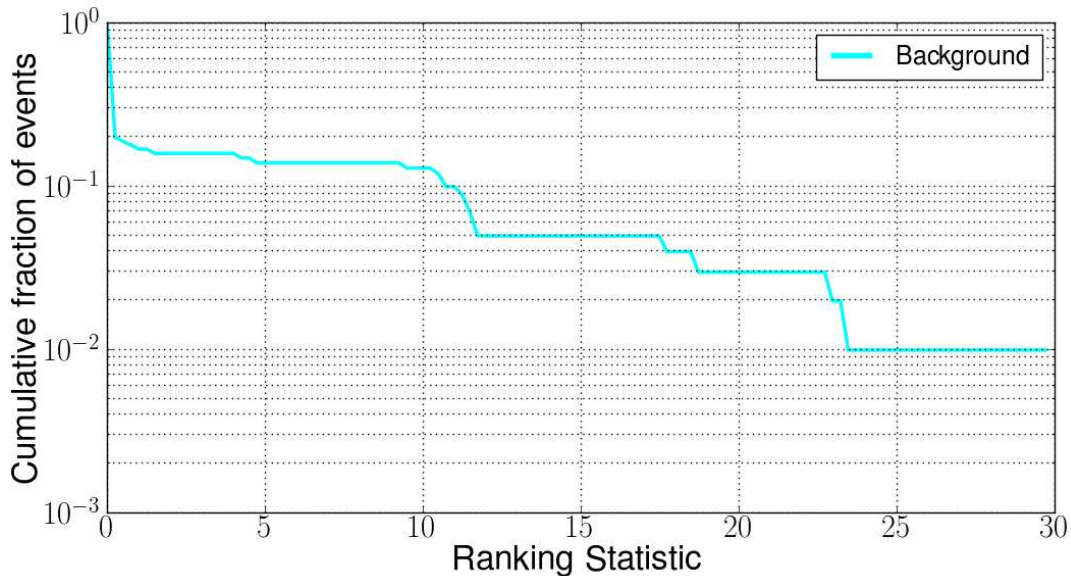


Figure 4.11: Distribution of the ranking statistic for background candidates, obtained from ~ 100 sets of images unrelated to GW triggers. Reproduced from Nuttall et al. (2012).

(which we call the background for this analysis) allows us to calculate the False Alarm Probability (FAP) for our candidates with similar ranking statistic values. The background distribution from these unrelated images is shown in figure 4.11. For example, if an object was detected with a ranking statistic of 11, it would have a FAP of around 0.1, while an object with $R = 25$ would have a FAP of 0.01. These values vary for each GW trigger imaged and analysed, as the background distributions were made for each trigger using background images that match the cadence of images taken for that particular trigger. For the ROTSE analysis we require a candidate to have a FAP of < 0.01 to be declared a detection, due to the need for conservative thresholds with first detections, while candidates with $\text{FAP} \lesssim 0.1$ would be considered for further follow-up observations where possible.

4.3.3 Efficiency of the ROTSE Pipeline

As with the Liverpool Telescope analysis, it is important to quantify the efficiency of the ROTSE pipeline to expected light curve models. For the ROTSE images we used

the same models as described in section 4.2.3, but the method for injection is different to take advantage of the many stars suitable for use as references. This is important for ROTSE due to the variation of the PSF across the image, which is difficult to recreate using a model PSF such as a Moffat profile. Additionally, a simple “cut-and-paste” of a star from one part of an image to another is not sufficient, as this will increase the noise in the region around the injected star. In order to circumvent this we use scaled bright, isolated stars in the field. This ensures that the object flux is dominated by Poissonian noise from the source, rather than sky or instrument noise, allowing a smooth injection which has a realistic PSF. A position close to the source star in the field is chosen at random as the injection position in order to match the PSF in the image region, along with a given light curve model and associated distance to the source. In each image, the background-subtracted flux of the original star is scaled according to the magnitude predicted from the light curve model, calculated using the time difference between the time of the GW trigger and the current image. The scaled flux, $F_{starscaled}$, is calculated using:

$$F_{starscaled} = \frac{F_{star}}{10^{\frac{mag_{image} - mag_{inj}}{-2.5}}} \quad (4.6)$$

where F_{star} is the flux of the original star, mag_{image} is the magnitude of the original star in the image and mag_{inj} is the required magnitude of the injected transient. In order to obtain realistic backgrounds it is necessary to scale the injection region by a factor f . Without scaling the injection region, the background noise added in quadrature, post-injection, will be:

$$\sigma(postinj)^2 = \sigma(preinj)^2 + \sigma(star)^2 \quad (4.7)$$

where $\sigma(star)$ is the standard deviation of the background around the source star, and $\sigma(preinj)$ and $\sigma(postinj)$ are the standard deviations of the background of the injection

region before and after injection respectively. The background noise, post injection, is therefore obviously larger than the original background noise. This can result in image subtraction in which this excess noise is clearly visible, possibly producing a higher than expected likelihood of detecting injections and increasing the error in photometry, depending on the methods used. In order to account for this, the injection region must be scaled so that the background before and after injection remains the same:

$$\sigma(\text{preinj})^2 = f^2 \times \sigma(\text{preinj})^2 + \sigma(\text{star})^2 \quad (4.8)$$

which rearranges to:

$$f = \sqrt{1 - \frac{\sigma(\text{star})^2}{\sigma(\text{preinj})^2}}. \quad (4.9)$$

By scaling the injection region before injecting the transient we reduce the background noise in the injection region, but also the mean of the injection region, so we therefore add a constant value across all pixels such that the mean of the background and the noise in the background remains the same post-injection. This constant is calculated by comparing the mean before and after scaling, and the difference is simply added to each pixel in the injection region. After adding our transient object, we have a smooth injection in which both the mean and standard deviations of the background are the same as before the injection. Two example injections, both with and without scaling, can be found in figure 4.12.

The efficiency of recovering injected transients varied across all 5 triggers due to issues with image quality. As shown in Figure 4.13, the ROTSE pipeline was able to observe simulated transients out to maximum distances of ~ 5 Mpc for kilonova, ~ 80 Mpc (~ 2 Mpc) for bright (faint) SGRB and ~ 1 Gpc (~ 50 Mpc) for bright (faint) LGRB

Additionally, due to the pipeline masking saturated objects nearby injections were ignored within the distance at which the brightness of the injected object was greater

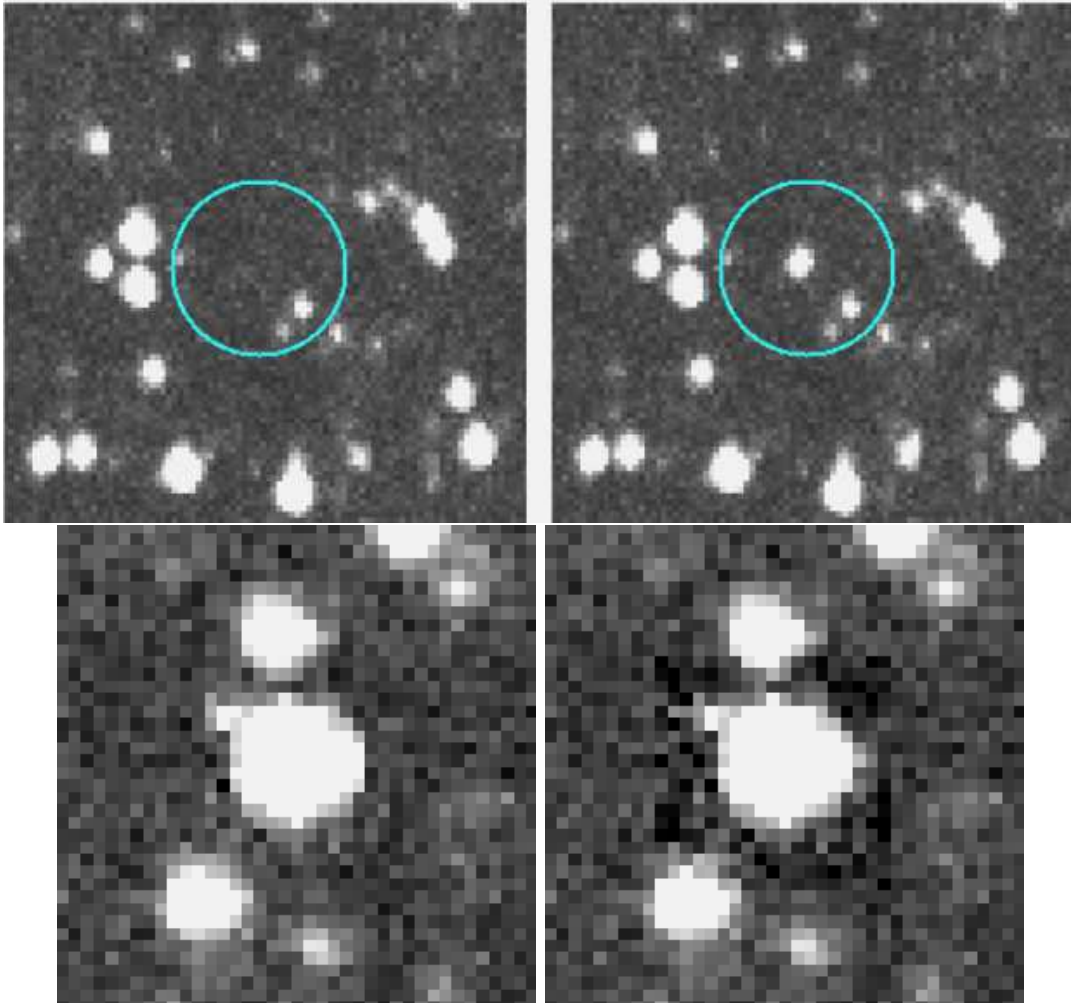


Figure 4.12: Examples of injected transients in a single image. The top images show a region of an image before (left) and after (right) injection of a bright object. The bottom image shows a different injection comparing the process with (left) and without (right) scaling the background in the manner described in section 4.3.3. As we can see, the injection made without correct scaling produces a region of higher noise surrounding the injected object, making it easy to distinguish between real and simulated transients.

than the saturation limit of the images. This corresponded to distances closer than .5 Mpc for kilonova, ~ 10 Mpc for bright SGRB and ~ 150 Mpc (3 Mpc) for bright (faint) LGRB transients, respectively. For the ROTSE analysis, triggers G18666, G19377 and G20190 recovered $\sim 80\%$ of injections around the distance at which these objects are no longer saturated, and decays with increasing distance. Triggers G21852 and G23004 have efficiencies of around 5% and 20% respectively before dropping rapidly with distance. This is due to the removal of poor images, due to extensive cloud or dust obscuring the sky, from the analysed data set.

4.3.4 Analysis Results

G19377

The ROTSE-IIIc telescope located in Namibia responded at $t+\sim 12$ hours and on subsequent follow-up nights ($t+6$ days to $t+29$ days) both ROTSE-IIIa (Australia) and c telescopes gathered images centered on the region $RA=115^{\circ}33'36''$ and $dec=-30^{\circ}0'0''$. Due to image quality issues described earlier only 72 of these images could be used in the analysis, with an average limiting magnitude of 15.1. Two galaxies at ~ 24 Mpc (PGC 078144 and PGC 078133) were visible within the FoV. The ROTSE image processing pipeline revealed 209 unique objects, one of which passed the candidate validation. Further tests found this candidate was consistent with background, with a false alarm probability of 10%. This left no significant candidates. As discussed in subsection 2.2.5, trigger G19377 was found to be a blind injection.

G20190

All four ROTSE-III telescopes responded to this GW trigger, taking images spanning $t+34h38m$ to $t+29d$, centered on the region $RA=333^{\circ}15'0''$ and $dec=18^{\circ}1'48''$. Due to image quality issues all images taken with the ROTSE-IIIa, b (USA) and d (Turkey)

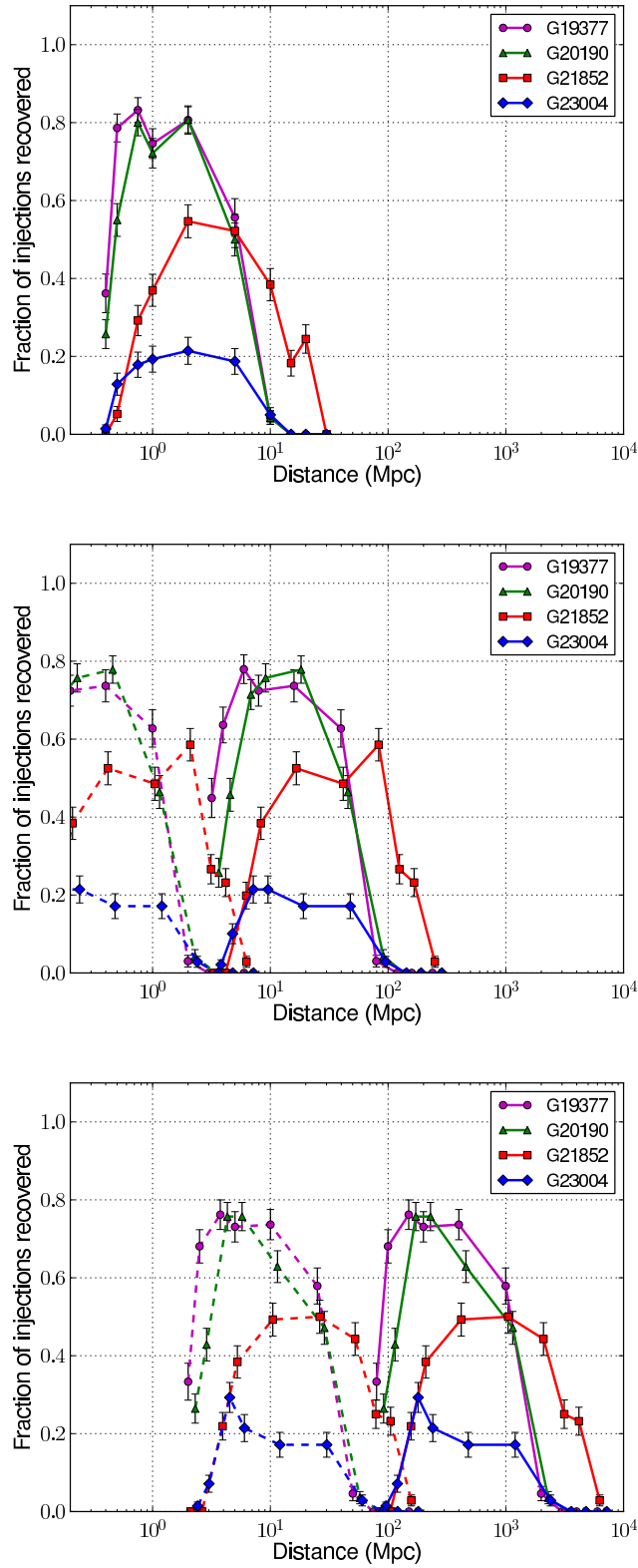


Figure 4.13: Plots showing the efficiency of the ROTSE pipeline as a function of distance in recovering simulated kilonovae transients (top), SGRBs (middle), and LGRBs (bottom). For the GRB injections only the brightest models were considered.

telescopes were discarded, resulting in 56 images being used for the analysis, with an average limiting magnitude of 15.5. The ROTSE image subtraction pipeline found 77 potential candidates, none of which passed the candidate validation procedure.

G21852

ROTSE-IIIb took images spanning $t+11\text{h}53\text{m}$ to $t+29\text{d}$ centered on the region $\text{RA}=11^{\circ}2'24''$ and $\text{dec}=41^{\circ}36'36''$ which, within its FoV, contained both M31 and M110. Due to image quality issues one follow-up night had to be ignored. The average limiting magnitude of the images was 16.6. The image subtraction pipeline found 187 objects, which resulted in four candidates after candidate validation. All four candidates overlapped with one of the galaxies mentioned, however all were consistent with background. The highest ranked candidate had a false alarm probability of 9%. Consequently we found no significant candidates.

G23004

The ROTSE-IIIb, c and d telescopes responded to G23004 at $t+6\text{h}25\text{m}$ and collected data up to $t+29\text{d}$. These images were centered on $\text{RA}=61^{\circ}58'12''$ and $\text{dec}=-20^{\circ}54'36''$ and contained one galaxy (NGC 1518) at 11.5 Mpc within the FoV. Around 75% of the data was of poor quality, resulting in the analysis of 30 images with an average limiting magnitude of 16.7. The ROTSE subtraction pipeline found 124 potential candidates of which none survived the candidate validation tests.

4.4 Conclusion

The work described in this chapter details two efforts to analyse images taken as part of the first EM follow-up campaign, performed as part of the 2009-2010 science run. We describe the data reduction pipelines for two observatories: the purpose built pipeline

for the Liverpool Telescope, and the ROTSE telescope analysis pipeline, altered to fit our needs. Using these pipelines, we find no optical transient candidates that pass our selection cuts. Other EM searches performed as part of the same follow-up campaign also find no viable EM candidates to GW triggers, as described in Aasi et al. (2014) and Evans et al. (2012) We simulate expected optical counterparts to assess the capabilities of the pipelines. We find that for the LT we were able to recover 80-90% of all simulated transients across the entirety of the 2009-2010 LIGO/Virgo distance range and beyond using the RATCam instrument. For the ROTSE pipeline, we were able to recover between 20-80% of all simulated transients across a smaller fraction of the same distances covered by the LT instruments. The differences between the two is due to a combination of poor quality images and the removal of saturated objects by the pipeline.

Chapter 5

Follow-up observations in the advanced detector era using GOTO

Advanced LIGO and advanced Virgo are set to begin operation from 2015/16, and are expected to provide the first direct detection of GWs. The most promising sources for detection are compact binary star mergers. A subset of these sources, NS-NS and NS-BH mergers, are also expected to be a significant source of EM radiation, such as SGRBs, and X-ray and optical transients, as described in chapter 2. Detection of these EM counterparts will not only help validate the GW detection, but will also provide complementary information on the nature of the source, as discussed in chapter 2. Therefore, a follow-up strategy which provides the best chance of detecting EM counterparts must be planned in the build up to the advanced detector era. The purpose of this chapter is to provide justification for the specifications of a rapid-response telescope, which we call the Gravitational-Wave Optical Transient Observatory (GOTO), designed to image EM counterparts soon after a possible GW detection. This work is the result of a collaboration between myself, Vik Dhillon, Ed Daw and Don Pollacco (Warwick University). My input to the design has been the investigation of the optical counterparts we wish to

observe, and the capabilities of the advanced detector network in terms of sky localisation, distance reach and timescales of detector commissioning. By combining these I was able to produce a design specification of a telescope which could cover the majority of optical counterparts across the distance range of aLIGO and AdV. I presented this work at the “Gravitational Wave - Electromagnetic Follow-up with UK Facilities” meeting at Warwick University¹, and the work presented in this chapter is expected to form the basis of a grant proposal to STFC in 2014 for funds to build GOTO.

5.1 The Advanced Detector Era

In this section we summarise the current plan for aLIGO/AdV detector installation and commissioning. We also discuss the detection and localisation capabilities during the commissioning of the advanced detectors, and summarise the impact this has on the requirements of a dedicated optical follow-up telescope.

Since the completion of the 2009-2010 science run in October 2010 the LIGO and Virgo interferometers have been undergoing a series of upgrades, such as the installation of more complex suspension systems, more powerful lasers and larger mirrors, which are expected to increase sensitivity by a factor of ~ 10 compared to the initial detectors. For aLIGO and AdV, this will result in a NS-NS merger range of approximately 200 Mpc and 130 Mpc, respectively, a 10-fold increase in range. It is important to note that these distances are the orientation and sky location averaged distance to merging NS-NS systems with two $1.4 M_{\odot}$ NSs. The limiting horizon distance is roughly twice this range for an optimally located and oriented (face-on) system, and also increases with the total mass of the system. A more detailed description of aLIGO can be found in Harry & LIGO Scientific Collaboration (2010). Initially, the installation of aLIGO called for two detectors to be installed at Hanford (replacing the 2 km H2 detector with a 4 km

¹http://www2.warwick.ac.uk/fac/sci/physics/research/astro/gwem_meeting

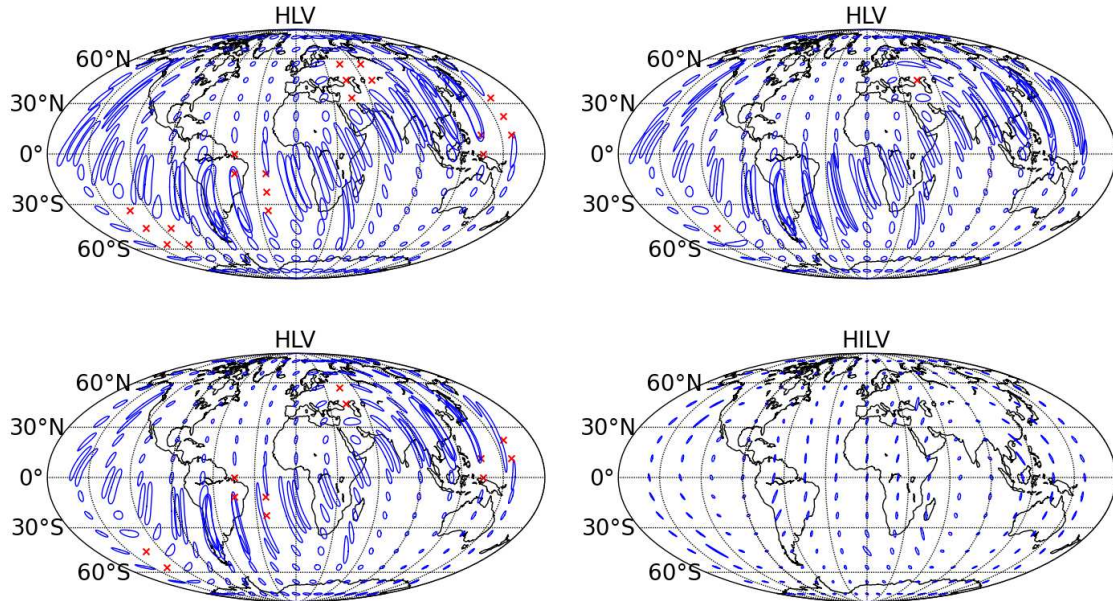


Figure 5.1: Network sensitivity and localisation accuracy for face-on NS-NS systems with advanced detectors comprised of Hanford (H), Livingston (L), Virgo (V) and India (I). The ellipses show 90% confidence localisation areas, and the red crosses show regions of the sky where the signal would not be confidently detected. The top two plots show the localisation expected for a NS-NS system at 80 Mpc by the HLV network in the 2016-17 run (left) and 2017-18 run (right). The bottom two plots show the localisation expected for a NS-NS system at 160 Mpc by the HLV network in the 2019+ run (left) and by the HILV network in 2022+ with all detectors at final design sensitivity (right). Reproduced from LIGO Scientific Collaboration et al. (2013).

interferometer). However, in order to improve the localisation of signals for EM follow-up observations, the decision was made to move the third LIGO interferometer to a site in India, with construction and commissioning expected to be completed sometime in the early 2020s. Unless indicated otherwise, the commissioning and observing schedule, sensitivities and limits discussed here are for the combination of the two US-based aLIGO (H: Hanford, L: Livingston) and one Italian AdV (V:Virgo) detectors only.

5.1.1 Commissioning and Observing Schedule

The ongoing upgrades are expected to be completed sometime during 2015, after which there will be an extensive commissioning period (LIGO Scientific Collaboration et al.,

Epoch	Estimated Run Duration	NS-NS Range (Mpc)		Number of NS-NS Detections	Median localisation (deg ²)	% NS-NS localised within	
		LIGO	Virgo			5 deg ²	20 deg ²
2015	3 months	40 - 80	-	0.0004 - 3	2000	-	-
2016-17	6 months	80 - 120	20 - 60	0.006 - 20	70	2	15
2017-18	9 months	120 - 170	60 - 85	0.04 - 100	84	1	12
2019+	(per year)	200	85 - 115	0.2 - 200	31	5	37
2022+ (India)	(per year)	200	130	0.4 - 400	11	19	73

Table 5.1: Summary of a plausible observing schedule, expected sensitivities, estimated source rates and source localisation with the advanced LIGO and Virgo detectors for a binary neutron star (NS-NS) comprised of two $1.4 M_{\odot}$ NSs. The NS-NS ranges and 90% localisation area reflect the uncertainty in the detector noise spectra. Reproduced from LIGO Scientific Collaboration et al. (2013).

2013). This time will be used to fine tune the detectors to design sensitivity, and will consist of a combination of engineering runs to calibrate upgrades and short science runs to assess the capabilities of the detectors during final observing-run conditions. An example of the final sensitivity of aLIGO can be seen in figure 1.4, which shows that aLIGO should be able to observe a large fraction of expected compact binary mergers. These science runs will allow some follow-up capabilities, but at shorter distance limits and science run length than the final configuration. The planned observing schedule can be seen in table 5.1, but this is likely to change somewhat in response to the success of the preceding engineering runs. During the first short run in 2015 there is a small possibility that AdV will join with a NS-NS range of around 20 Mpc, with longer joint science runs taking place each year until design sensitivity is reached towards the end of the decade. At this point the detectors are expected to observe as continuously as possible in a so called “Joint Science Mode”. Given the commissioning schedule, a dedicated observatory would need to be ready by 2016 at the latest. However, if we wish to determine the typical background transient rate, a year of observations would be required, so a date for “first light” of 2015 would be ideal.

5.1.2 aLIGO/AdV Detection Capabilities

As shown in table 5.1, the distance range for a NS-NS merger is expected to improve dramatically over the course of detector commissioning. If we assume all three detectors are required for triangulation, a limiting factor for EM follow-up projects similar to that undertaken during the 2009-2010 joint science run described in chapter 2 is the distance range of AdV, which will reach around 130 Mpc at the end of commissioning in 2020. However, the actual distance range of the 3-detector network depends on the combined SNR of the GW signal in all three detectors, which also depends on the parameters of the system being observed. However, a combined distance range of 150-180 Mpc at the design sensitivity of the HLV network is not unreasonable. The sky localisation, which varies greatly across the sky, is also not expected to improve drastically until LIGO-India is completed in the early 2020s, as shown in figure 5.1. This figure shows the evolution of sky localisation as the detectors increase in sensitivity. The top two plots show the localisation across the sky for a $1.4 M_{\odot}$ - $1.4 M_{\odot}$ NS-NS binary merger at a distance of 80 Mpc. Sky localisation improves as the sensitivity of the detectors, and subsequently the SNR of the source, increases from the 2016-17 run (left) to the run 2017-18 (right). The bottom plots are for sources at 160 Mpc during the 2019 run (left) and the 2022+ run (right), the latter including LIGO-India, which increases the median localisation, particularly for sources along the plane of the original network consisting of the LIGO-L, LIGO-H and Virgo detectors. Kasliwal & Nissanke (2013) argue that it may be possible to provide some localisation using only the two LIGO detectors, with median sky errors of 200-300 square degrees, for NS-NS mergers. However, the localisation is limited to specific regions of the sky and will have some error regions of up to 1000 square degrees. Given the relatively short science run for LIGO-only, it is logical to consider only the 3-detector network consisting of LIGO-Livingston, LIGO-Hanford and Virgo for the remainder of this chapter. In this case, an observatory designed for EM follow-up

in the advanced detector era must be able to observe a sky region covering tens of square degrees and be able to observe EM counterparts to expected sources (see section 5.2.1) out to a distance of at least 150 Mpc.

5.2 Optical Follow-Up with aLIGO/AdV

In this section, we summarise the properties of the optical counterparts we expect from NS-NS mergers and how the capability of the advanced detectors impact on the EM follow-up of these counterparts, which we use to justify the design specification of a telescope to be used for rapid optical follow-up observations to GW triggers during the advanced detector era.

5.2.1 Optical Counterparts

Since NS-NS mergers are expected to be the source of the first detection of GWs (see chapters 1), and they are expected to provide significant detectable EM emission (see chapter 2), it is reasonable to prioritise these systems for GW-EM follow-up searches. During the 2009-2010 science run, images were analysed and efficiencies calculated using the properties of observed optical afterglows detected of short and long GRBs (Kann et al., 2010, 2011), and early theoretical kilonova light curves (Metzger et al., 2010, and see chapter 4 of this thesis). Recently, van Eerten & MacFadyen (2011) produced a series of updated theoretical light curves for on- and off-axis short GRB afterglows. These models were presented, along with updated models for isotropic kilonovae emission, by Metzger & Berger (2012), which are discussed in more detail in chapter 2. The Metzger & Berger (2012) and van Eerten & MacFadyen (2011) light curves can be seen in figures 5.2 to 5.4, which show a series of possible models for R -band optical afterglows due to NS-NS mergers at various distances. These models are for optical afterglows due to the interaction of the GRB jet with the surrounding interstellar medium and the kilonova

decay of neutron rich matter surrounding the merger remnant, which does not depend on the orientation of the system. As can be seen, the further off-axis a GRB afterglow is, the fainter the beamed optical afterglow. Fortunately, the detection range of NS-NS and NS-BH mergers for LIGO and Virgo is also dependent on the angle the system is viewed in a similar manner, so for an on-axis NS-NS merger both the GW and optical afterglow emission will be brighter than for an off-axis merger.

5.2.2 Impact of Advanced Detector Capabilities on EM Follow-Up

In this section we use the distance and localisation limitations of the advanced detectors, listed in table 5.1, and the model light curves presented in figures 5.2 to 5.4 and tables 5.2 to 5.6, to discuss the limitations of any EM follow-up program in the advanced detector era, and the requirements needed for a dedicated optical follow-up observatory.

Limiting Magnitude

The limiting magnitude of a telescope designed to follow-up LIGO/Virgo candidates is a critical parameter in the success of detecting the optical transients described in section 5.2.1. During the 2009-2010 science run, partner telescopes covered a range of limiting magnitudes, from 12th (Pi of the Sky) to $\sim 21^{\text{st}}$ (Liverpool Telescope - RATCam) magnitude, as described in chapter 2. However, the majority of GW triggers were imaged by telescopes with limiting magnitudes of around 15-16, such as the ROTSE telescopes described in section 4.3. As shown in figure 4.13, such telescopes can only detect kilonova afterglows at maximum distances of the order of 10 Mpc, while the brightest short GRBs can only be seen out to distances of around 100 Mpc. By comparison, the LT can see kilonova afterglows out to distances of around 150 Mpc and bright SGRBs at over 1 Gpc (see figure 4.13). This leads to the conclusion that for a telescope for use during advanced

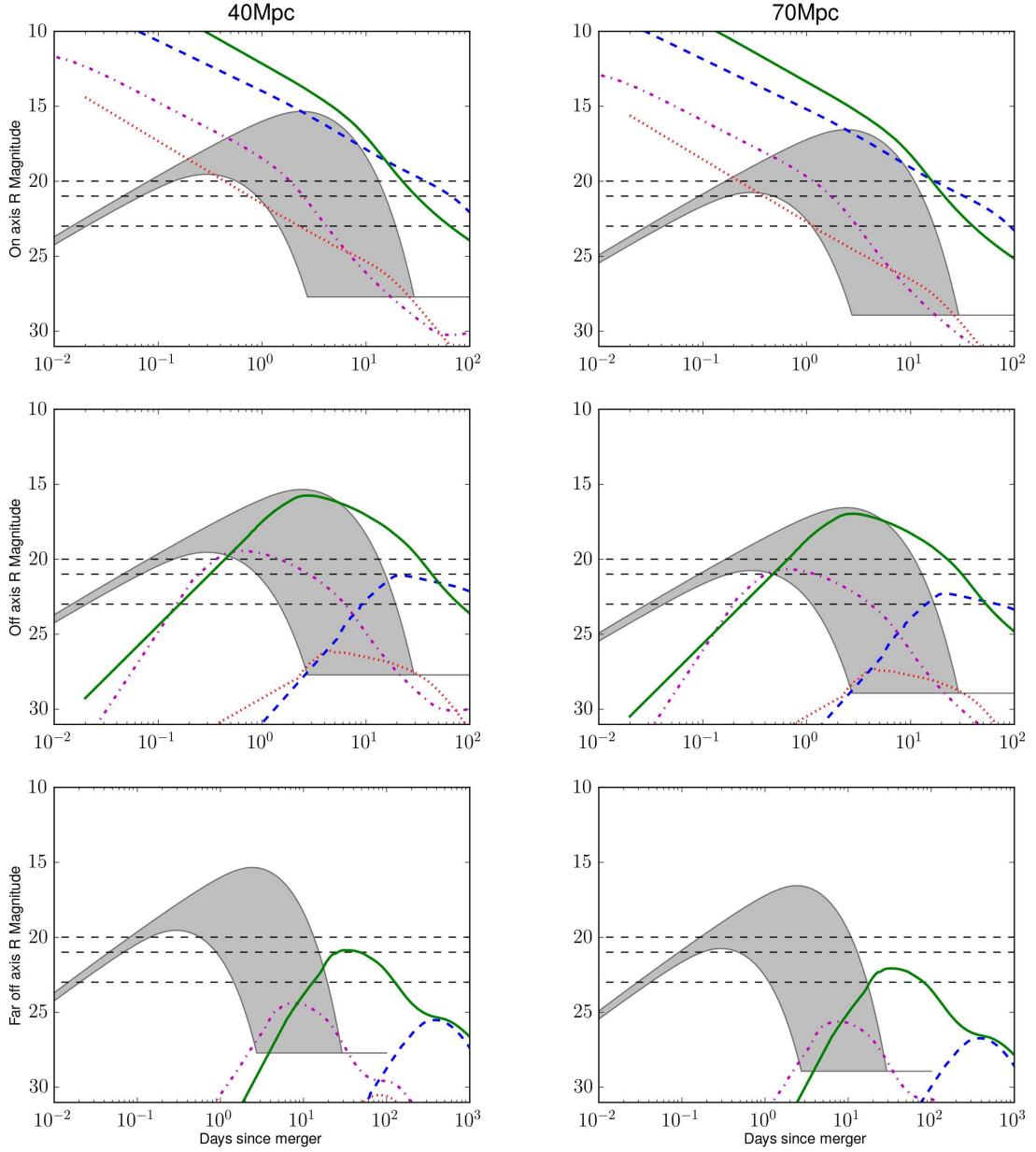


Figure 5.2: Afterglow lightcurves at distances of 40 (left) and 70 Mpc (right) for on-axis ($\theta \sim \theta_j$, top), off-axis ($\theta \sim 2\theta_j$, middle) and far off-axis ($\theta \sim 4\theta_j$, bottom), where the jet opening angle $\theta_j = 0.2$. The four models describe different jet energies, E_j , and density of interstellar medium surrounding the source, n . Green-solid: $E_j = 10^{50}$ ergs, $n = 1\text{cm}^{-3}$; Blue-dashed: $E_j = 10^{50}$ ergs, $n = 10^{-3}\text{cm}^{-3}$; Magenta-dot-dashed: $E_j = 10^{48}$ ergs, $n = 1\text{cm}^{-3}$; Red-dotted: $E_j = 10^{48}$ ergs, $n = 10^{-3}\text{cm}^{-3}$. The grey shaded region is the isotropic kilonova emission from the decay of neutron rich matter surrounding the merger remnant, spanning the expected range of ejecta mass and velocity, with estimated uncertainty in nuclear heating and opacity parameters. These are R -band apparent magnitudes not corrected for interstellar extinction. Created using light curves taken from Metzger & Berger (2012) via private communication.

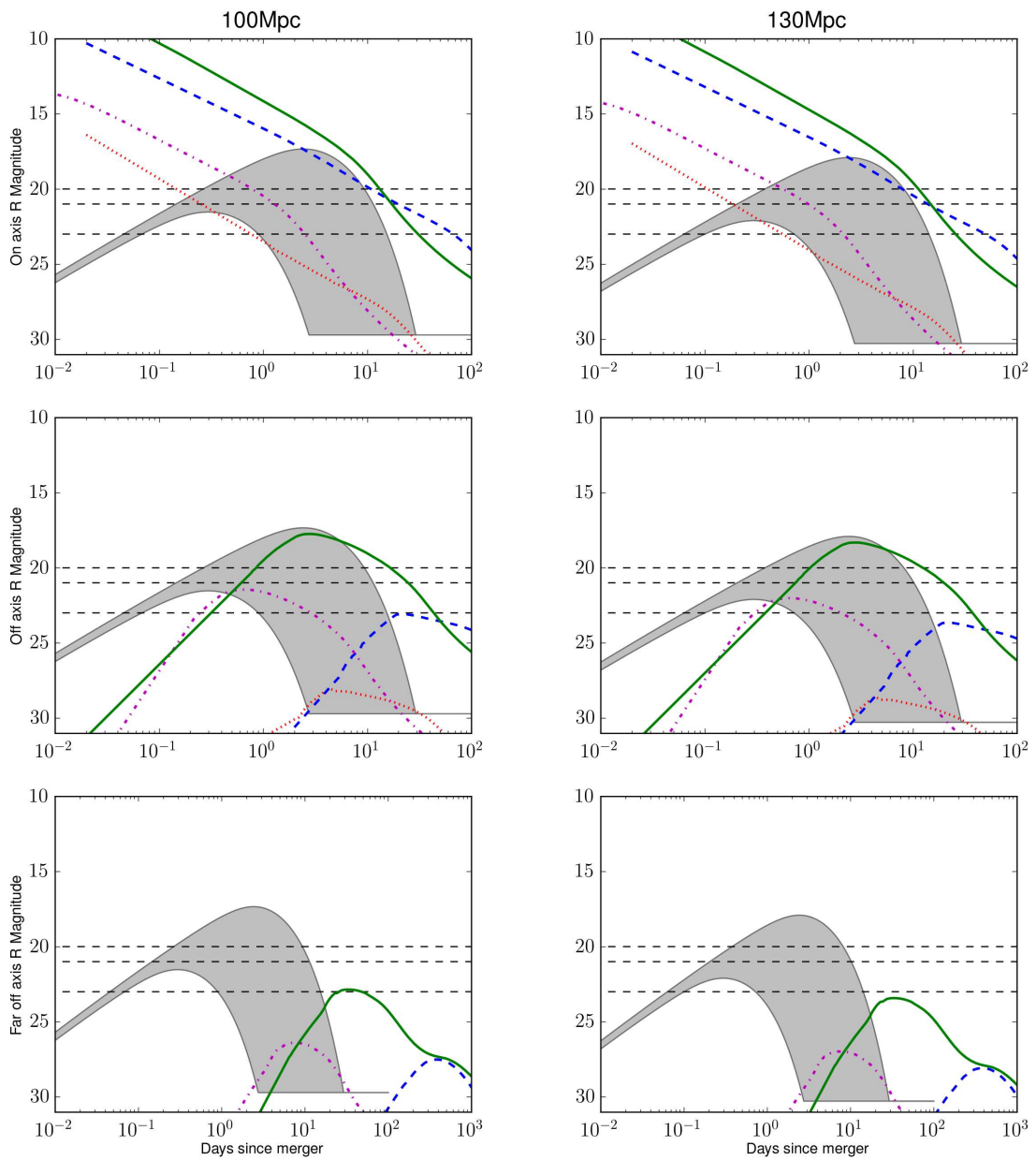


Figure 5.3: As in figure 5.2 but for distances of 100 (left) and 130 Mpc (right).

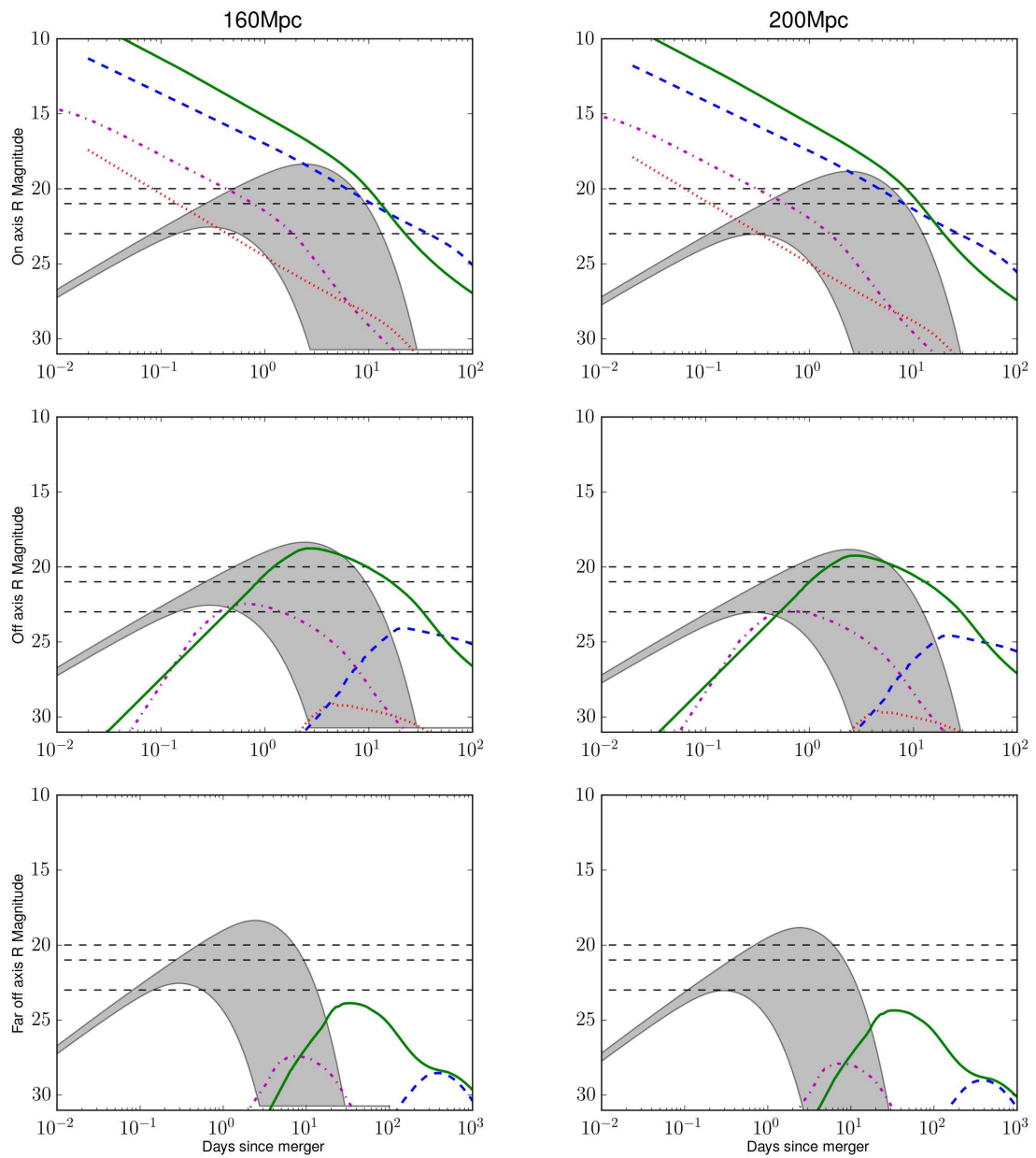


Figure 5.4: As in figure 5.2 but for distances of 160 (left) and 200 Mpc (right).

detector science run to be successful, it will ideally be able to observe as many possible EM counterparts over as much of the aLIGO/AdV distance range, and corresponding optical counterpart magnitude range, as possible. One measure of the capabilities of a telescope with a given magnitude limit is simply a comparison of which sources are clearly visible above the magnitude limit at any reasonable time after the initial trigger: between approximately 30 minutes from the trigger, the typical response time for follow-up observations during the 2009-2010 joint LIGO/Virgo science run, to 100 days after trigger. The visibility of the models shown in figures 5.2 to 5.4 over varying distances is listed in tables 5.2 to 5.6. As we can see, there is only one case at 200 Mpc that is not visible at 20th but is visible at both 21st and 23rd magnitude. Similarly, there are two models, one at 40 Mpc and one at 100 Mpc, that are only visible for a limiting magnitude of 23. From this we can conclude that a telescope capable of reaching 21st magnitude would be capable of imaging the vast majority of models shown in tables 5.2 to 5.6.

Sky Localisation

The sky localisations given in table 5.1 and shown in figure 5.1 seem to vary little with time until LIGO-India joins the network of detectors. While it is true that the fourth detector will vastly improve the error regions, it is important to note that the localisations are given for the set distances discussed in the caption of figure 5.1. Therefore, as the sensitivity of the detectors increases, NS-NS systems at fixed distances will give slightly improved localisations due to higher SNR in the detectors. However, this improvement will not be as great as the introduction of LIGO-India, and NS-NS mergers before then will still have localisations of the order of tens of square degrees.

Another contributing factor is the positioning of the telescope on the Earth's surface with respect to the sky localisation regions provided by LIGO/Virgo during the commissioning of the detectors, as shown in figure 5.1. Off-axis afterglow models are expected to peak and persist for several days, as shown in figures 5.2 to 5.4. However, for dis-

Mag	40 Mpc		100 Mpc		200 Mpc	
	on	off	on	off	on	off
20	✓	✓	✓	✓	✓	×
21	✓	✓	✓	✓	✓	✓
23	✓	✓	✓	✓	✓	✓

Table 5.2: Table listing the visibility of on- and off-axis SGRB optical afterglows for jet energy and interstellar medium density of $E_j = 10^{50}$ ergs and $n = 1 \text{ cm}^{-3}$ respectively, as shown in figures 5.2 and 5.3 for limiting magnitudes of $R=20, 21$ and 23 at distances of 40, 100 and 200 Mpc.

Mag	40 Mpc		100 Mpc		200 Mpc	
	on	off	on	off	on	off
20	✓	×	✓	×	✓	×
21	✓	×	✓	×	✓	×
23	✓	✓	✓	×	✓	×

Table 5.3: As in table 5.2 but for $E_j = 10^{50}$ ergs and $n = 10^{-3} \text{ cm}^{-3}$.

Mag	40 Mpc		100 Mpc		200 Mpc	
	on	off	on	off	on	off
20	✓	✓	✓	×	✓	×
21	✓	✓	✓	×	✓	×
23	✓	✓	✓	✓	✓	×

Table 5.4: As in table 5.2 but for $E_j = 10^{48}$ ergs and $n = 1 \text{ cm}^{-3}$.

Mag	40 Mpc		100 Mpc		200 Mpc	
	on	off	on	off	on	off
20	✓	×	✓	×	✓	×
21	✓	×	✓	×	✓	×
23	✓	×	✓	×	✓	×

Table 5.5: As in table 5.2 but for $E_j = 10^{48}$ ergs and $n = 10^{-3} \text{ cm}^{-3}$.

Mag	40 Mpc	100 Mpc	200 Mpc
20	✓	✓	✓
21	✓	✓	✓
23	✓	✓	✓

Table 5.6: Table listing the visibility of kilonova light curves shown in figures 5.2 and 5.3 for limiting magnitudes of $R=20, 21$ and 23 at distances of 40, 100 and 200 Mpc.

tant on-axis models, which peak within a few minutes and decay rapidly as discussed in chapter 2, it can be argued that rapid follow-up is best suited to telescopes located near a region of good sky localisation. A smaller sky area allows faster imaging of the entire error region for telescope FoVs smaller than the localised area (i.e. less tiling is required to image the entire error region). It is important to note that the error regions are those on the sky with respect to the fixed ground positions of the LIGO/Virgo detector at the time of detection. Using the top left plot in figure 5.1 as an example, if the sky localisation of a detection was found to be above Eastern China, the sky region would be highly elongated. Approximately 9 hours later, when this region of sky is visible for a telescope located in La Palma, the skymap for the detection will still be elongated and not similar to the localisation errors above La Palma at the time of GW detection.

Previous attempts to perform EM follow-up have shown that sky regions are not likely to be one contiguous region but are in fact composed of several smaller regions, as demonstrated in figure 5.5, which can complicate EM follow-up planning and observations. This suggests that the ability to simultaneously image the whole region with a series of tiles is important, rather than aiming to image the entire region with a single, large FoV detector. The 2009-2010 follow-up attempt also made use of a galaxy catalogue. For the early advanced detector era, this may still be a useful method, but as shown in Kanner et al. (2012), at 200 Mpc a 100 square degree error region could contain around 1000 galaxies. Aiming to image each galaxy individually will eventually become too time consuming for narrower field instruments, especially when the rapid decay of on-axis afterglows requires prompt (<1 hour) observations to obtain as much information about the prompt afterglows as possible. This leads us to a wide-field design capable of imaging to faint magnitudes, as described in the next section, although using a galaxy catalogue to prioritise important regions within the larger skymaps could still be useful.

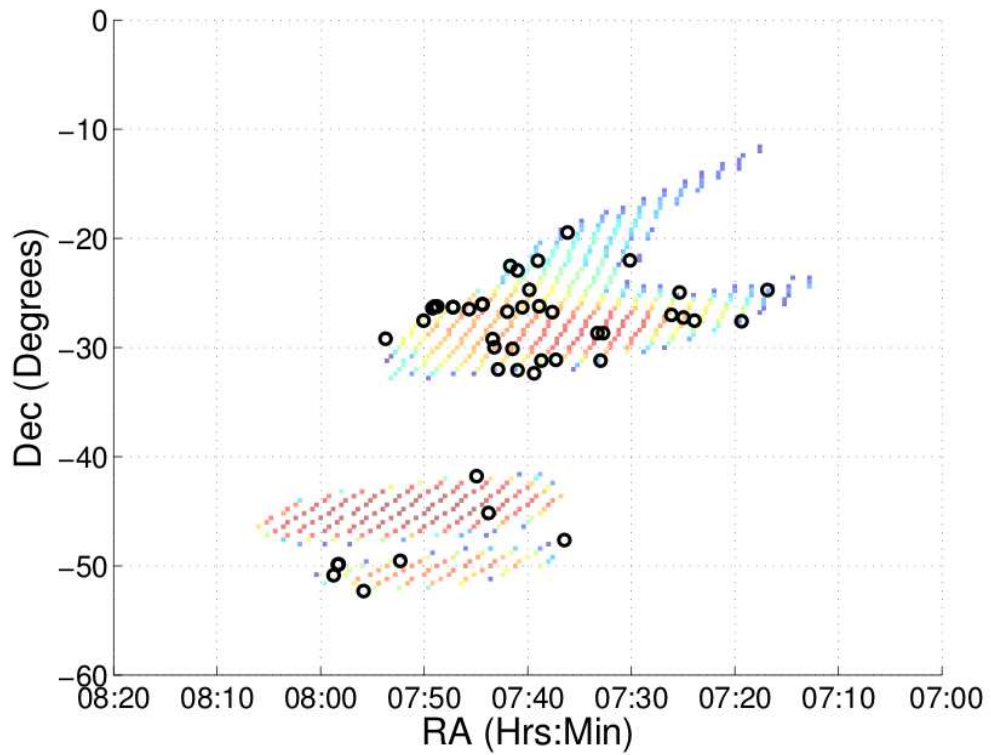


Figure 5.5: A typical sky map showing the region associated with a possible detection (in this case a blind injection study), with known galaxies highlighted by black circles. The colour represents the source location probability distribution across the sky above a given threshold (red: high, blue: low). Reproduced from <http://www.ligo.org/science/GW100916/>

5.2.3 GOTO - The Gravitational-Wave Optical Transient Observatory

In order to be successful in performing follow-up observations of GW triggers in the advanced detector era, a telescope must fulfill the following requirements:

- **Field of view and limiting magnitude:** The ability to image the entire GW sky localisation region to a suitable depth is the main driver in the design of a new telescope. There are several telescopes which can achieve either the required FoV or faint magnitude limit, but currently none available for triggered follow-up observations that do both. The advanced detector era makes this even more important. The median error region is several tens of square degrees until LIGO-India comes online. Since the majority of models discussed earlier in this chapter that will be detectable at the distance ranges expected from aLIGO/AdV will be brighter than 21st magnitude, then a telescope with a FoV of between 50 and 100 square degrees capable of imaging down to $R \simeq 21$ is suitable.
- **Tiled localisation region:** Due to the irregular skymaps produced by the GW trigger pipelines, the ability to observe the entire error region is not usually possible for a telescope with a square FoV. Therefore, a series of individually steerable detectors or telescopes that can be aligned to cover the error region as closely as possible would be well suited to GW-EM follow-up.
- **Response time and location:** Due to the short timescale of some of the fainter on-axis afterglows and the delay from GW signal to observing request of 30-40 minutes, a response time of less than 1-2 hours increases the information obtainable through EM observations. As discussed in chapter 2, GRB afterglows have rise times of a few minutes to half an hour, after which the decaying afterglow is visible for a couple of hours to a couple of days above 21st magnitude. Therefore, in order

to gain as much information from the decay of these afterglows as possible, the source must be imaged as quickly as possible. The localisation of the GW detectors is also a factor here, as smaller error regions of a few tens of square degrees can be covered in fewer pointings than large error regions spanning several hundreds of square degrees. Therefore, a fast-response robotic telescope placed in either La Palma or Australia would be ideal due to the smaller sky localisation errors above these locations, as shown in figure 5.1.

- **Wavelength range:** Metzger & Berger (2012) describe the spectra of their models as similar to a thermal blackbody with $T \approx 10^4$ K. This would produce a peak in the near-UV region of the spectrum. However, use simple line data for iron to estimate opacities. Metzger & Berger (2012) argue that taking into account more detailed opacities is likely to produce counterparts that peak in the *R*-band, so a red-optimised optical telescope is suitable.
- **Construction timescale:** The current schedule for construction of the advanced detectors expects routine observations from aLIGO and AdV from 2016. Taking into account the usefulness of having a year prior to the first science run to study the optical transient sky (which can help remove contaminating transients from the searches) it is obvious a quick construction time is needed. For this reason, an optical follow-up telescope would need to be commissioned by 2015. Such a short construction timescale demands the use of off-the-shelf components and reusing existing hardware and software where possible. If the telescope is to be located in La Palma, the existing infrastructure for the new-retired SuperWASP observatory could be used.

The above requirements define the specification of a telescope which can cover 50-100 square degrees to around 21st magnitude. This FoV would cover the median sky localisations listed in table 5.1 for the first 3-4 years of joint science runs with the

advanced detectors, and as shown in figures 5.2 to 5.4, this limiting magnitude would allow us to observe a significant fraction of on- and off-axis SGRB afterglows and kilonova emission during at least the first ~ 5 years of LIGO/Virgo commissioning. Moreover, the telescope would need to be able to cover highly asymmetric sky regions: such a requirement could be achieved with eight individual telescopes capable of observing 3×3 degrees each, giving a total of ~ 70 square degrees. By taking advantage of the latest 9000×9000 pixel CCDs (see Atwood et al., 2012, for example), with a pixel size of $10 \mu\text{m}$, we can calculate the specification of each telescope assuming typical parameters for sky brightness, readout noise, and dark current noise. Since we require a field of view of 3 degrees ($10,800''$), and our CCD will be 90mm across (9000 pixels at $10 \mu\text{m}$ per pixel), we can calculate the platescale, p , required:

$$p = \frac{10800}{90} = 120''/\text{mm}. \quad (5.1)$$

The platescale is related to the focal length, F , of the telescope via the equation:

$$p = \frac{206265''}{F}. \quad (5.2)$$

Rearranging, and using the platescale calculated in equation 5.1, we get a focal length of:

$$F = \frac{206265}{p} = \frac{206265}{120} = 1719 \text{ mm}. \quad (5.3)$$

The focal ratio, f , of a telescope is the ratio between the focal length, F , and the diameter of the primary mirror, D . For a telescope with a given focal ratio, we can then calculate the mirror diameter needed to observe the field required. However, the size of the mirror also affects the exposure time needed to achieve a given SNR (dependent on sky conditions), so the calculation is an iterative process to obtain the required specifications. Here we present the specification of a telescope which gives us an SNR of 5.5, calculated

using equation 5.13. For a telescope with a focal ratio of $f/6$ we obtain a mirror diameter of:

$$D = \frac{F}{f} = \frac{1719}{6} = 286 \text{ mm.} \quad (5.4)$$

Therefore a mirror of approximately 30cm in diameter will be suitable. However, if the telescope requires a larger mirror (for example if an image with a fainter limiting magnitude for a given exposure is needed), then a different focal length telescope is needed to obtain the same FoV. For example, a mirror of around 45cm will require a telescope with a focal ratio of $f/4$. This can impact the cost of the telescope, as faster focal-ratio telescopes are generally more complex, and hence more expensive. In our case, we are aiming for simple specifications in order to keep costs low, so an $f/6$ telescope is suitable.

To demonstrate the suitability of this telescope design for optical follow-up, we must calculate the SNR of a typical observation of an object at the desired magnitude limit of $R = 21$. The relation between the flux, F , and apparent magnitude, m , of two objects can be written as:

$$m_1 - m_2 = -2.5 \log \left(\frac{F_1}{F_2} \right). \quad (5.5)$$

Using a standard flux zero-point, F_{ZP} , which is defined as the flux detected for a star with apparent magnitude, $m = 0$, we can re-write this relationship to find the flux of an object we wish to observe:

$$m_{obs} = -2.5 \log \left(\frac{F_{obj}}{F_{ZP}} \right). \quad (5.6)$$

However, m_{obs} is the magnitude observed for a star seen through the atmosphere, so we must also correct for atmospheric extinction. To do this, we define the relation between the above atmosphere magnitude and observed magnitude as

$$m_{obs} = m_o + k \sec Z, \quad (5.7)$$

where m_o is the above-atmosphere magnitude of the object, k is the extinction coefficient² and $\sec Z$ is the airmass (where Z is the angle from the zenith that the object is observed).

This gives us:

$$m_o + k \sec Z = -2.5 \log \left(\frac{F_{obj}}{F_{ZP}} \right). \quad (5.8)$$

Rearranging gives:

$$F_{obj} = 10^{-m_o/2.5} \cdot 10^{-k \sec Z/2.5} \cdot F_{ZP}. \quad (5.9)$$

F_{ZP} for standard filters³ are typically given in units of photons/s/cm²/Å. Therefore, we need to account for the exposure time, t_{exp} , the collecting area of the primary mirror, A and the bandpass of the filter used, $\Delta\lambda$. This gives

$$F_{obj} = 10^{-m_o/2.5} \cdot 10^{-k \sec Z/2.5} \cdot F_{ZP} \cdot t_{exp} \cdot A \cdot \Delta\lambda. \quad (5.10)$$

Finally, we must take into account various efficiencies of the telescope system, giving:

$$F_{obj} = 10^{-m_o/2.5} \cdot 10^{-k \sec Z/2.5} \cdot F_{ZP} \cdot t_{exp} \cdot A \cdot \Delta\lambda \cdot \eta_{inst} \cdot \eta_{tel} \cdot QE, \quad (5.11)$$

where η_{inst} is the instrumental throughput, η_{tel} is the reflectivity of the telescope optics and QE is the quantum efficiency of the CCD, which depends on the wavelength of light being observed. For a 2-mirror telescope with aluminium coatings, in which each coating is $\sim 90\%$ efficient, $\eta_{tel} = 0.9 \times 0.9 = 0.81$. Assuming a simple case of a filter and a plane-parallel window covering the CCD, in which each surface transmits light with an efficiency of 98% , then $\eta_{inst} = 0.98^4 \approx 0.92$. Using standard filter information² we can calculate the flux of an object with a known magnitude for a given exposure time in a given filter. For an object at 21st magnitude in the R -band ($F_{ZP} = 717$ photons/s/cm²/Å,

²Example values can be found at:

http://www.vikdhillon.staff.shef.ac.uk/teaching/phy217/instruments/phy217_inst_photcal.html#table2

³Typical values can be found at:

http://www.vikdhillon.staff.shef.ac.uk/teaching/phy217/instruments/phy217_inst_photsys.html#table1

filter bandpass $\Delta\lambda = 1330 \text{ \AA}$, $\eta_{tel} = 0.81$, $QE = 0.8$) with a mirror diameter of 30 cm ($A = 0.9\pi r^2 = 671.5 \text{ cm}^2$ where the factor of 0.9 takes into account the typical fraction of the primary mirror covered by the shadow of the secondary mirror), a 300 second exposure (the same exposure time as the LT, see table 2.1), gives $F_{obj} = 389$ photons at a typical zenith distance of 40° .

The noise sources for CCD observations can be summarised as:

- Poissonian noise of object, $\sqrt{F_{obj}}$ (photons).
- Poissonian noise of sky background, $\sqrt{F_{sky}}$ (photons/pixel).
- Poissonian noise of dark current (thermally-generated electrons from the CCD), $\sqrt{F_{dark}}$ (electrons/pixel).
- Exposure-time-independent non-Poissonian noise due to readout electronics, R (electrons/pixel).

The flux due to the sky has a similar form to equation 5.11:

$$F_{sky} = 10^{-m_{sky}/2.5} \cdot F_{ZP} \cdot t_{exp} \cdot A \cdot \Delta\lambda \cdot \eta_{inst} \cdot \eta_{tel} \cdot QE \cdot p^2. \quad (5.12)$$

where p is the platescale (in units of arcseconds/pixel). The value for m_{sky} is typically given in units of magnitudes per square arcsecond, so the factor p^2 is used to convert to units of photons/pixel. We also no longer need to correct for atmospheric extinction, as the sky background is due to scattering of light from the ground and light generated by the sky, neither of which is subject to extinction. Assuming typical observing conditions (median seeing of good observing site of $1.2''$ and a ‘grey’ moon producing $m_{sky} = 20.1$ magnitudes per square arcsecond in the R -band) we find the sky flux to be $F_{sky} = 1425$ photons/pixel.

The SNR of our object can then be calculated using:

$$\text{SNR} = \frac{F_{obj}}{\sqrt{F_{obj} + N_{pix}(F_{sky} + F_{dark}t_{exp} + R^2)}} \quad (5.13)$$

where N_{pix} is the number of pixels our object is spread over given our seeing. For typical values of $F_{dark} = 0.05$ electrons/pixel/sec and readout noise of 7 electrons/pixel we find a SNR ~ 5.5 . Therefore, we can conclude that a series of 30 cm telescopes can reach $R = 21^{\text{st}}$ magnitude with a total FoV of ~ 70 square degrees with an exposure time of 300 seconds with SNR > 5 . This also provides a pixel scale of 1.2 arcsec/pixel, which is comparable to the seeing of good observing sites such as La Palma, reducing the contribution of sky background to ~ 1 pixel.

Using the localisation accuracy of mergers shown in figure 5.1, it can be seen that the sky above La Palma in the Canary Islands should provide the smallest localisation error associated with possible sources at the time of detection, as opposed to, for example, a site in Chile, using a 3-detector (HLV) network configuration. The La Palma site is ideal for fast (< 1 hour) follow-up observations of rapidly fading transients. The telescope design presented here also allows for regular surveying of the night sky. Given that the telescope can cover 70 square degrees in a 5 minute observation, we can therefore observe around 700 square degrees per hour (given reasonable time overheads for slew/readout/etc.). For a typical 10 hour night, this will allow us to cover around 7000 square degrees per night, or the entire observable night sky every 2 nights at La Palma. This would allow us to characterise the transients in the night sky, provide EM triggers for GW analysis and provide very recent pre-trigger images for optical follow-up analysis.

5.2.4 Updated Opacities for r-process Material - Impacts for aLIGO/AdV

Soon after the initial design requirements for GOTO were first decided, as described in section 5.2.3, improvements to the kilonova models described in Metzger et al. (2010) and Metzger & Berger (2012) were published. Work by Kasen, Badnell & Barnes (2013) and Barnes & Kasen (2013) attempted to improve on the models of Metzger & Berger (2012) by using radiative transport simulations with more recent atomic-line data to estimate the opacities of the r-process material created from the neutron-rich ejecta post-merger. Using similar nuclear heating rates to those of Metzger et al. (2010) and Metzger & Berger (2012), Kasen, Badnell & Barnes (2013) used Neodymium (Nd) line data for the Lanthanide elements instead of Iron (Fe), as used by Metzger et al. (2010) and Metzger & Berger (2012). Kasen, Badnell & Barnes (2013) found that the Nd-based opacities were a factor of 100 higher than Fe-based opacities. As shown in Barnes & Kasen (2013), this results in light curves that are fainter, redder and longer lasting than those of Metzger et al. (2010) and Metzger & Berger (2012). Importantly, the light curves of Barnes & Kasen (2013) are found to peak in the Near-Infrared (NIR) region of the spectrum, rather than in the optical, as shown in figure 5.6. For comparison, Barnes & Kasen (2013) find peak absolute R -band magnitudes of $-11 \geq M_R \geq -15$ compared to $-13 \geq M_R \geq -17$ for Metzger & Berger (2012). However, the Nd line data used in the simulations of Kasen, Badnell & Barnes (2013) also suffers from uncertainties, with different line models having significant effects on the overall light curves. One example light curve (shown in figure 5.7) shows that a different line model than that shown in figure 5.6 can produce peak R -band brightnesses that are 1-2 magnitudes brighter, which are not too dissimilar to those of Metzger & Berger (2012).

Complementary work was presented by Tanaka & Hotokezaka (2013) and Hotokezaka et al. (2013), who also implement radiative transport models to the ejecta material from

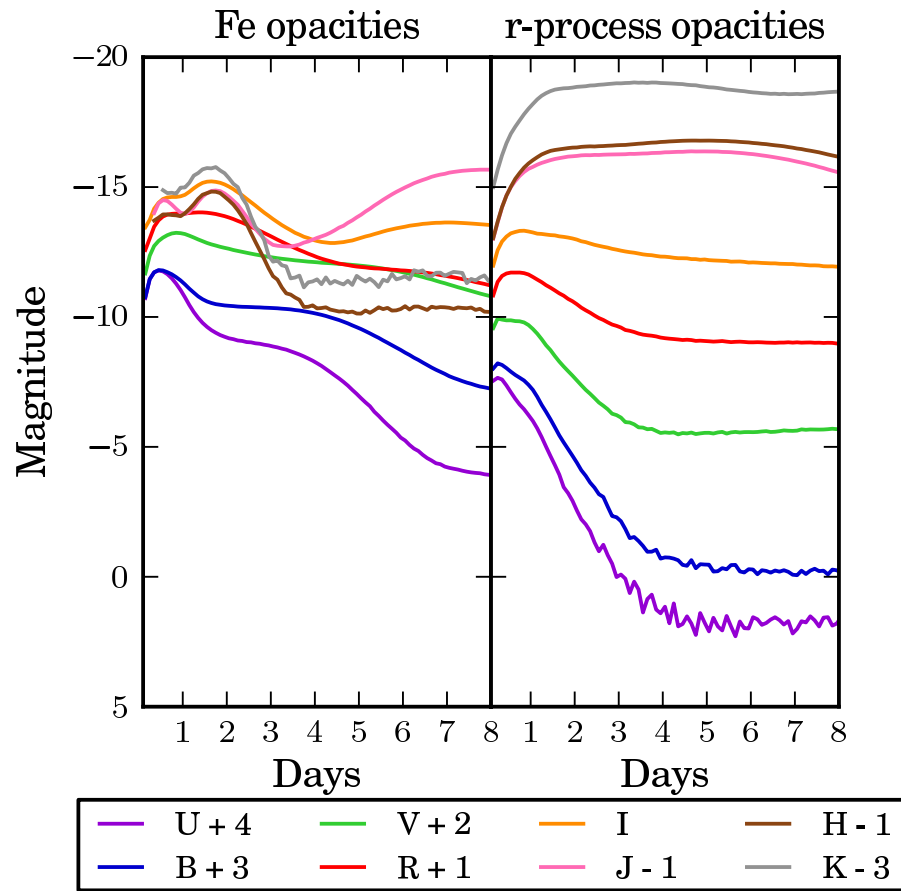


Figure 5.6: Synthetic broadband light curves calculated for the fiducial ejecta model, described in Kasen, Badnell & Barnes (2013) and Barnes & Kasen (2013), calculated using iron-like opacities (left) and r-process opacities (right). The effect of r-process opacities is to suppress the optical emission and shift the radiation toward redder bands, in particular the infrared J , H and K bands. Reproduced from Barnes & Kasen (2013).

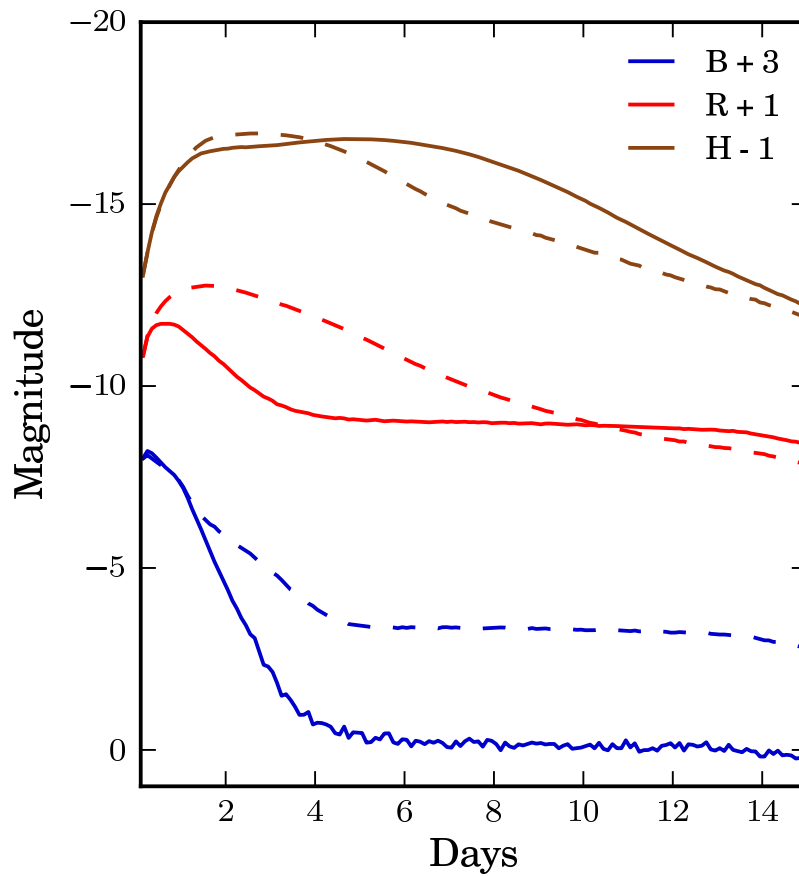


Figure 5.7: A comparison of broadband curves of the fiducial model, calculated using line data with from two different `Autostructure` models of Nd, each with a somewhat different energy level structure. Calculations using the *opt2* line data (dashed lines) predict higher magnitudes for the optical *B*- and *R*-bands than those with the *opt3* line data (solid lines). Reproduced from Barnes & Kasen (2013).

a NS-NS merger, but with less detailed line data for a broader range of elements across a wider range of merger scenarios. Tanaka & Hotokezaka (2013) find opacities similar to Kasen, Badnell & Barnes (2013), but show that the EM emission depends on the mass ratio and the Equation of State (EOS) assumed for the detailed numerical simulations of the NS-NS binary (Hotokezaka et al., 2013). Tanaka & Hotokezaka (2013) discuss two sets of models, each with their own subsets, as described below.

First, simple analytical models are used covering a range of possible scenarios:

- NSM-all: Similar to the model from (Metzger & Berger, 2012) using solar abundances of r-process material from Gallium (Ga) to Uranium (U).
- NSM-dynamical: Scenario in which the r-process is very efficient, resulting in elements with $Z \geq 55$ only.
- NSM-wind: A scenario in which feedback from the accretion onto the black hole halts the r-process early on, resulting in elements with $31 \leq Z \leq 54$ only.

Second, results from 4 numerical simulations described in Hotokezaka et al. (2013), in which the NS-NS masses are either $1.3\text{-}1.4 M_{\odot}$ or $1.2\text{-}1.5 M_{\odot}$, and the EOS of the NS pairs are either stiff (smaller NS radius, higher density) or soft (larger radius, lower density). Tanaka & Hotokezaka (2013) find light curves qualitatively similar to those shown in Barnes & Kasen (2013), with some variation dependent on the specific model used. Figure 5.8 shows the result of the NSM-all scenario, while figure 5.9 shows the light curves from all 4 numerical models in different filters. In particular Tanaka & Hotokezaka (2013) find that for soft EOS mergers, the mass ratio has little effect on the overall brightness of the light curve, while a stiff EOS can vary the peak brightness by several magnitudes, as the larger mass ratio produces more ejecta, which results in a brighter light curve.

Rosswog et al. (2013) and Grossman et al. (2013) provide further complementary work through additional simulations. Uniquely, hydrodynamical simulations by Rosswog et al.

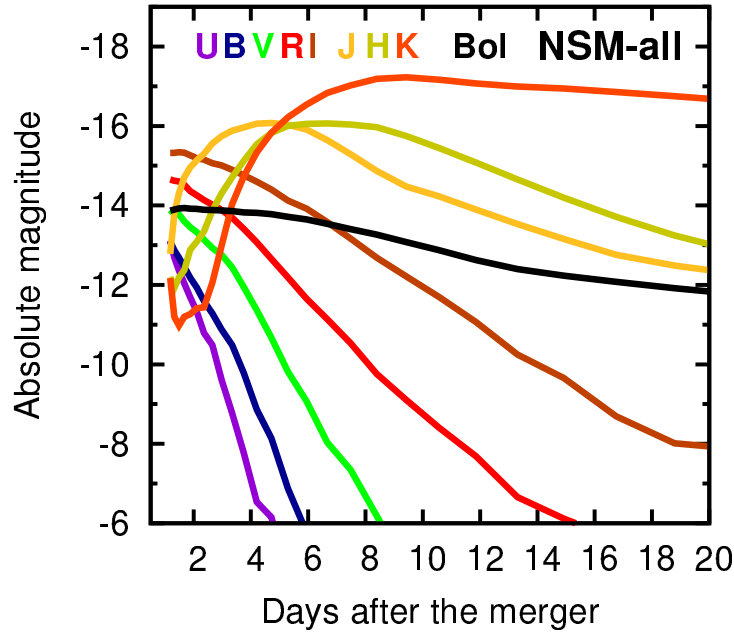


Figure 5.8: Multi-colour light curves of model NSM-all (in Vega magnitudes). Light curves in redder bands are brighter and slower fading than models from Metzger & Berger (2012). Reproduced from Tanaka & Hotokezaka (2013).

(2013) extend out to 100 years, where previous simulations were usually hydrodynamical for the first few seconds, with thermodynamic and radiative transport models for the remainder of the simulation. Rosswog et al. (2013) also do not assume spherical geometry of the ejecta. Using heating methods similar to Metzger et al. (2010) and Metzger & Berger (2012), hydrodynamical simulations described in Rosswog et al. (2013) produce similar abundances to other models. Grossman et al. (2013) investigates two possible ejecta channels and the impacts these have on the light curves we hope to detect in aLIGO. Firstly, dynamical ejecta (similar to the previous models) produces “strong” r-process material (with atomic mass number, $A > 130$), but the NS-NS mass ratio is important. They find that larger mass ratios typically produce more ejecta. These are intrinsically brighter but are more non-spherical, which could impact on the visibility of the resulting kilonova depending on the line of sight. Grossman et al. (2013) also argues that previous work by Metzger & Berger (2012) uses an electron fraction of the initial material that is too high, and shows that their work with lower electron fractions

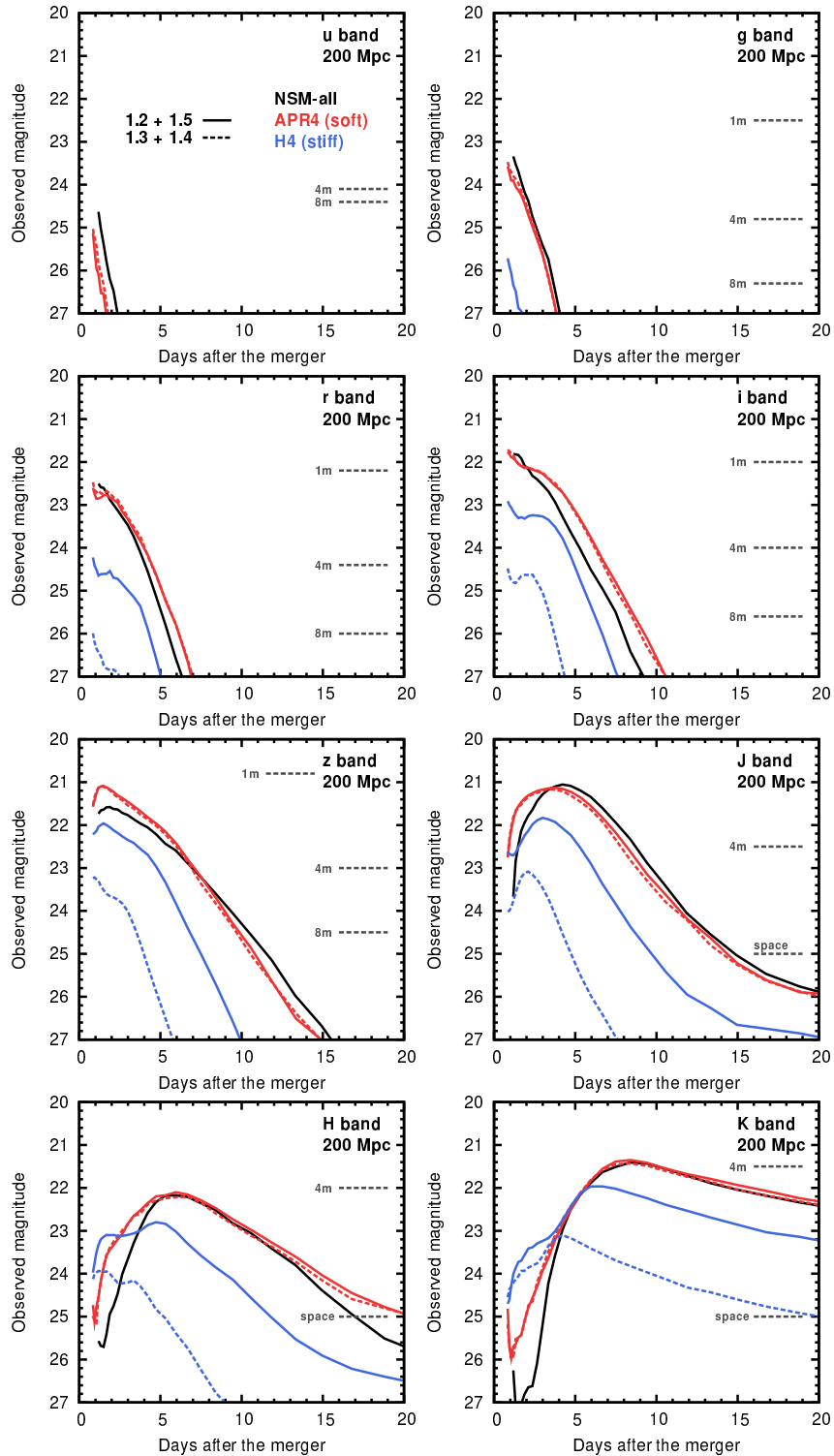


Figure 5.9: Predicted *ugrizJHK*-band light curves for model NSM-all and 4 numerical models. The distance to the NS merger event is set to be 200 Mpc. Horizontal lines show typical limiting magnitudes for wide-field telescopes (5σ with 10 min exposure, see Tanaka & Hotokezaka (2013) for details). Reproduced from Tanaka & Hotokezaka (2013).

Model Source	Type	Filter	$M(\text{Filter})$	$m@200\text{Mpc}$	$t_{\text{peak}}(\text{days})$
Metzger (2012)	On-axis GRB	r	-26.5 to -16.5	10 to 20	<0.1
	Off-axis GRB	r	-17.5 to -7.5	19 to 29	1 to 10
	Kilonova	r	-17.5 to -13.5	19 to 23	0.5 to 4
Kasen & Barnes (2013)	Kilonova	R	-15.5 to -11.2	21 to 25.3	~ 0.5 to 10
		I	-16.7 to -12	19.8 to 24.5	~ 0.5 to 10
		H	-18 to -14	18.5 to 22.5	~ 0.5 to 10
Tanaka & Hotokezaka (2013)	Kilonova 1.3-1.4 M_{\odot}	r	-14 to -10.5	22.5 to 26	~ 1
		z	-15.5 to -13	21 to 23.5	1 to 2
		J	-15.5 to -13.5	21 to 23	1 to 5
		H	-14.5 to -12.5	22 to 24	1 to 7
Grossman et al. (2013)	Kilonova 1.3-1.4 M_{\odot}	R	-14.5 to -11	22 to 25.5	0.5 to 1
		B	-13.5 to -10	23 to 26.5	0.3 to 0.5
		J	-14 to -12.5	22.5 to 24	0.5 to 2
		H	-14 to -13	22.5 to 23.5	1 to 4

Table 5.7: An example of the range of light curves from the models discussed in this chapter, showing absolute magnitudes, apparent magnitudes at a distance of 200 Mpc and the time at which the models peak for a variety of filters.

produces light curves up to 2 magnitudes fainter for similar mass ratios (see figure 5.10). However, these light curves are calculated using black body effective temperatures, and so may vary with more detailed work taking into account complex opacities. Grossman et al. (2013) also discuss the possibility of a neutrino-driven wind ejecta channel, which would produce lower mass, “weak” r-process material. Early results show that this ejecta channel could produce a shorter lived, brighter optical counterpart which peaks at around 0.5 days post-merger with a bolometric absolute magnitude of -14.9 ($m = 20.1$ at 100 Mpc), again shown in figure 5.10.

So, in conclusion, while kilonova emission is gaining traction as a real detectable counterpart to NS-NS mergers, the situation is complex, as seen in table 5.7, and changing rapidly. These models suggest that the design for GOTO may have to be altered, and that imaging to fainter magnitudes in the NIR portion of the spectrum may be necessary, but the field is currently very uncertain.

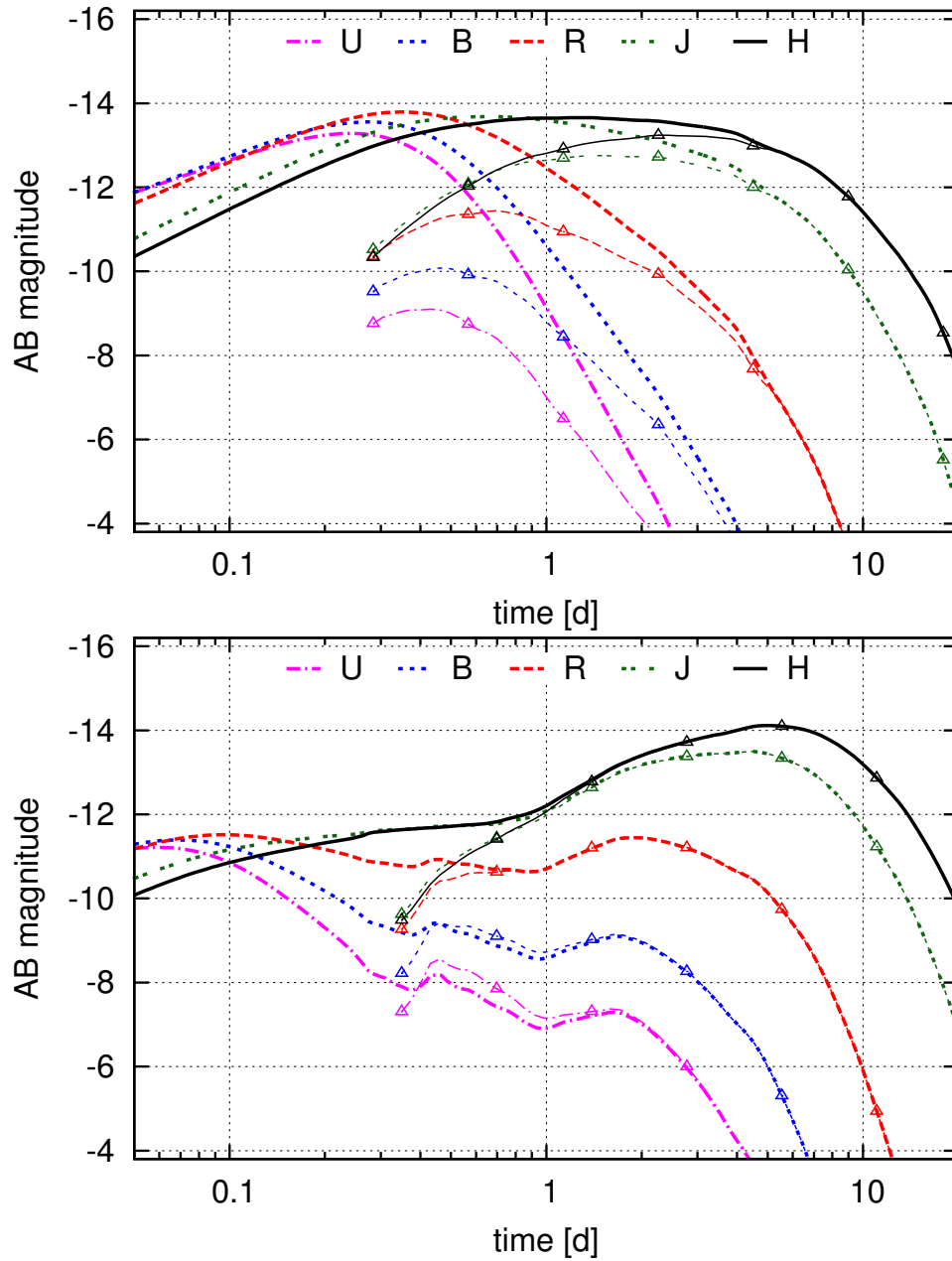


Figure 5.10: Broadband light curves from the total ejected material (dynamic ejecta plus ν -driven wind; thick lines) and the dynamically ejected matter alone (symbols; thin lines), for NS-NS masses of $1.4\text{-}1.3 M_{\odot}$ (top) and $1.8\text{-}1.2 M_{\odot}$ (bottom). As a word of caution Grossman et al. (2013) stress that the broadband light curves have been computed assuming a blackbody spectrum corresponding to the effective temperature. Reproduced from Grossman et al. (2013).

5.2.5 GRB 130603B - A Possible Kilonova Afterglow?

While writing this chapter, and investigating new theoretical models for the as-of-yet undiscovered kilonova afterglow to a NS-NS merger, the first possible detection of a real kilonova associated with a GRB was published, the properties of which are summarised here. At 2013-06-03 15:49:14 UT the Burst-Alert-Telescope (BAT) on the Swift Satellite detected a short GRB with a duration of 0.18 ± 0.02 seconds⁴. Follow-up observations using the 4.2 m William Herschel Telescope (WHT) detected an optical afterglow overlapping a galaxy detected in the SDSS survey. Both the afterglow and galaxy were found to have a redshift of $z = 0.356$. Additional observations were taken with the Hubble Space Telescope (HST) at ~ 9 days and ~ 30 days post-burst. Images were obtained in both the optical F606W filter ($0.6 \mu\text{m}$) and the NIR F160W filter ($1.6 \mu\text{m}$). Image subtraction using the early- and late-epoch images found an excess in the NIR in two independent studies (Tanvir et al., 2013; Berger, Fong & Chornock, 2013). The results given below are from Tanvir et al. (2013), but both studies are qualitatively the same. The residual NIR transient was found to have a magnitude of $m_H \sim 25.73 \pm 0.20$, approximately 3.5 magnitudes brighter than the extrapolated afterglow. No optical counterpart was found with a 2σ upper limit of $m_R > 28.25$. This excess NIR flux corresponds to a source with absolute magnitude $M(J) \approx -15.35$ approximately 7 days after the burst in the rest frame. The evolution of the optical, NIR and X-ray observations are shown in figure 5.11. The optical and X-ray afterglows decay steeply after 0.3 days, modelled as a broken power law with index ~ 2.7 . As shown in figure 5.11, this lies well within the models predicted by Kasen, Badnell & Barnes (2013) and Barnes & Kasen (2013), providing a natural explanation that the NIR transient detected in HST images is an r-process kilonova remnant from the NS-NS merger progenitor of the short GRB 130603B.

An absolute J -band magnitude of -15.35 corresponds to $m(J) = 19.47$ at a distance

⁴GCN Circulars: 14735, 14741

of 100 Mpc. For the models of Barnes & Kasen (2013), assuming that this J -band magnitude lies in the middle of their range of model light curves, a similar kilonova at a distance of 100 Mpc would have $19.5 < m(R) < 23.8$. From this, we can conclude that the kilonova models are reasonably accurate and that GOTO may be able to observe some fraction of kilonova afterglows within the conservative aLIGO/AdV distance limit of 100 Mpc. For GW detectors at full design sensitivity, which give a distance range (horizon) of 200 (400) Mpc, the brightest kilonova models would result in an R -band magnitude of around 21 (22.5), respectively. This suggests that we may need to increase the magnitude limit of our observations to observe even the brightest kilonova afterglows across the entire aLIGO/AdV distance horizon.

5.3 Conclusion

During the next few years advanced LIGO and advanced Virgo will begin regular joint observations. For the remainder of the decade, the commissioning of the detectors will slowly increase the sensitivity of the detectors, increasing the chances of detecting gravitational waves. It is hoped that this will allow routine observations of GW sources, in particular NS-NS mergers, which are expected to produce significant EM radiation. NS-NS mergers viewed on-axis are thought to be the progenitors of SGRBs, and are also predicted to produce observable off-axis EM afterglows and radioactively produced EM emission. In order to detect these EM counterparts, telescopes capable of observing sky regions covering several tens of square degrees down to a limiting magnitude of $R \approx 21$ are needed. We describe the design of a telescope, GOTO, for which EM-GW follow-up observations is the main science goal, based on models presented in Metzger et al. (2010) and Metzger & Berger (2012). More recent models, for a specific emission process known as a kilonova, suggest the detections of kilonova counterparts may be a more challenging task than anticipated, as r-process opacities can significantly alter the resulting kilonova

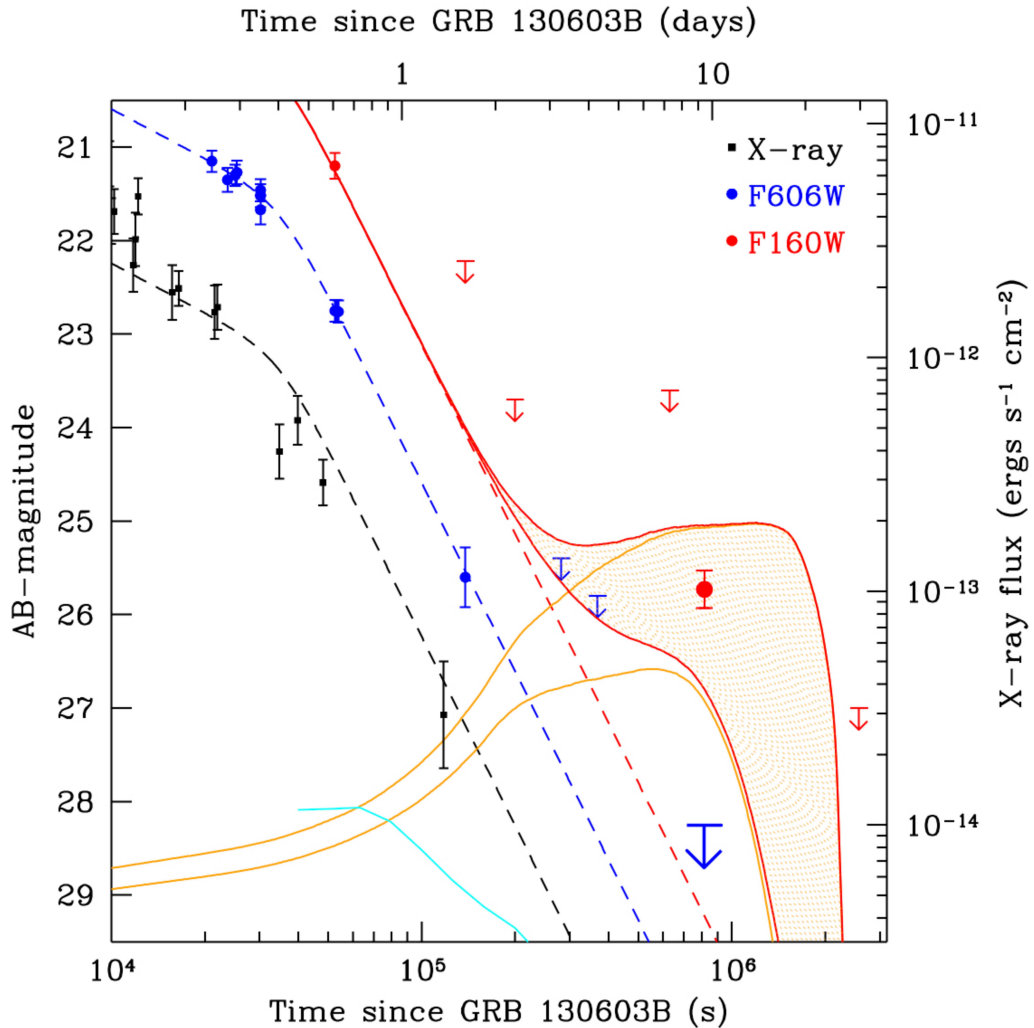


Figure 5.11: X-ray (black), optical (blue) and NIR (red) light curves of afterglows of GRB 130603B. Upper limits are 2σ and error bars are 1σ . The WHT optical data (g -, r - and i -bands) have been interpolated to the F606W band and the NIR data have been interpolated to the F160W band (see supplementary information of Tanvir et al. (2013) for a full description). HST epoch-1 points are given by bold symbols. Dashed lines are simple afterglow power-law decays. The solid orange curves correspond to model light curves from Kasen, Badnell & Barnes (2013) and Barnes & Kasen (2013) for ejecta masses of $10^{-2} M_{\odot}$ (lower) and $10^{-1} M_{\odot}$ (upper). Added to the afterglow decay curves, this produces the solid red curve/hatched region. The cyan curve shows that even the brightest optical kilonova emission is negligible. Reproduced from Tanvir et al. (2013).

light curves. These models suggest that the EM emission from a kilonova is longer lasting, fainter and peaks in the near infra-red portion of the spectrum. While these models suffer from several uncertainties, and cover a wide range of brightnesses and lifetimes (see table 5.7), the detection of a possible kilonova remnant accompanying the short GRB 130603B lends weight to these models. Due to the brightness of the kilonova models, GOTO may not be able to observe even the brightest afterglows given in Barnes & Kasen (2013) beyond a distance of 200 Mpc in the R -band, Therefore, further work must be done to investigate improvements to GOTO, which can increase the chances of detecting a kilonova afterglow. The kilonova models suggest that peak brightness occurs in the NIR region of the spectrum. However, sky brightness can be 8 magnitudes brighter than in the optical, so we may benefit from pushing further into the red, but still optical, portion of the spectrum. Using figure 5.6 we can see that observing in the I -band results in an afterglow that is 3-4 magnitudes brighter than in the R -band, while not suffering from increases in sky brightness on the same scale as NIR observations. However, conventional CCDs decrease in sensitivity with increasing wavelength. One method of increasing the sensitivity in the I -band is to replace conventional CCDs with deep-depletion CCDs (see Rahmer et al., 2012, for an example), which have a thicker layer of silicon for longer wavelength light to interact and free a photoelectron, increasing the QE of the CCD by over a factor of 2 for far-red observations.

Chapter 6

Conclusions and Future Work

Over the last few years, GW detectors have begun approaching the sensitivity limit required for routine observations of GWs. To do so, detectors must be capable of detecting changes in length that are $\sim 1/1000^{\text{th}}$ of the width of a proton. Together with interference from noise sources such as seismic activity, laser shot noise, weather effects and even the deformation of the Earth's crust due to the Moon, this provides a huge technical challenge. However, the development of sophisticated seismic isolation systems, large mass pendulum mirrors and stabilised, high-power lasers have helped reduce these noise sources to a manageable level. As well as confirming a key prediction of Einstein's theory of general relativity, a GW detection will be a huge technical achievement.

6.1 Electromagnetic Follow-up

The routine detection of GWs alone will give us a new and unique means with which to explore the Universe, allowing us to see into the regions typically opaque to EM observations. By combining GW detections with EM observations, it is possible to gain even greater insight into the physical processes at work. A classic example is that of GRBs; Long GRBs should have been detectable within a few Mpc for the 2009-2010

science run, while Short GRBs were detectable out to ~ 50 Mpc. By combining GW and EM detections, not only can we increase the confidence of a GW detection, but it is possible to gain much more detail on the central engines of the objects, as GWs are unobscured by intervening matter, unlike light, which suffers from scattering and absorption.

Chapter 2 describes the first attempt at performing EM follow-up of GW candidates using a range of GW trigger generators and partner observatories. GW data from the two LIGO detectors and the Virgo detector were analysed by three trigger generators, looking for both unmodelled GW burst signals and signals which matched theoretical waveforms, which allowed us to reconstruct a source position on the sky, known as skymaps. These skymaps, when combined with prior information of the location of nearby galaxies, allowed us to use EM observatories to image the most interesting regions of the sky in response to a GW trigger. Over the 2009-2010 science run, 8 triggers were identified and sent for observation by partner observatories, resulting in over 1,800 images from the optical telescopes alone, from which no EM candidates were observed. One of these GW triggers was part of a blind injection challenge, where a simulated transient was added to the detector data to test the analysis pipelines. The trigger generators placed the origin of the transient near Canis Majoris, giving the event the moniker “Big Dog”, with an official designation of GW100916. Initial analysis suggested that the transient was similar to a typical inspiral signal. More in depth analysis found that the system was most likely a BH-BH binary object with component masses $5.4 < M_1 < 10.5 M_\odot$ and $2.7 < M_2 < 5.6 M_\odot$, at a distance of between 7 and 60 Mpc, with an extremely low false alarm rate of 1 event per 7000 years. Errors in the injection software resulted in an incorrect waveform and sky location, but once corrected the analysis results and blind injection matched.

My contribution to the work described in chapter 2 was the creation and testing of code which ranked galaxies based on their likelihood of hosting the GW source, and the

subsequent observation requests, for the Liverpool Telescope and LOFAR. I also acted as an “on-call” EM follow-up expert, whose role is to provide human verification of a GW trigger, and submitting the observing requests to the partner telescopes.

6.2 The Gravitational Wave Galaxy Catalogue

In chapter 3 we created the Gravitational Wave Galaxy Catalogue (GWGC; White, Daw & Dhillon, 2011), which contains 53,225 galaxies within 100 Mpc, which was used to image the sky regions we considered most interesting. By this, we mean regions of the sky which contain the most extragalactic stellar mass, as GW sources are expected to be rare in our own galaxy, but strong enough to be seen out to distances of tens of Mpc for NS-NS mergers. In order to image these regions, we needed an up-to-date catalogue of nearby galaxies. Previous catalogues used within LIGO suffered from degeneracies and did not include data from the most recent data releases from large-area galaxy surveys. The GWGC was created using a combination of local and extended galaxy catalogues from the literature, and includes the most accurate distances and positions available, along with diameters, position angles and B -band magnitudes where possible for each galaxy in the catalogue. Comparisons with the expected distribution of blue light based on SDSS data shows that the catalogue is almost complete out to a distance of ~ 40 Mpc, but suffers from systematic incompleteness beyond this distance, which will only be solved with the inclusion of a deep, all-sky galaxy survey. In anticipation of the advanced detector era, an updated catalogue was also produced which contained I -band magnitude measurements for as many galaxies as possible. This allows an estimate of the mass of a galaxy to be made, rather than relying on blue luminosity as a tracer of NS-NS merger likelihood (Kanner et al., 2012). While originally designed for the 2009-2010 EM follow-up campaign, the catalogue has been used extensively within the LIGO/Virgo collaboration and beyond. See Kanner et al. (2012), Adrián-Martínez et al.

(2013a), Baret et al. (2012) and Camp et al. (2013) for some examples.

6.2.1 Optical Image Analysis from GW triggers

In chapter 4, we presented the results of the analysis of images taken by the Liverpool Telescope (LT) and the ROTSE Telescope network as part of the EM follow-up campaign described in chapter 2. The LT imaged the sky using two instruments simultaneously: the 4.7 arcminute FoV RATCam instrument at the Cassegrain focus of the telescope and the 1° FoV SkyCamZ on the finder telescope. The RATCam instrument obtained a total of 22 images over a month to be analysed for trigger G23004, along with 3 images to be combined into a high quality reference image. The SkyCamZ instrument obtained 172 images to be analysed along with 17 reference images. To ensure no optical transient was present, the reference images were taken 18 months after the original trigger. The LT image analysis pipeline was created using a python script to perform image subtraction via a series of standard programs for image analysis. The resulting residual images contained objects due to the difference between the two matched frames. These candidates were subjected to a number of cuts to remove uninteresting transient artefacts, and known variable stars and minor planets. After all cuts, we found no optical transient candidates.

The ROTSE network imaged 5 triggers, one of which was of the wrong sky position due to a software error. Additionally, one of the remaining 4 triggers was the blind injection described earlier. The ROTSE network images a single region from the first available clear night and as many subsequent nights as possible for up to 30 days. ROTSE obtained 782 images, of which 411 had to be removed due to poor image quality. The remaining images were analysed in a method similar to the LT using the ROTSE pipeline. Each candidate that survived the cuts was given a ranking statistic, which was compared to the background distribution taken from the analysis of 100 sets of images

from unrelated triggers, giving us a false alarm probability (FAP). For a candidate to be considered a new detection, we consider candidates with a $FAP < 0.01$, while candidates with $FAP < 0.1$ are considered for further follow-up observations. For all triggers, we found no candidates with $FAP < 0.01$, and two with $FAP \sim 0.1$, which we considered consistent with background rates.

6.2.2 Efficiency Studies of Analysis Pipelines

To ensure that our cuts do not reject the EM counterparts we hope to detect, we used simulated transients in our images and analysed them using the same data reduction pipelines. The model light curves we used were based on observed optical afterglows to LGRBs and SGRBs, and the predicted kilonova light curve from the neutron rich matter ejected during a NS-NS merger, placed at different distances out to a maximum of 1 Gpc. For the high quality LT images, we were able to simply inject model stars using a Moffat profile. For the LT we were able to recover 80-90% of all models, covering the entirety of the 50 Mpc LIGO/Virgo distance horizon for NS-NS mergers, and beyond 1 Gpc for the brightest GRB injections.

For ROTSE, special care had to be taken to account for the variation of the PSF across the FoV, often resulting in elliptical sources. To account for this, we used stars in the field as templates, which were extracted, scaled and copied to the injection region. Simply adding the scaled template star resulted in an obvious variation in the background noise, which needed to be scaled first. The resulting injections allowed us to recover model transients with efficiencies which varied from 20% to 80% due to the removal of poor quality images. The ROTSE pipeline also masked saturated pixels, resulting in the rejection of bright transients. Worryingly, this would reject all of the brightest LGRB afterglows within 100 Mpc and most of the brightest SGRB injections within 10 Mpc.

6.2.3 Follow-up in the Advanced Detector Era

The detectors used during the 2009-2010 science run are currently in the process of being upgraded which is expected to lead to an improvement in sensitivity of a factor of 10. These advanced detectors are expected to begin joint observations from 2015/2016, initially at reduced sensitivities, which increases towards the design sensitivity after a few years. There are also plans to install a third aLIGO detector at a site in India, which should hopefully begin operation in the early 2020s. The capabilities of the telescopes used during the 2009-2010 science run taught us valuable lessons for the planning of EM follow-up with aLIGO/AdV. While the increased sensitivity will allow aLIGO to detect NS-NS mergers out to an average distance range (maximum distance) of ~ 200 Mpc (~ 450 Mpc), the localisation of the advanced detectors before LIGO-India comes online will still be of the order of 10's of square degrees. It is therefore vital that we have telescopes capable of imaging these large, disjointed sky areas down to at least 21st magnitude. Using more recent light curve models than those used in the injection studies in chapter 4, we were able to create a design specification for a telescope to be used in the advanced detector era, which we call the Gravitational-wave Optical Transient Observatory (GOTO). This facility is designed to reach a limiting magnitude of $R = 21$ with a 300 second exposure, and covers a sky area of around 70 square degrees via 8 individually steerable telescopes, allowing us to cover asymmetric skymaps in one pointing. Placing the telescope on La Palma or in Australia, which coincide with the best sky localisations for the early advanced detector network, would allow deep, rapid (< 1 hour) follow up, which is vital for observing rapidly fading counterparts to GW sources.

6.3 Future Work

After the initial design of GOTO was created, a new series of models for the kilonova afterglows of a NS-NS merger were published (Kasen, Badnell & Barnes, 2013; Barnes &

Kasen, 2013; Tanaka & Hotokezaka, 2013; Hotokezaka et al., 2013; Rosswog et al., 2013; Grossman et al., 2013). These newer models vary slightly in their methods, but all show that the opacity of the neutron rich matter is significantly higher than anticipated. This results in light curves which peak in the near-infrared, rather than optical portion of the EM spectrum. These light curves also peak at later times and are intrinsically fainter. This has implications for the design of GOTO, which assumed that the kilonova emission peaked in the optical. Simply observing in the near-infrared may seem like an obvious solution, but sky background is several magnitudes brighter than for the optical, far-red portion of the spectrum. More work is therefore needed to refine the design of GOTO, such as using deep-depletion CCDs to be able to image in the far-red, but it may also be necessary to alter the specifications further to reach fainter limiting magnitudes.

Due to the greater distance range possible for aLIGO/AdV, a new, extended galaxy catalogue is also needed. Early work suggests that the current method of creating an extended catalogue using HyperLEDA would result in a low completeness¹. Work described in section 3.4.2, which uses H α and HI surveys, could provide modest completeness, but the surveys to create such catalogues do not currently exist in the public domain. It is obvious, therefore, that work must begin sooner, rather than later, to create a new galaxy catalogue for use during the advanced detector era. As described in section 3.3.1, the inclusion of galaxies from the 2MASS Redshift Survey could improve completeness significantly.

Finally, the mechanics of operating an EM follow-up campaign must be altered to take into account the new capabilities the advanced detector will bring, such as increased distance ranges with no initial improvement in localisation. Even if one or two observatories with specifications similar to GOTO were available, there is still some use for telescopes with a range of limiting magnitudes and FoVs. The difficulty is in utilising the available telescopes to maximise the chances of success of finding an EM counterpart.

¹Unpublished work carried out within the internal Looc-Up working group.

Early attempts to do so, using the telescopes used during the 2009-2010 science run, is presented in Singer, Price & Speranza (2012). However, this approach merely aims to image the correct region of the skymap, with no guarantee on detecting a counterpart, as the limiting magnitudes of each telescope is not taken into account (although is stated to be part of further work by the authors). Additionally, this study does not take into account the construction of new, dedicated instruments. There is also the possibility of a tiered approach to triggered observations. By passing on the location of possible transients detected by the first responders to a trigger onto deeper, possibly spectroscopic observatories will increase the information available for each candidate. For example, spectra can provide redshifts, abundances and spectral energy distributions of counterparts. The logistics of doing so becomes complicated. We must understand the background rate for optical transients to decide which candidates are statistically interesting. Some attempts to characterise the transient sky has already been performed (see Singer et al., 2013; Berger et al., 2013, for examples), but the use of a fast, wide-field optical observatory such as GOTO should improve on this. We must also ensure that telescopes do not reject candidates due to saturation, as shown with the ROTSE pipeline. Despite these questions, the future of GW astrophysics and the EM follow-up campaign looks promising, and will lead to exciting times in the coming decade.

We gratefully acknowledge the support of the United States National Science Foundation for the construction and operation of the LIGO Laboratory, the Science and Technology Facilities Council of the United Kingdom, the Max-Planck-Society, and the State of Niedersachsen/Germany for support of the construction and operation of the GEO600 detector, and the Italian Istituto Nazionale di Fisica Nucleare and the French Centre National de la Recherche Scientifique for the construction and operation of the Virgo detector. The authors also gratefully acknowledge the support of the research by these agencies and by the Australian Research Council, the International Science Linkages program of the Commonwealth of Australia, the Council of Scientific and Industrial

Research of India, the Istituto Nazionale di Fisica Nucleare of Italy, the Spanish Ministerio de Economía y Competitividad, the Conselleria d’Economia Hisenda i Innovació of the Govern de les Illes Balears, the Foundation for Fundamental Research on Matter supported by the Netherlands Organisation for Scientific Research, the Polish Ministry of Science and Higher Education, the FOCUS Programme of Foundation for Polish Science, the Royal Society, the Scottish Funding Council, the Scottish Universities Physics Alliance, The National Aeronautics and Space Administration, OTKA of Hungary, the Lyon Institute of Origins (LIO), the National Research Foundation of Korea, Industry Canada and the Province of Ontario through the Ministry of Economic Development and Innovation, the National Science and Engineering Research Council Canada, the Carnegie Trust, the Leverhulme Trust, the David and Lucile Packard Foundation, the Research Corporation, and the Alfred P. Sloan Foundation. We acknowledge the use of the HyperLEDA database, the Extragalactic Distance Database, SWarp, WCSRemap and HOTPANTS.

Appendix A

Images from Observations and Analysis for the LIGO/Virgo Joint Science Run

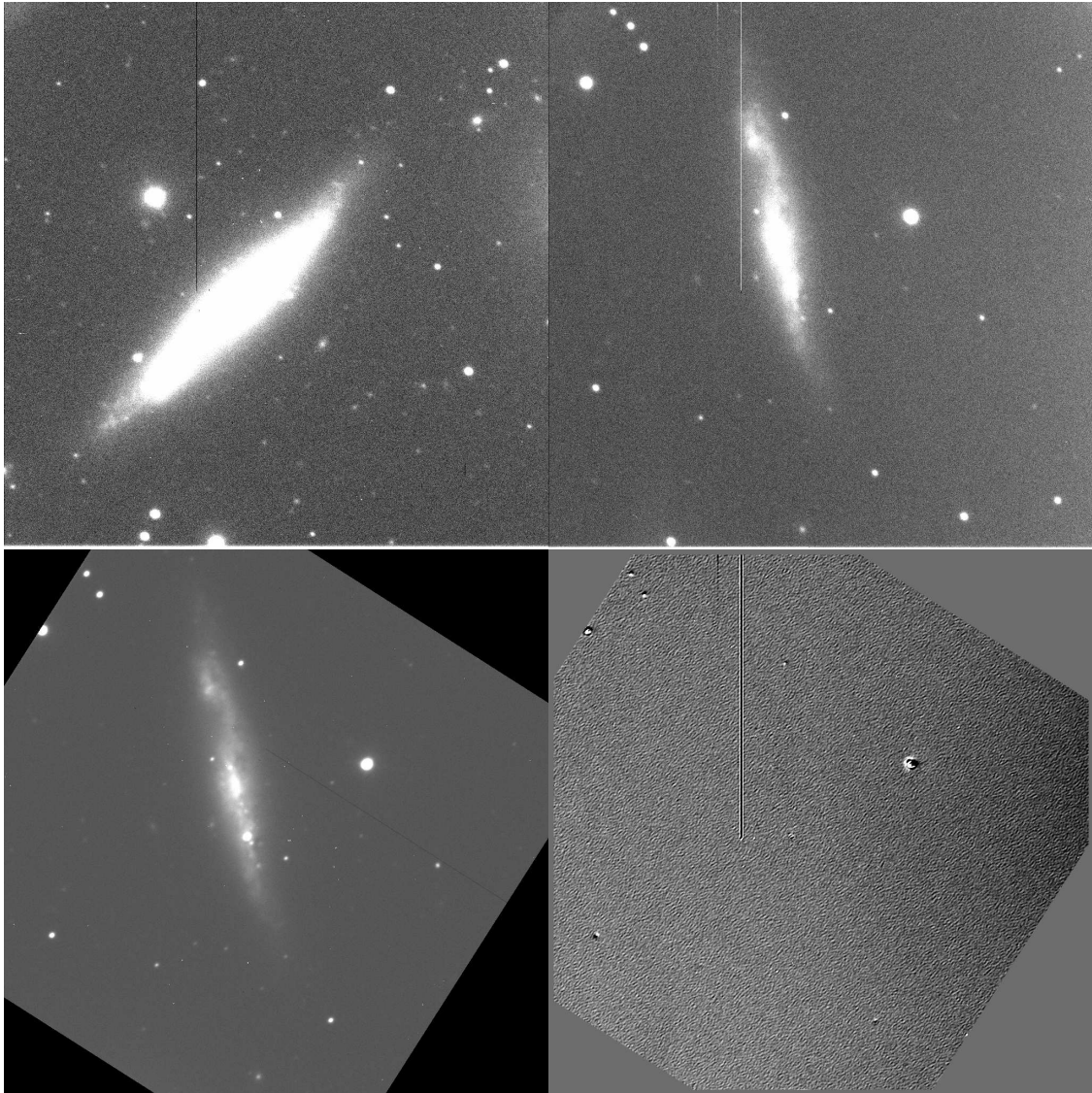


Figure A.1: Examples of images from the Liverpool Telescope RATCam instrument showing the warping and subtraction stages of the image analysis pipeline described in section 4.2.2, with the original (top left), reference (top right), warped (bottom left) and subtracted (bottom right) images shown.

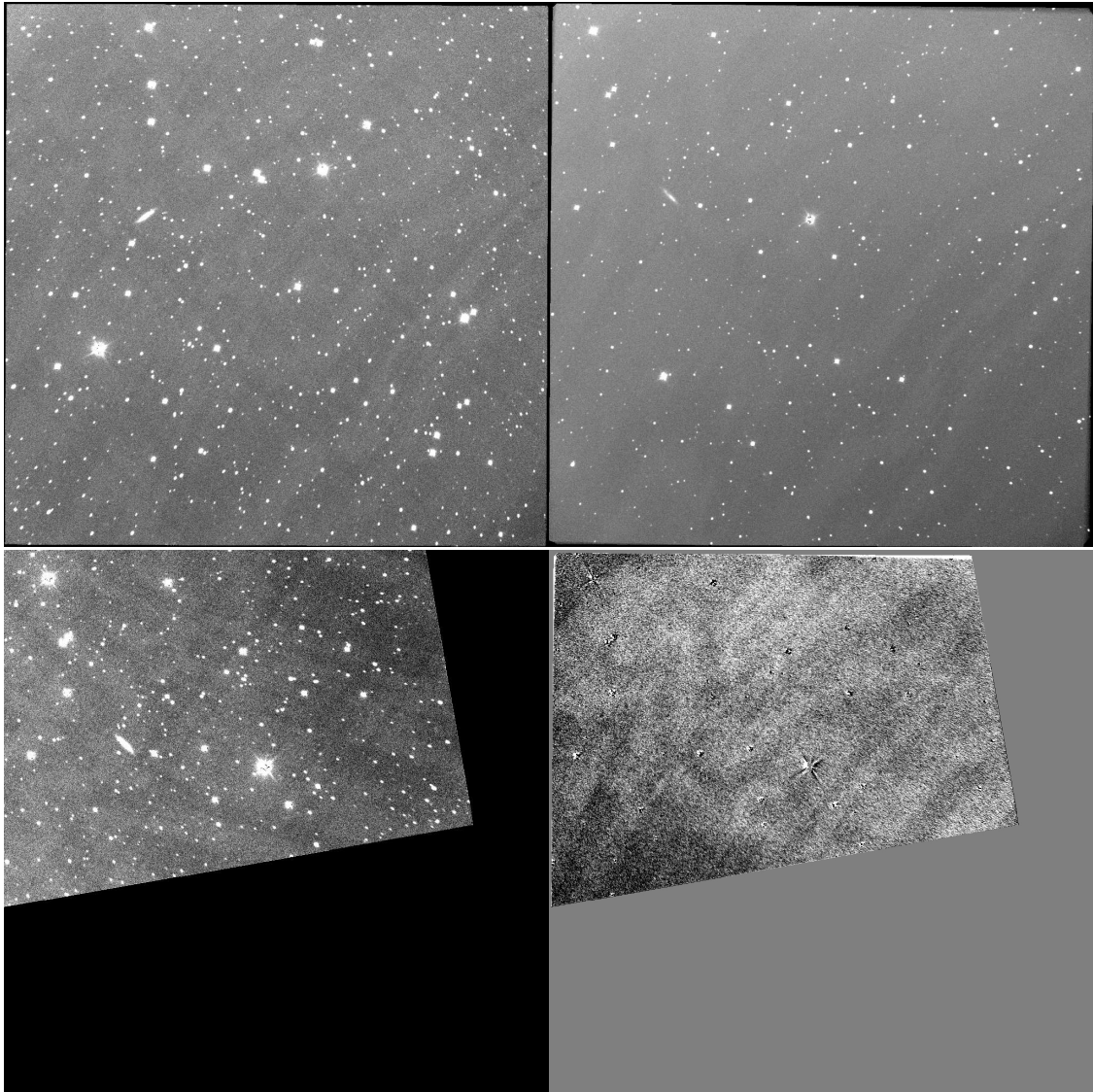


Figure A.2: Examples of images from the Liverpool Telescope SkyCamZ instrument showing the same warping and subtraction stages of the image analysis pipeline described in section 4.2.2, with the original (top left), reference (top right), warped (bottom left) and subtracted (bottom right). As discussed in section 4.2.2, the SkyCamZ images are poorly aligned with the reference image, resulting in poor coverage for analysis, impacting on the efficiencies shown in figure 4.9.

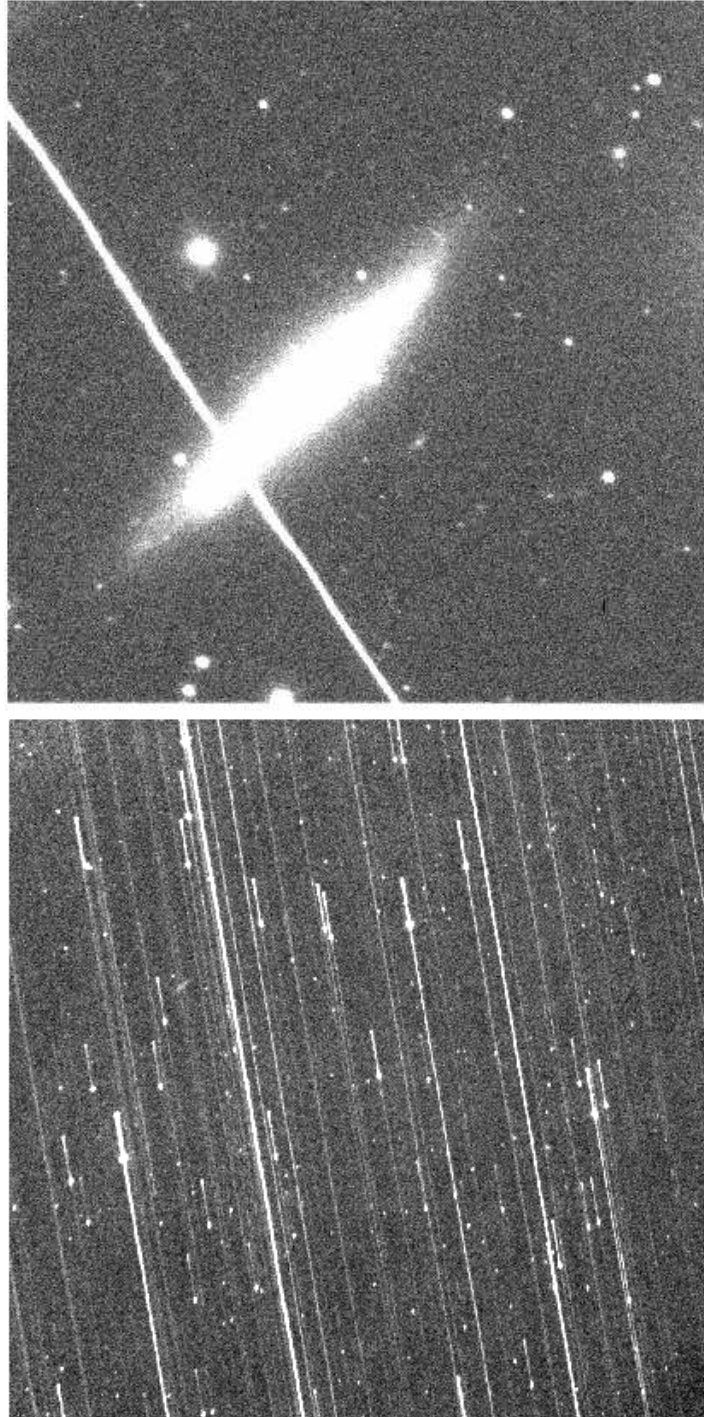


Figure A.3: Examples of images removed from the Liverpool Telescope analysis due to a passing satellite and poor tracking, as discussed in section 4.2.1.

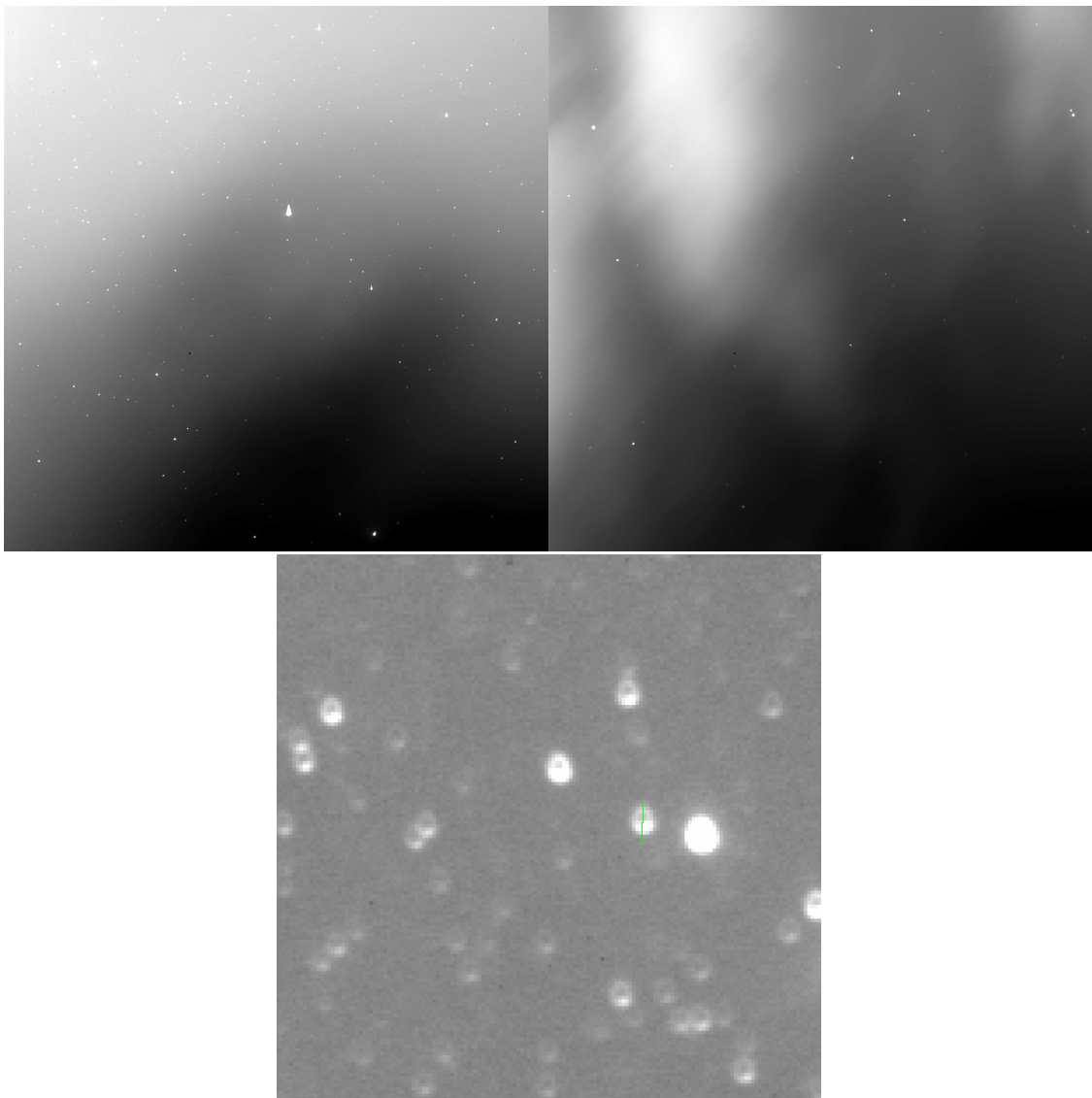


Figure A.4: Examples of images suffering from cloud cover (top) and poor focussing (bottom), removed from the ROTSE analysis, as described in section 4.3.1. The images are from triggers G20190 (top left), G23004 (top right) and G18666 (bottom)

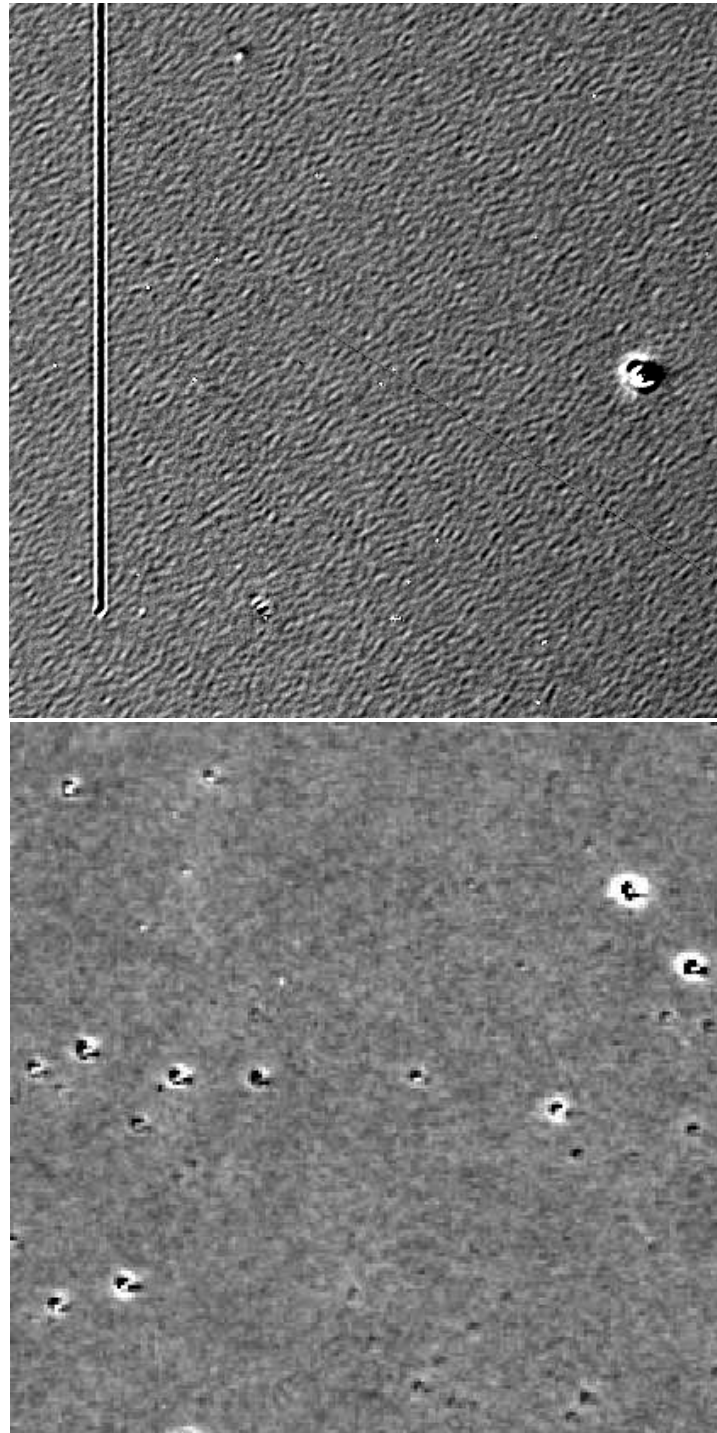


Figure A.5: Examples of artefacts resulting from poor image subtraction either due to misalignment, incorrect convolution or saturated objects for the Liverpool Telescope RATCam instrument (top) and ROTSE (bottom).

Bibliography

Aasi J. et al., 2014, *Astrophysical Journal Supplements*, 211, 7

Abadie J. et al., 2012a, *Astronomy and Astrophysics*, 541, A155

Abadie J. et al., 2012b, *Physical Review D*, 85, 082002

Abadie J. et al., 2012c, *Astrophysical Journal*, 760, 12

Abadie J. et al., 2012d, *Physical Review D*, 85, 089903

Abadie J. et al., 2010, *Nuclear Instruments and Methods in Physics Research A*, 624, 223

Abadie J. et al., 2012e, *Astronomy and Astrophysics*, 539, A124

Abadie J. et al., 2012f, *Physical Review D*, 85, 089905

Abadie J. et al., 2012g, *Astrophysical Journal*, 755, 2

Abadie J., et al., 2010, *Physical Review D*, 81, 102001

Abazajian K. et al., 2003, *Astronomical Journal*, 126, 2081

Abbott B. et al., 2008, *Astrophysical Journal*, 681, 1419

Abbott B. P. et al., 2009a, *Reports on Progress in Physics*, 72, 076901

Abbott B. P. et al., 2009b, *Physical Review D*, 80, 047101

- Acernese F. et al., 2008, *Classical and Quantum Gravity*, 25, 114045
- Adrián-Martínez S. et al., 2013a, *Journal of Cosmology and Astroparticle Physics*, 6, 8
- Adrián-Martínez S., Samarai I. A., Albert A., André M., Anghinolfi M., et al., 2013b, *Journal of Cosmology and Astroparticle Physics*, 6, 8
- Akerlof C. W. et al., 2003, *Publications of the Astronomical Society of the Pacific*, 115, 132
- Alard C., 2000, *Astronomy and Astrophysics Supplements*, 144, 363
- Alard C., Lupton R. H., 1998, *Astrophysical Journal*, 503, 325
- Amaro-Seoane P. et al., 2013, *GW Notes*, Vol. 6, p. 4-110, 6, 4
- Antonucci F. et al., 2012, *Classical and Quantum Gravity*, 29, 124014
- Atwood B. et al., 2012, in *Society of Photo-Optical Instrumentation Engineers (SPIE) Conference Series*, Vol. 8446, Society of Photo-Optical Instrumentation Engineers (SPIE) Conference Series
- Atwood W. B. et al., 2009, *Astrophysical Journal*, 697, 1071
- Baltay C., et al., 2007, 119, 1278
- Baret B. et al., 2012, *Physical Review D*, 85, 103004
- Barnes J., Kasen D., 2013, *ArXiv e-prints*: 1303.5787
- Barthelmy S. D. et al., 2005, *Space Science Reviews*, 120, 143
- Belczynski K., Bulik T., Rudak B., 2002, *Astrophysical Journal*, 571, 394
- Belczynski K., Kalogera V., Bulik T., 2002, *Astrophysical Journal*, 572, 407

- Belczynski K., Perna R., Bulik T., Kalogera V., Ivanova N., Lamb D. Q., 2006, *Astrophysical Journal*, 648, 1110
- Bell E. F., de Jong R. S., 2001, *Astrophysical Journal*, 550, 212
- Bell E. F., McIntosh D. H., Katz N., Weinberg M. D., 2003, *Astrophysical Journal Supplements*, 149, 289
- Berger E., 2009, *Astrophysical Journal*, 690, 231
- Berger E., Fong W., Chornock R., 2013, ArXiv e-prints: 1306.3960
- Berger E. et al., 2013, ArXiv e-prints: 1307.5324
- Bertin E., Arnouts S., 1996, *Astronomy and Astrophysics Supplements*, 117, 393
- Bertin E., Mellier Y., Radovich M., Missonnier G., Didelon P., Morin B., 2002, in *Astronomical Society of the Pacific Conference Series*, Vol. 281, *Astronomical Data Analysis Software and Systems XI*, Bohlender D. A., Durand D., Handley T. H., eds., p. 228
- Blanton M. R. et al., 2003, *Astrophysical Journal*, 592, 819
- Blanton M. R., Roweis S., 2007, *Astronomical Journal*, 133, 734
- Branchesi M., LIGO Scientific Collaboration, Virgo Collaboration, 2012, *Journal of Physics Conference Series*, 375, 062004
- Burrows D. N. et al., 2004, in *Society of Photo-Optical Instrumentation Engineers (SPIE) Conference Series*, Vol. 5165, *Society of Photo-Optical Instrumentation Engineers (SPIE) Conference Series*, Flanagan K. A., Siegmund O. H. W., eds., pp. 201–216
- Camp J. et al., 2013, *Experimental Astronomy*, 36, 505

- Coward D. M., et al., 2010, *Publications of the Astronomical Society of Australia*, 27, 331
- Cutler C., Thorne K. S., 2002, in *General Relativity and Gravitation*, Bishop N. T., Maharaj S. D., eds., pp. 72–111
- Danzmann K., 2000, *Advances in Space Research*, 25, 1129
- de Freitas Pacheco J. A., Regimbau T., Vincent S., Spallicci A., 2006, *International Journal of Modern Physics D*, 15, 235
- Drozdovsky I. O., Karachentsev I. D., 2000, *Astronomy and Astrophysics Supplements*, 142, 425
- Einstein A., 1918, *Sitzungsberichte der Königlich Preußischen Akademie der Wissenschaften (Berlin)*, Seite 154-167., 154
- Evans P. A., Fridriksson J. K., Gehrels N., Homan J., Osborne J. P., et al., 2012, *Astrophysical Journal Supplements*, 203, 28
- Fairhurst S., 2009, *New Journal of Physics*, 11, 123006
- Fender R. P. et al., 2006, in *VI Microquasar Workshop: Microquasars and Beyond*
- Ferrari V., Matarrese S., Schneider R., 1999a, *Monthly Notices of the Royal Astronomical Society*, 303, 247
- Ferrari V., Matarrese S., Schneider R., 1999b, *Monthly Notices of the Royal Astronomical Society*, 303, 258
- Folkes S. et al., 1999, *Monthly Notices of the Royal Astronomical Society*, 308, 459
- Freedman W. L. et al., 2001, *Astrophysical Journal*, 553, 47
- Freise A., Strain K., 2010, *Living Reviews in Relativity*, 13, 1

- Gallego J., Zamorano J., Aragon-Salamanca A., Rego M., 1995, *Astrophysical Journal Letters*, 455, L1
- Gehrels N. et al., 2004, *Astrophysical Journal*, 611, 1005
- Gehrels N., Ramirez-Ruiz E., Fox D. B., 2009, *Annual Review of Astronomy and Astrophysics*, 47, 567
- Grossman D., Korobkin O., Rosswog S., Piran T., 2013, ArXiv e-prints: 1307.2943
- Harris W. E., 1996, *Astronomical Journal*, 112, 1487
- Harry G. M., LIGO Scientific Collaboration, 2010, *Classical and Quantum Gravity*, 27, 084006
- Hobbs G., 2011, in *High-Energy Emission from Pulsars and their Systems*, Torres D. F., Rea N., eds., p. 229
- Hotokezaka K., Kiuchi K., Kyutoku K., Okawa H., Sekiguchi Y.-i., Shibata M., Taniguchi K., 2013, *Physical Review D*, 87, 024001
- Huchra J. P. et al., 2012, *Astrophysical Journal Supplements*, 199, 26
- Hulse R. A., Taylor J. H., 1975, *Astrophysical Journal Letters*, 195, L51
- Jacoby B. A., Cameron P. B., Jenet F. A., Anderson S. B., Murty R. N., Kulkarni S. R., 2006, *Astrophysical Journal Letters*, 644, L113
- Jones D. H. et al., 2004, *Monthly Notices of the Royal Astronomical Society*, 355, 747
- Ju L., Blair D. G., Zhao C., 2000, *Reports on Progress in Physics*, 63, 1317
- Kann D. A. et al., 2011, *Astrophysical Journal*, 734, 96
- Kann D. A. et al., 2010, *Astrophysical Journal*, 720, 1513

- Kanner J., 2011, PhD thesis, LOOC UP: Seeking Optical Counterparts to Gravitational Wave Signals, University of Maryland
- Kanner J., Camp J., Racusin J., Gehrels N., White D., 2012, *Astrophysical Journal*, 759, 22
- Kanner J., Huard T. L., Márka S., Murphy D. C., Piscionere J., Reed M., Shawhan P., 2008, *Classical and Quantum Gravity*, 25, 184034
- Karachentsev I. D., Karachentseva V. E., Huchtmeier W. K., Makarov D. I., 2004, *Astronomical Journal*, 127, 2031
- Kasen D., Badnell N. R., Barnes J., 2013, *Astrophysical Journal*, 774, 25
- Kasliwal M. M., Nissanke S., 2013, ArXiv e-prints: 1309.1554
- Keller S. C., et al., 2007, *Publications of the Astronomical Society of Australia*, 24(1), 1
- Kennicutt, Jr. R. C., Lee J. C., Funes, José G. S. J., Sakai S., Akiyama S., 2008, *Astrophysical Journal Supplements*, 178, 247
- Klotz A., Boër M., Atteia J. L., Gendre B., 2009, *Astronomical Journal*, 137, 4100
- Kokkotas K. D., 2008, in *Reviews in Modern Astronomy*, Vol. 20, *Reviews in Modern Astronomy*, Röser S., ed., p. 140
- Kopparapu R. K., Hanna C., Kalogera V., O'Shaughnessy R., González G., Brady P. R., Fairhurst S., 2008, *Astrophysical Journal*, 675, 1459
- Kozai Y., TAMA-300 Team, 1999, in *Observational Astrophysics in Asia and its Future*, Chen P. S., ed., p. 35
- Kramer M. et al., 2006, *Science*, 314, 97

- Kulkarni S., Kasliwal M. M., 2009, in *Astrophysics with All-Sky X-Ray Observations*, Kawai N., Mihara T., Kohama M., Suzuki M., eds., p. 312
- Kuroda K., LCGT Collaboration, 2010, *Classical and Quantum Gravity*, 27, 084004
- Law N. M. et al., 2009, *Publications of the Astronomical Society of the Pacific*, 121, 1395
- Leavitt H. S., Pickering E. C., 1912, *Harvard College Observatory Circular*, 173, 1
- Lee M. G., Freedman W. L., Madore B. F., 1993, *Astrophysical Journal*, 417, 553
- Leibler C. N., Berger E., 2010, *Astrophysical Journal*, 725, 1202
- LIGO Scientific Collaboration, Virgo Collaboration, Aasi J., Abadie J., Abbott B. P., et al., 2013, *ArXiv e-prints*: 1304.0670
- Lorimer D. R., 2008, *Living Reviews in Relativity*, 11
- MacFadyen A. I., Woosley S. E., 1999, *Astrophysical Journal*, 524, 262
- MacFadyen A. I., Woosley S. E., Heger A., 2001, *Astrophysical Journal*, 550, 410
- Malek K. et al., 2009, in *Society of Photo-Optical Instrumentation Engineers (SPIE) Conference Series*, Vol. 7502, *Society of Photo-Optical Instrumentation Engineers (SPIE) Conference Series*
- Marion F., 2004, *Proceedings of Rencontres de Moriond on Gravitational Waves and Experimental Gravity 2003*
- Mawson N. R., Steele I. A., Smith R. J., 2013, *ArXiv e-prints*: 1305.0573
- Meegan C. et al., 2009, *Astrophysical Journal*, 702, 791
- Metzger B. D., Berger E., 2012, *Astrophysical Journal*, 746, 48
- Metzger B. D., Kaplan D. L., Berger E., 2013, *Astrophysical Journal*, 764, 149

- Metzger B. D. et al., 2010, *Monthly Notices of the Royal Astronomical Society*, 406, 2650
- Moffat A. F. J., 1969, *Astronomy and Astrophysics*, 3, 455
- Nakar E., 2007, *Physics Reports*, 442, 166
- Nuttall L. K., Sutton P. J., 2010, *Physical Review D*, 82, 102002
- Nuttall L. K., White D. J., Sutton P. J., Daw E. J., Dhillon V. S., Zheng W., Akerlof C., 2012, ArXiv e-prints: 1211.6713
- Nysewander M., Fruchter A. S., Pe'er A., 2009, *Astrophysical Journal*, 701, 824
- O'Shaughnessy R., Belczynski K., Kalogera V., 2008, *Astrophysical Journal*, 675, 566
- Ott C. D., 2009, *Classical and Quantum Gravity*, 26, 063001
- Ott C. D., Burrows A., Livne E., Walder R., 2004, *Astrophysical Journal*, 600, 834
- Paturel G., Fouque P., Bottinelli L., Gouguenheim L., 1989, *Astronomy and Astrophysics Supplements*, 80, 299
- Paturel G., Petit C., Prugniel P., Theureau G., Rousseau J., Brouty M., Dubois P., Cambrésy L., 2003, *Astronomy and Astrophysics*, 412, 45
- Perley R. A., Chandler C. J., Butler B. J., Wrobel J. M., 2011, *Astrophysical Journal Letters*, 739, L1
- Phinney E. S., 1991, *Astrophysical Journal Letters*, 380, L17
- Piran T., 2004, *Reviews of Modern Physics*, 76, 1143
- Rahmer G., Smith R. M., Bui K., Kirby E., Dekany R., Croner E., Milburn J., 2012, in *Society of Photo-Optical Instrumentation Engineers (SPIE) Conference Series*, Vol. 8446, Society of Photo-Optical Instrumentation Engineers (SPIE) Conference Series

- Roming P. W. A. et al., 2004, in Society of Photo-Optical Instrumentation Engineers (SPIE) Conference Series, Vol. 5165, Society of Photo-Optical Instrumentation Engineers (SPIE) Conference Series, Flanagan K. A., Siegmund O. H. W., eds., pp. 262–276
- Rosswog S., Korobkin O., Arcones A., Thielemann F.-K., 2013, ArXiv e-prints: 1307.2939
- Samus N. N., Durlevich O. V., Zharova A. V., Kazarovets E. V., Kireeva N. N., Pastukhova E. N., Williams D. B., Hazen M. L., 2009, VizieR Online Data Catalog, 1, 2025
- Saulson P. R., 1994, Fundamentals of interferometric gravitational wave detectors, Singapore: World Scientific Publishers, 1994, xvi, 299 p. ISBN 9810218206
- Schechter P., 1976, *Astrophysical Journal*, 203, 297
- Shaya E. J., Peebles P. J. E., Tully R. B., 1995, *Astrophysical Journal*, 454, 15
- Siemens X., Creighton J., Maor I., Majumder S. R., Cannon K., Read J., 2006, *Physical Review D*, 73, 105001
- Sigg D., 1998, LIGO DCC: P980007-00: Published in Proceedings of TASI 98
- Singer L., Price L., Speranza A., 2012, ArXiv e-prints: 1204.4510
- Singer L. P. et al., 2013, ArXiv e-prints: 1307.5851
- Steele I. A., 2001, *New Astronomy Review*, 45, 45
- Tanaka M., Hotokezaka K., 2013, ArXiv e-prints: 1306.3742
- Tanvir N. R., Levan A. J., Fruchter A. S., Hjorth J., Hounsell R. A., Wiersema K., Tunnicliffe R., 2013, ArXiv e-prints: 1306.4971

- Tonry J., Schneider D. P., 1988, *Astronomical Journal*, 96, 807
- Tully R. B., 1987, *Astrophysical Journal*, 321, 280
- Tully R. B., Rizzi L., Shaya E. J., Courtois H. M., Makarov D. I., Jacobs B. A., 2009, *Astronomical Journal*, 138, 323
- Tully R. B., Shaya E. J., Karachentsev I. D., Courtois H. M., Kocevski D. D., Rizzi L., Peel A., 2008, *Astrophysical Journal*, 676, 184
- Ushomirsky G., Cutler C., Bildsten L., 2000, *Monthly Notices of the Royal Astronomical Society*, 319, 902
- van Eerten H. J., MacFadyen A. I., 2011, *Astrophysical Journal Letters*, 733, L37
- Weber J., 1967, *Physical Review Letters*, 18, 498
- Weisberg J. M., Taylor J. H., 2005, in *Astronomical Society of the Pacific Conference Series*, Vol. 328, *Binary Radio Pulsars*, Rasio F. A., Stairs I. H., eds., p. 25
- White D. J., Daw E. J., Dhillon V. S., 2011, *Classical and Quantum Gravity*, 28, 085016
- White D. J., LIGO Scientific Collaboration, Virgo Collaboration, 2012, *Journal of Physics Conference Series*, 363, 012036
- Woolley S. E., 1993, *Astrophysical Journal*, 405, 273
- Yamamoto K. et al., 2008, *Journal of Physics Conference Series*, 122, 012002
- Yuan F., 2010, PhD thesis, *Chasing the brightest cosmic explosions with ROTSE-III*, University of Michigan
- Yuan F., Akerlof C. W., 2008, *Astrophysical Journal*, 677, 808
- Zwaan M. A., Meyer M. J., Staveley-Smith L., Webster R. L., 2005, *Monthly Notices of the Royal Astronomical Society*, 359, L30